Process Modeling, Validation and Process Intensification of Vacuum Membrane Distillation

Thesis submitted in partial fulfilment

of the requirements for the degree

of

DOCTOR OF PHILOSOPHY

Submitted by

SHANMUGAM V

(Reg. No. 206107026)

DEPARTMENT OF CHEMICAL ENGINEERING

INDIAN INSTITUTE OF TECHNOLOGY, GUWAHATI

GUWAHATI-781039, ASSAM, INDIA

August 2025

Indian Institute of Technology Guwahati
Guwahati-781039, Assam, India
Department of Chemical Engineering

ACKNOWLEDGEMENT

I hereby certify that the work presented in this thesis entitled **"Process Modeling, Validation and Process Intensification of Vacuum Membrane Distillation"** is the outcome of my original research work carried out at the at Department of Chemical Engineering, Indian Institute of Technology Guwahati, under supervision of **Prof. Senthilmurugan Subbiah.** The result documented in this thesis are not submitted to any other university or institute for the award of any degree or diploma. Due acknowledgment has been made wherever the work described is based on the findings of investigations of others with supporting references.

Date: 23-12-2025
Place: Guwahati

Shanmugam V
Roll No. 206107026
Department of Chemical Engineering
Indian Institute of Technology, Guwahati

Indian Institute of Technology Guwahati
Guwahati-781039, Assam, India
Department of Chemical Engineering

CERTIFICATE

This is to certify that the work contained in this thesis entitled **"Process Modeling, Validation and Process Intensification of Vacuum Membrane Distillation"** is being submitted by **Shanmugam V (Roll No. 206107026),** for the award of Ph.D. degree, is a record of bonafide original research carried out by her at Department of Chemical Engineering, Indian Institute of Technology Guwahati, under our guidance and supervision. This work embodied in this thesis has not been submitted to any other University or Institute for the award of any other degree or diploma.

Date: 23-12-2025

Place: Guwahati

Prof. Senthilmurugan Subbiah
Professor
Department of Chemical Engineering
Indian Institute of Technology Guwahati

ACKNOWLEDGEMENT

With deep gratitude, I would like to acknowledge my thesis supervisor, **Prof. Senthilmurugan Subbiah**, for his unwavering guidance, inspiration, and patience throughout my Ph.D. I am sincerely thankful to him for providing me with state of art laboratory facilities, funding, and access to vast resources, as well as fostering a challenging work environment that has significantly contributed to my professional growth. The journey has been filled with numerous challenges, and I am sincerely extending my appreciation for his generosity in providing honorarium during my needful time for my academic requirements and offering continuous support throughout my research.

I would like to thank my doctoral committee members, **Prof. Anugrah Singh**, **Prof. Kalyan Raidongia**, and **Dr. Omkar Deshmukh,** for their kind words, constant encouragement, and constructive inputs during my seminars which helped shape my thesis to its present form.

I am grateful **Prof. Subrata Kumar Majumder**, Head Department of Chemical Engineering, and **Prof. Kaustubha Mohanty**, Head (Former) Department of Chemical Engineering, for their administrative assistance. I am thankful to the Department of Chemical Engineering, Analytical Laboratory Chemical Engineering, Central Instrument Facility (CIF), for providing their state-of-the-art analytical facilities. I am also grateful to all the technical staff from the departments as mentioned above.

I am obliged to the Ministry of Education, Government of India and Department of Science and Technology, tax payers of this nation for providing me with fund to carry out my research. I would extend my gratitude to Mr. Anuj and Mr. Kumaresan from Luit Renewables for the technology support during my phD work.

I would like to take these opportunities to thank all my seniors and lab mates from my research group Water-and-Energy Nexus Lab, I would like to thank Dr. Aanisha Akhtar, Dr. Ananya Bardhan, Dr. Viswanth R, Dr. Nivedhitha S, Dr. Muniraja Tippa, Dr. Surendhar G., Dr. Senthil S, Dr. Naveenkumar A Yaranal Dr. Dinesh K. Gautam, Dr. Balakumara V., Dr. Priyamjeet, Dr. Nahawand AlZainati, Ms. Neelam Dutta, Ms. Seema, Mr. Bijoyendra, Mr. Venkatesh Mr. Bedanta Chakraborty, Mr. Koushik Ghosh, Mr. Chibibharath P, Mr. Adithya, Ms. Chitra Sharma, Mr. Karthik, Mr. Satish, Mr. Kombaiahpandian, Ms. Uthara, for their constant support, laughter, and motivations. I would also like to thank our lab assistants, Mr. Banajit Saloi, Mr. Rupam, Mr. Krishna and Mr. Bishnu Sharma, for their timely assistance. I would

like to extend my sincere thanks to Mr. Sai Mukesh for his valuable support during my phD tenure. I thoroughly overhelmed on discussing the fundamental concepts of chemical engineering, updating my numerical skills along with him. I would extend my gratitude to Ms. Stuti Dubey for her continuous support and motivation in handling this long journey.

I am grateful to my friends, Bharatheeswaran, Pradeep kumar, Giridhar, Kannan, Naveen, Dr. Thirukumaran, Thilagaraj, Raghavan, Harish, Askar, Jenny, Rigved, Nayanita for their constant love, support, and motivations. I am humbled to be a part of Tamil Sangam and Tamil Thalaivas cricket team where I got the platform to enhance my managerial and leadership skills. My cricket group friends, Ashwin, Eswar Srinivasan, Rishi, Magesh kumar, Dr. Deepak, Dr. Pilli rajasekhar, Dr. Tamil, Mukesh, Dilip, Rajavelu, Dr. Soundar, Allanblessraj all had a wonderful memories on and off the ground.

No words would suffice to express my most profound sense of gratitude to my mother Kamatchi, and father Viswanathan for supporting me in all circumstances and keeping the hope for my success in career. I would also like to thank my brother Balaji for his support. I am deeply grateful to my bachelor's faculty members Dr. M. Helen Kalavathy, Dr. Uma, Dr. Balasubramanian, and Dr. Prakash for fostering my interest and motivation in chemical engineering.

I would like to extend my sincere gratitude to all my dear friends and well-wishers for their constant support and encouragement.

(Shanmugam V)

Department of Chemical Engineering,

Indian Institute of Technology Guwahati

ABSTRACT

Water scarcity and the increasing demand for high-purity water in industrial and environmental sectors have intensified the global pursuit of sustainable and energy-efficient technologies. The treatment and resource recovery of industrial effluents are central to achieving true zero liquid discharge (ZLD), yet billions of cubic meters of wastewater, laden with valuable solutes are released untreated. Traditional separation processes often fail to recover these solutes efficiently, either due to high energy demands, material incompatibility, or limited selectivity.

The established membrane-based technologies such as Reverse Osmosis (RO) are constrained while handling highly concentrated solutions primarily due to the high osmotic pressure and severe fouling challenges, whereas Forward Osmosis (FO) is energetically favourable but limited by the complexity of draw solution regeneration. Conventional thermal based membrane technologies such as Multistage Flash Distillation (MSF) and Multi effective Distillation (MED) often posing a challenge in high scale operations such as capital and operating cost especially for decentralized applications. However, Vacuum Membrane Distillation (VMD) has emerged as a promising thermal based membrane technology, offering advantages in flux performance and thermal efficiency, yet its widespread adoption is hindered by high energy consumption, limited system integration strategies and need for the optimization of membrane module design. This thesis addresses these critical research gaps by exploring fundamental aspects of energy optimization in VMD for its widespread application on concentration and potential for crystallization, further recovery of heavy metal ion enabling ZLD.

This thesis investigates the feasibility of the VMD process for concentrating molybdenum from heavy fraction pitch through experimental studies, alongside performance evaluation through mathematical modelling validated with experimental data using both freshwater and saline feeds. The study is further extended to address energy minimization by integrating the VMD system with various energy recovery devices (ERDs), including a heat exchanger (HX), thermoelectric heat pump (TEHP), vapor compressor (VC), and conventional heat pump (HP). These integrations aim to explore energy pinch analysis and maximize latent heat recovery within the VMD system, thereby enhancing its overall energy efficiency and viability for resource recovery and ZLD applications.

The developed mathematical model is studied for optimization of HF membrane properties such as tortuosity, heat and mass transfer co-efficient and HF module length respectively. The proposed model integrates heat, mass and momentum and membrane transport equations and they are implemented in modelica language using Dynamic Modelling Laboratory (DYMOLA). Momentum balance in lumen side is incorporated using modified Hagen Poiseuille equation and vapor transport through the membrane is modelled by using Knudsen, and Poiseuille mechanisms. Concentration and temperature polarization are incorporated using film theory and energy balance across the boundary layer respectively. The developed model validated with experimental data generated from HF-VMD module made of expanded Polytetrafluoroethylene (ePTFE). In the experimental input, operating parameters such as feed flowrate, feed temperature, vacuum pressure and feed concentration of feed stream were varied within their recommended operating limits of HF-VMD module. The validated model was deployed for the optimization of module design parameters and operating parameters of the HF VMD module, with particular emphasis on critical parameter membrane length. Unlike, most studies reported up to the membrane length of 0.5m, this work explored the maximum of 1m and achieved the flux of 9.2 LMH demonstrating the potential of HF-VMD for high performance applications. This study also highlights that upon decreasing the length to 0.1m, flux can be increased up to 30 times at the feed temperature of 343K as the energy loss across the module length is conserved.

Furthermore, the potential for energy recovery in VMD was investigated through integration with a TEHP. The TEHP module was employed to harness thermal energy from both the reject stream and the permeate vapor produced by the VMD system. This recovered energy was efficiently reused to preheat the feed stream to its required operating temperature through integrated heat exchange. The Coefficient of Performance (COP) for the hot side of the TEHP was observed to be higher (1.1) compared to the cold side (0.3), indicating an inherent trade-off between effective condensation and feed heating. Consequently, the number of TEHP units required for optimal energy balance was carefully evaluated through a systematic flowsheet analysis, accounting for associated energy costs. Optimal operating conditions including a feed flow rate of 600 L/h, vacuum pressure of 715 mmHg, and feed temperature of 343 K were identified as part of this study to enhance overall system efficiency.

The Latent heat recovery in the VMD system was further investigated through the integration of a heat exchanger (HX) and a vapor compressor (VC) to identify the maximum energy pinch that could be extracted. Simulations under optimal operating conditions revealed that approximately 11.1 kW of excess heat must be removed using an additional heat exchanger,

while about 16.5 kW of thermal energy is required to preheat the feed solution. With VC integration, the system performance slightly improved, reducing the excess heat removal requirement to 10.5 kW and lowering the heating demand to approximately 16 kW.

To address this energy trade-off, a heat pump (HP) was proposed, and a mathematical model was developed to meet the actual thermodynamic constraints of energy exchange. A 15-kW cooling load was fixed as the HP capacity, given that the COP on the hot side exceeded that of the cold side consistent with TEHP performance trends. The integration of the HP is expected to remove around 4 kW of residual heat from the system, significantly improving thermal balance and energy utilization. Upon integration, the energy savings upto 86% has been identified that plays a pivotal role in scaling up this MD technology.

The hydrocarbon pitch was initially subjected to comprehensive characterization using techniques such as X-ray Photoelectron Spectroscopy (XPS), Raman Spectroscopy, X-ray Diffraction (XRD), Thermogravimetric Analysis (TGA), and Inductively Coupled Plasma Mass Spectrometry (ICP-MS) to determine the molybdenum content. Based on this analysis, sodium molybdate was selected as a representative compound for experimental studies using the VMD system. The VMD module demonstrated excellent separation performance, rejecting 99.99% of sodium molybdate and producing high-purity vapor, thus showcasing its strong potential for future applications in concentrating hydrocarbon pitch. Moreover, the concentration was successfully carried out to the point of supersaturation within the module, laying the groundwork for future studies focused on salt crystallization through VMD.

Keywords: Vacuum membrane distillation, Hollow fibre module, Optimization, Energy recovery, Gained output ratio, Coefficient of performance

Nomenclature

Notation	Definition
A, B, C	Antoine correlation constants
a, b, c	Estimated parameters from heat and mass transfer co-relation
C	Concentration (g/L)
c_p	Specific heat capacity (J/Kg.K)
D	Diffusion coefficient (m^2/s)
d_i	Inner diameter of the membrane (m)
d_p	pore size of the membrane(m)
h	Heat transfer coefficient (W/m^2K))
K	Mass transfer co-efficient (m/s)
k	Thermal conductivity (W/mK)
L	Length (m)
M	Molecular weight (g/mol)
N	Mass flux (Kg/m^2h)
n	number of finite elements
P	Pressure (Pa)
P^o	Vapor Pressure (Pa)
P_a	air pressure within the pores
Q	Feed flowrate (L/h)
r	Pore radius of the membrane (m)
T	Temperature (K)
v	Velocity of the feed (m/s)

Greek letters

ΔP_m	Pressure difference between feed and permeate side of the membrane (Pa)
μ	Viscosity of the feed liquid (Ns/m^2)
ϵ	fractional void volume in the membrane
τ	Tortuosity of the membrane
$\Re$	Universal Gas Constant(J/kg.K)
θ	Temperature polarization co-efficient
δ	Thickness of membrane(m)
ΔH	Latent heat of Vaporization(J/kg)
λ	mean free path of water vapor (µm)
α	Seebeck coefficient of the thermoelectric material V/K
η	Efficiency
ρ	Fluid density

Dimensionless numbers

Nu	Nusselt number
Pr	Prandtl number
Re	Reynolds number
Sh	Sherwood number
Sc	Schmidt number

Subscripts

avg	average pressure between membrane interface at feed and permeate side
e	effective length
exp	experimental
f	feed
fb	feed bulk
fm	feed membrane interface
lm	log mean
m	membrane
p	permeate
r	reject
s	stripping side of membrane
sb	strip side bulk
w	water
i	Iteration variable
in	inlet
l	liquid
max	maximum
mf	makeup feed
min	minimum

Abbreviations

AC	Alternating Current
AGMD	Air Gap Membrane Distillation
BPE	Boiling Point Elevation

CFNF	Critical Flowrate for Nucleate Formation
CGMD	Conductive Gap Membrane Distillation
CL	Conductive Loss
CPC	Concentration Polarization Coefficient
DASSL	Differential Algebraic System Solver
DC	Direct Current
DCMD	Direct Contact Membrane Distillation
DSC	Double Stage Cooling
DYMOLA	Dynamic Modelling Laboratory
EB	Energy Balance
ERD	Energy Recovery Device
FO	Forward Osmosis
FE	Finite Element
FS	Flat Sheet
FPC	Flat Plate Collector
ePTFE	Expanded Polytetrafluoroethylene
FS	Flat Sheet
GIT	Grid Independency Test
GOR	Gained Output Ratio
HEN	Heat Exchanger Network
HF	Hollow Fiber
HP	Horse Power
HTHP	Heating Tower Heat Pump
ICP-MS	Inductively Couple Plasma Mass Spectrophotometry
KD	Knudsen Diffusion
LB	Lower Bound
LEP	Liquid Entry Pressure
LMH	Litre per Metre squared Hour
MaB	Mass Balance
MAE	Mean Absolute Error
MB	Momentum Balance
MC	Membrane Configuration
MED	Multi Effect Distillation
MINLP	Mixed Integer Non-Linear Programming
ML	Membrane Length
MSF	Multi Stage Flash

MVMD	Multiple Vacuum Membrane Distillation modules
MVR	Multi Stage Vapor Recompression
NF	Nano Filtration
LMH	Litre per metre square per hour
OD	Osmotic Distillation
PD	Poiseuille Diffusion
PFD	Process Flow Diagram
PGMD	Permeate Gap Membrane Distillation
PID	Proportional Integral Derivative
PP	Polypropylene
PTFE	Polytetrafluoroethylene
PVDF	Polyvinylidene Fluoride
PW	Present Work
RAPC	Relative Absolute Percentage Change
RO	Reverse Osmosis
RP	Reject Pressure
RT	Reject Temperature
SEC	Specific Energy Consumption
SGMD	Sweep Gas Membrane Distillation
STEC	Specific Thermal Energy Consumption
SWRO	Sea Water Reverse Osmosis
TDS	Total Dissolved Solid
TPC	Temperature Polarization Coefficient
TR	Ton of Refrigeration
UB	Upper Bound
UF	Ultra-Filtration
XPS	X-ray Photon Spectroscopy
XRD	X-ray Diffraction
VMD	Vacuum Membrane Distillation
1-D	One Dimensional

Table of Contents

Chapter 1

1 Introduction

This chapter provides a concise overview of membrane distillation for concentration and crystallization processes, including its energy-recovery potential. It also explains the motivation for applying membrane distillation to molybdenum recovery and presents the thesis objectives.

1.1 Membrane Distillation process

In the quest for sustainable solutions to industrial effluent management, the recovery and concentration of valuable ions from wastewater streams have become a critical research focus. Heavy metal ions discharged from industries like metallurgy, petroleum refineries often exit as effluent due to the lack of technologies for the effective concentration and crystallization to reuse in the plant. The concentration and recovery of heavy metal ions from aqueous and organic solutions pose significant challenges due to the complex chemical properties of the ion, its tendency to form stable complexes, and the need for precise separation techniques to ensure high selectivity and purity.

Conventional separation process like Reverse Osmosis (RO) driven by pressure gradient, Electro dialysis (ED) driven by electric current, thermal separation process such as Multi Effect Distillation (MED), Multistage Flash (MSF) are often energy intensive process, pose significant operational charges and therefore many researchers focused in minimizing it through integration with renewable energy source [1–3].

Membrane Distillation (MD) is a combination of thermal distillation and separation through a micro porous hydrophobic membrane which permeates only pure vapor. The process operates by creating a temperature-induced vapor pressure difference across the membrane, allowing only vapor to pass through while retaining non-volatile contaminants. This mechanism enables MD to achieve high rejection rates for salts and other impurities, making it even suitable for desalination and wastewater treatment applications[4].

Interest in MD for versatile applications has grown significantly due to its capacity for complete retention of non-volatile solutes in the retentate. This attribute facilitates the concentration of valuable solutes to very high levels, thereby substantially reducing the volume of effluent requiring disposal and simultaneously enabling resource recovery and reuse. The

term MD originates from its similarity to conventional distillation, as both processes rely on vapor-liquid equilibrium for separation and require latent heat of vaporization to induce phase change. However, in MD the feed solution taken up to the saturation for separation, leading to favourable conditions for crystallization. In this scenario, the membrane surface acts as a heterogeneous nucleation site, promoting controlled crystal growth[5]. This technology is ideally suited for achieving ZLD objectives in process industries, that enhance sustainable industrial practices.

1.2 Applications of Membrane Distillation

MD has emerged as a versatile thermal–membrane process that complements and, in specific niches, outperforms conventional desalination and concentration technologies. Its distinctive attributes, near complete rejection of non-volatile solutes, operation at moderate temperatures and ambient pressures, tolerance to high-salinity feeds, and compatibility with low-grade or renewable heat, enable deployment across diverse sectors from water reuse to product concentration and crystallization [16–21]. Unlike pressure-driven membranes, MD performance is not fundamentally constrained by osmotic pressure, allowing treatment of hypersaline streams and the deliberate approach to supersaturation required for controlled solid recovery. Moreover, the process window can be tailored to balance flux, heat efficiency, and fouling/wetting resistance for the target application.

1.2.1 Desalination

VMD is an effective desalination configuration in which a vacuum on the permeate side lowers vapour-phase mass-transfer resistance, enabling high salt rejection at modest feed temperatures (≈45–80 °C).

When integrated upstream of MDC, VMD concentrates the mother liquor sufficiently to initiate controlled nucleation of target salts/complexes containing molybdenum. This tight coupling of desalination and crystallisation supports ZLD while valorising solids.

When VMD can surpass SWRO performance:

- Hypersaline feeds and RO concentrate: VMD is not limited by osmotic pressure, allowing treatment and further concentration of brines beyond the practical pressure limits of seawater reverse osmosis (SWRO).
- Availability of low-grade heat: With waste heat, solar-thermal, geothermal, or other low-grade sources, VMD’s thermal duty becomes cost-effective; electrical demand is

largely limited to circulation and vacuum, often lower than high-pressure SWRO pumping at comparable scales.

- Stringent trace-contaminant targets: VMD achieves high removals of weakly ionised or volatile species without complex pH conditioning or multi-pass trains typically required in SWRO.

Desalination coupled to crystallisation/valorisation: Where the objective is water + solids (e.g., NaCl or metal-bearing crystals), VMD's ability to operate at very high Total Dissolved Solids (TDS) and deliver supersaturation simplifies integration with MDC and can reduce the duty of standalone evaporators/crystallisers.

Overall, for high-salinity brines, off-grid or heat-rich sites, and product specifications that benefit from coupling with crystallisation (as in Mo recovery here), VMD can provide superior technical and system-level performance relative to SWRO.

1.2.2 Resource Recovery

A key advantage of MD is its ability to generate near-saturated to supersaturated retentates, which promotes crystal growth. The hydrophobic membrane surface provides heterogeneous nucleation sites, and when an external crystalliser is integrated, MDC offers controlled nucleation, faster crystallisation rates, and effective management of supersaturation. MDC is therefore well-suited for resource recovery from highly concentrated process streams and for progressing towards ZLD [22].

J. Kim et al. [23] demonstrated MDC on shale-gas produced water, leveraging the high-salinity tolerance of MD and the geothermal/waste-heat potential inherent to the process. The study examined inorganic scaling on the membrane surface and its effects on flux, wetting, and crystal growth. Importantly, MDC integration increased total water recovery to 62.5%, while mitigating membrane wetting and reducing the load on subsequent separation steps.

For selective recovery, a comparative study on lithium from highly concentrated solutions showed that VMD outperforms Direct Contact Membrane Distillation (DCMD) and Osmotic Distillation (OD) once supersaturation is reached, promoting crystallisation while minimising temperature polarisation and vapour-transport resistance. Under suitable operating windows, lithium crystals formed in multiple polymorphs, with VMD favouring more controlled growth kinetics [24].

In desalination-brine valorisation, X. Zhang et al. [25] reported that higher feed temperatures yielded larger crystal clusters, while longer crystallisation times produced more regular cubic crystals. For smallest crystal size, conditions of 50 °C feed temperature, 180 min crystallisation time, and aquarium salt feed were optimal; for the narrowest size distribution, 50 °C and 60 min using laboratory-grade NaCl were preferred. These results provide practical guidance for scaling MDC by tuning temperature and residence time to target desired crystal size distributions, reduce environmental impact, and improve brine management.

These studies demonstrate that MDC can handle high-salinity process streams and support ZLD while recovering valuable solids. However, previous investigations have mainly focused on common inorganic salts such as NaCl and lithium compounds. The selective crystallization and recovery of industrially relevant metal-bearing phases, particularly molybdenum, are still underexplored. In this thesis, VMD is used to concentrate molybdenum-bearing solutions to supersaturation, creates opportunities for sustainable molybdenum recovery from challenging metallurgical effluents.

1.3 Configurations of Membrane Distillation

Major research on MD has primarily focused on four fundamental configurations, distinguished by the mode of condensation downstream of the membrane, while commonly involving feed solution heating and evaporation at the upstream side. These configurations include DCMD, VMD, Air Gap Membrane Distillation (AGMD), and Sweep Gas Membrane Distillation (SGMD), each offering distinct operational characteristics and performance advantages. These configurations have been extensively studied with respect to their thermodynamic efficiency, mass and heat transfer dynamics, and suitability for various feedwater types. Emerging studies also emphasize hybrid designs and novel membrane materials to extend the operational stability and scalability of MD systems. The schematic of various configuration is shown in Figure *1* explaining the operation principles.

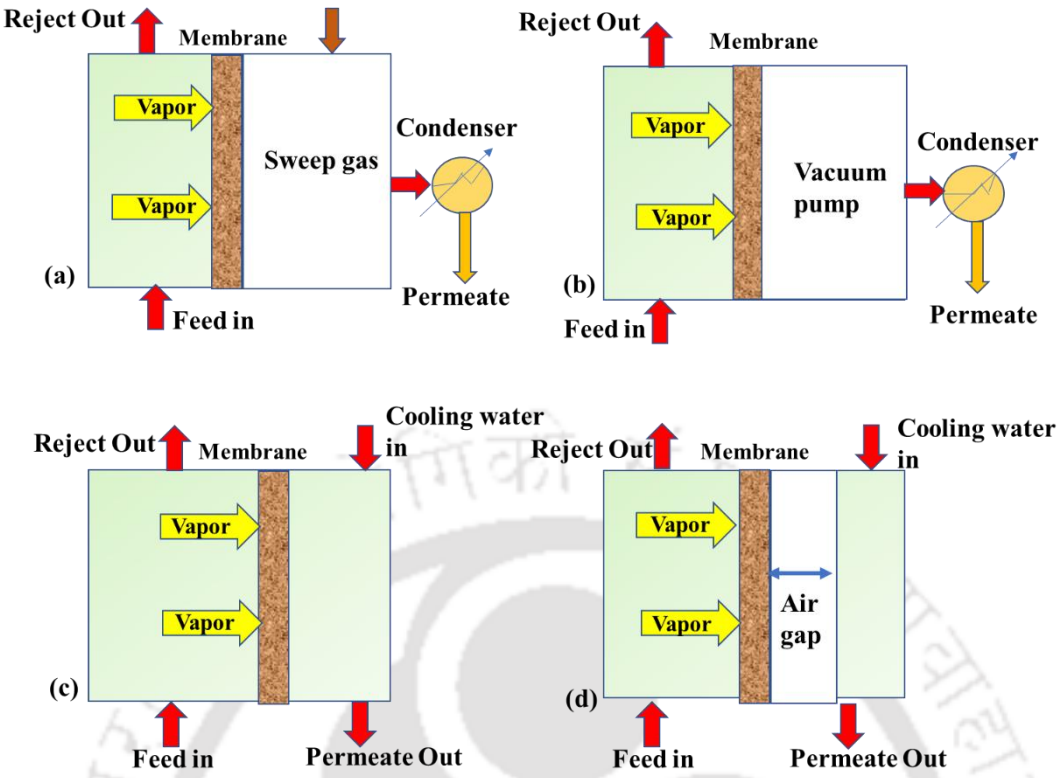

Figure 1 Configurations of MD (a) SGMD (b) VMD (c) DCMD (d) AGMD

1.3.1 DCMD

DCMD is the most studied configuration by the researchers climbing more than 50% contribution in the literatures, characterized by its simplicity and effectiveness. In this configuration, both hot and cold water are directly in contact with hydrophobic membrane which drives vapor through cold from hot side, the noteworthy problem is about the conduction loss accounts for 20-50% of the supplied thermal energy [6]. Typical operational temperatures range between 40–80°C on the feed side, while the permeate side is usually maintained at a significantly lower temperature, typically 20–40°C. This temperature difference generates the necessary vapor pressure gradient that drives mass transfer. DCMD efficiency and reduce specific energy consumption, which typically ranges from about 150 to 400 kWh/m³ of water produced when using conventional heating sources but can be significantly reduced when employing waste heat or solar thermal energy sources.

1.3.2 AGMD

AGMD configuration attempted to minimize the conduction loss by an introduction of air gap between membrane and condensation surface. In AGMD, heated feed water flows on one side of the microporous hydrophobic membrane, creating a vapor pressure gradient. Water vapor

crosses the membrane pores, driven by this gradient, and then traverses the stagnant air gap before condensing on a cooler plate or surface on the opposite side. The presence of the air gap significantly reduces heat conduction losses, enhancing thermal efficiency compared to DCMD. Notably, in AGMD permeate is condensed on a cold surface separated from direct membrane contact by an air gap. This unique feature makes AGMD particularly suitable for specialized applications where DCMD has limitations, such as the effective removal of volatile organic compounds (VOCs) from aqueous solutions. The lower heat loss results in improved energy efficiency, often making AGMD more attractive for processes that rely on renewable energy sources, such as solar or waste heat.

1.3.3 SGMD

SGMD configuration used a cold inert sweeping gas thereby condensing the vapor on the external condenser [7,8]. SGMD is characterized by the utilization of an inert gas typically air or nitrogen as a sweep medium on the permeate side of a hydrophobic microporous membrane. SGMD integrates the low conductive heat loss characteristic of AGMD with the reduced mass transfer resistance typical of DCMD. In SGMD, instead of a stagnant air layer separating the membrane and condensation surface, a continuous stream of inert gas is swept across the membrane surface to carry the vapor to an external condenser. This configuration enhances mass transfer efficiency and is advantageous for recovering volatile compounds and handling temperature-sensitive feed solutions.

Despite efforts to minimize mass transfer resistance and conductive heat loss, the overall performance of SGMD has remained relatively limited in terms of permeate flux. This is primarily due to the additional resistance introduced by the air gap and the sweeping inert gas. Moreover, the external condenser in SGMD systems faces a significant thermal load, as it must condense a small volume of vapor dispersed within a large volume of sweep gas. Consequently, the complexity and energy demand of the condensation step have restricted the practical application and broader investigation of SGMD, with relatively few studies reported in the literature. Notably studies by swaminathan et al[9] on novel MD configurations such as Permeate Gap Membrane Distillation (PGMD) and Conductive Gap Membrane Distillation (CGMD) have demonstrated significant improvements in energy efficiency. PGMD was shown to achieve up to 20% higher GOR than traditional AGMD, while CGMD, incorporating a thermally conductive material in the gap, achieved nearly twice the GOR of PGMD under the same conditions. The enhancement in CGMD is attributed to improved heat transfer across the

gap and more efficient internal energy recovery, particularly when operated in a counter-current configuration with respect to the coolant stream.

1.3.4 VMD

In VMD configuration, one side of the membrane is exposed to hot feed solution and the other side is subjected to reduced pressure using vacuum pump. The pressure is lower than the equilibrium vapor pressure of the corresponding feed[10]. This allows minimum conduction loss across the membrane and lower energy consumption for feed evaporation which in turn drives more vapor flux compared to all other configurations [11].

The vacuum significantly lowers the partial pressure on the permeate side, creating a substantial driving force for water vapor to permeate from the hot feed solution side, through the membrane pores, into the vacuum environment. Unlike other MD configurations, condensation of the vapor typically occurs externally in a separate condenser unit rather than directly adjacent to the membrane. VMD is particularly noted for achieving higher flux rates compared to other MD techniques due to the substantial vapor pressure gradient induced by the vacuum. Typical feed temperatures in VMD systems range from 40°C to 80°C, and vacuum levels are usually maintained at pressures between 1 to 50 kPa. This significant driving force often results in superior permeation performance and higher productivity, making VMD particularly efficient for desalination and concentration processes where rapid throughput is essential.

On the other hand, pore wetting is prevalent in VMD hence the applied hydraulic pressure and vacuum pressure should not exceed the Liquid Entry Pressure (LEP) of the membrane [12]. The detailed summary of the configurations with respect to the advantages and limitations are listed in the Table *1*.

Table 1: Advantages and Limitations of various configuration of MD

Configuration	Operational Type	Advantages	Limitations
DCMD	Feed and permeate in direct contact with the membrane surfaces	Simple design and ease of operation Suitable for small-scale systems	High conductive heat losses; this exhibits highest SEC as both feed and permeate in contact with membrane
AGMD	Air gap between membrane and condenser surface	Reduced heat losses due to air gap Lower risk of membrane wetting	More complex design and higher initial costs; Improved thermal effects with the cost of lower flux and module complexity
SGMD	Inert gas sweeps vapor away from permeate side	High vapor transport rate due to vapor removal Effective for volatile compound recovery Reduced heat conduction losses	Requires gas handling, higher complexity and operational costs; additional energy input for sweep gas circulation, compression and vapor condensation
VMD	Vacuum applied on permeate side of the membrane	High driving force leading to high fluxes Effective for concentration and crystallization	Requires vacuum pumps and condensers but comparatively better flux with lower SEC Risk of membrane wetting

1.4 Performance analysis and energy consumption in MD

MD holds greater potential to perform without compromising the flux for longer operation. Since the occurrence of fouling i.e. deposition of solute particles on the membrane surface is minimum in comparison with the existing pressure driven technologies like RO and FO. MD has shown greater resistance to both organic and inorganic fouling especially for the organic with steady flux[13].

In conventional RO, separation occurs primarily through size exclusion, where the pore size of the membrane is typically in the range of 0.1 to 1 nm to prevent the passage of dissolved solids. This small pore size, however, leads to significant deposition of solutes on the membrane surface, resulting in fouling and performance degradation over time. In contrast, MD is driven by a thermal gradient. Consequently, the pore size of MD membranes can be larger, typically in the range of 0.2 to 1 µm, without impacting the separation efficiency. This characteristic of

MD allows it to maintain superior performance with minimal deterioration of the membrane surface during water treatment and desalination operations[14].

Historically, the first MD experiment using a PTFE membrane with an average pore size of 9 µm recorded a permeate flux of 1 kg/m²·h, which is negligible compared to RO[15]. As a result, the focus on MD diminished in a short period. However, over the years, the customization of membrane manufacturing has advanced significantly. With higher porosities (up to 80%) and reduced thicknesses (close to 50 µm), the flux has increased by nearly 100-fold. A well improved operating conditions, membrane properties, fabrication, module design resulted in water flux of up to 80 kg/m²·h experimentally and up to 388 kg/m²·h theoretically were recorded, which are competitive to RO[16–18].

One of the key advantages of MD is its ability to utilize renewable energy sources such as solar energy, low-grade heat or industrial waste heat for operation. This capability results in a competitive STEC compared to conventional desalination methods, making MD more energy efficient option. For instance, studies have reported STEC values as low as 2 kWh/m³ for MD systems upon integrating it with waste heat, which is competitive with RO processes that typically consume around 3 kWh/m³ for seawater desalination. Further combination of PRO, MD and RO can drastically reduce the STEC up to 0.67 kWh/m³ for treating the brine solution[19–21]. The detailed electrical and thermal energy consumption of the membrane and thermal based technologies are highlighted in the Table 2.

Table 2: Energy consumption in membrane and thermal based technologies

Technology	**Electrical Energy (kWh/m^3)**	**Thermal Energy (kWh/m^3)**	**Operational Limitations**	**Reference**
RO	2-5.5	-	High fouling; limited to moderate salinity streams	[14]
FO	0.27	-	Complexity in draw regeneration	[22]
MSF	4	120	requires large infrastructure	[23]

MEMD	1.5-2.5	300	limited performance at small scales	[24]
MD	0.6-1.8	1700	Higher energy consumption; need to integrate with waste heat	[25]

1.4.1 Energy recovery potential in MD

MD generates valuable latent heat during the process. Recovering this latent heat through an Energy recovery device (ERD) can substantially improve the overall performance of the system. The recovered latent heat can be reused to preheat the incoming feed, which significantly reduces the energy costs associated with the process. Recent research on latent heat recovery shows great promise for scaling up this technology, with various ERDs and configurations being explored to optimize energy efficiency. Gained Output Ratio (GOR) is a commonly used performance metric in the literature, representing the ratio of the mass of latent heat recovered to the heat energy supplied to the system. In single-stage MD systems, the GOR is typically reported to be less than 1, considering the loses inside the membrane module. However, in multistage MD systems, the GOR can reach values as high as 12.1[26].

This significant improvement is due to the reuse of the generated steam in subsequent stages to preheat the incoming feedwater, thereby enhancing overall thermal efficiency. The most extensively studied configuration in the literature is DCMD, it has been reported that around 20–50% of the supplied thermal energy is lost solely through conduction. Additionally, significant efforts have been made to enhance membrane properties such as increasing porosity, thickness, and reducing tortuosity to minimize the conduction loss across the membrane[27,28].

AGMD inherently possesses the mechanism for recovering the latent heat. In this configuration, the condensation surface, air gap and the membrane forms sandwich like structure, which facilitates the continuous heating of fresh stream using the latent heat released during condensation. AGMD spiral wound module attained a GOR of 6.05 for study with tap water as feed source [29].

Multi effect membrane distillation (MEMD) is proposed to utilize the steam generated in the system for the subsequent stages till reaching the desired concentration of the solution. Upon

integrating this configuration, GOR of the system is drastically improved. M. Burhan, et al[30] investigated the performance of single and multi-stage mode of VMD system, the single effect mode has consumed 13.5 kW as input energy in comparison with 3.4kW energy in multi effect mode with a substantial improvement in the flux production.

1.4.2 Integration of MD with energy recovery device

The process integration of MD with various ERD have been extensively studied, including TEHP, HP, and VC with a focus on comparing the energy efficiency, GOR and COP among these integrations that governs the transfer of heat from one source to the other for heating and cooling applications.

A TEHP utilizes the Peltier effect to transfer heat between two materials, effectively both cooling and heating. By applying an electric current through a thermoelectric module, heat is absorbed on one side (cooling it) and released on the other side (heating it). This mechanism is particularly well-suited to the demands of MD, as it requires both heating the feed solution and cooling the permeate vapor. O. Makanjuola et al.[31] investigated the integration of TEHP with MD for an efficient desalination process. The integrated system demonstrated excellent salt rejection and significantly improved energy efficiency, achieving a STEC of 780 kWh/m^3, compared to 1700 kWh/m^3 typically consumed by standalone systems.

Additionally, the integration of TEHP led to a notable increase in the TP from 0.23 (typical of conventional DCMD) to 0.39 in the integrated system[32]. D.U. Lawal et al.[33] explored the combination of TEHP with AGMD, which eliminated the need for a cooling line, pump, and chiller. This integration enhanced energy efficiency, achieving an STEC of 962 kWh/m^3, showing promising potential for desalination applications.

A HP transfers heat from a lower temperature (low-grade side) to a higher temperature (high-grade side) using electrical power to drive a compressor, making it suitable for both heating and cooling applications. Additionally, VC are employed in MD to elevate the latent heat temperature generated in the system, the compressed vapor carries high pressure and temperature allowing more heat to be released to the incoming fresh feed. As a result, the overall energy efficiency of the system is significantly enhanced. E. Shaulsky et al.[34] developed a MD assisted with HP which improved the GOR of the overall system close to 60 which is highest ever reported in the literature with the flux of 60LMH highlighting the significance of HP.

The promising integration enabling ZLD through higher energy efficiency, low capital cost and modularity. A theoretical study by A. Khalifa et al.[35] on integrating the 2 kW HP with DCMD drastically reduced the STEC between 330 to 400 kWh/m³ with GOR of 2.1 and production cost of water decreased from 30 to 4 $/m^3$. Z. Si, et al. investigated the VMD system for treating the sulphuric acid solution, the result shown that concentrated up to 50% with the separation efficiency of 99.9% is achieved. In order to increase the energy efficiency of the process, the system is integrated with Mechanical Vapor Recompression (MVR) unit that ensured energy savings of 65.5% for the overall system[36]. Integration of HP with VMD proposed to cool the secondary vapor through evaporator and preheating the feed in the condenser section, result reveals that SETC close to 181.47 kWh/t, COP 3.44 with thermal efficiency of 63.31% respectively[37].

1.5 Advantages of integrating MD with technologies

Integrating MD with other membrane-based technologies such as RO, PRO, and FO has gained significant attention for enhancing energy efficiency, operational flexibility, and water recovery. The long-term challenges on brine discharge using RO, harvesting the energy recovery from PRO and regenerating the draw from FO can be addressed upon integrating these techniques with MD.

1.5.1 MD with RO

MD performs significantly for treating the highly concentrated brine with minimal fouling on the membrane surface which promises for the growing concern on RO brine discharge, the integration of MD with RO, treats both the concentrated brine and recovers the salt to enable the ZLD concept. MD is particularly effective in treating high-salinity brines and industrial effluents, where traditional membrane processes like RO face limitations due to osmotic pressure constraints. The ability of MD to handle such challenging feedwaters expands its applicability in achieving ZLD goals in various industries. Moreover, the modular and compact design of MD systems facilitates their integration into existing treatment infrastructures and enables decentralized water purification solutions.

1.5.2 MD with FO

The FO and MD hybrid configuration leverages FO's low-energy water extraction and MD's effective draw solution regeneration. FO technique draws water from the feed which turns it into the highly concentrated solution whereas the draw solution is diluted at the other end. The

recovery of draw solution can be addressed through integration with MD. FO draws water from the feed into a concentrated draw solution, which MD then dilutes while producing clean water. This integration is particularly advantageous for treating challenging wastewaters and utilizing low-grade heat sources

1.5.3 MD with Pressure Retarded Osmosis(PRO)

The PRO and MD hybrid system synergizes the energy generation capability of PRO with the high-rejection salt of MD. In this PRO and MD configuration, MD concentrates the draw solution diluted from the PRO, which then generates energy through the controlled mixing of solutions with different salinities. This closed-loop enhances both water recovery and harvests energy from the system. The summary of the integration is discussed in the Table 3.

Table 3: Integration of MD with other membrane technologies

System	Energy Use	Operational advantage	Application strength
MD-RO	Waste heat utilization	Robustness against high osmotic pressures	ZLD, industrial wastewater management
MD-FO	Reduced hydraulic energy, low thermal demand	Low fouling and minimal pretreatment requirements	Complex wastewater treatment, resource recovery
MD-PRO	Renewable energy generation from salinity gradients	Energy offsetting, high osmotic gradient exploitation	Renewable energy, sustainable desalination

1.6 Research Motivation

Industrial effluents are rising, and regulators are pushing ZLD. Conventional thermal routes (MSF, MED) are energy-intensive; pressure-/draw-driven membranes (RO, FO) face practical limits RO suffers fouling and trace solute leakage, FO needs energy-costly draw regeneration. MD addresses these gaps: it runs at moderate temperatures/near-ambient pressure, achieves near-complete rejection of non-volatile solutes, tolerates hypersaline feeds, and can be powered by low-grade or waste heat. Critically, MD naturally drives the retentate to supersaturation,

and the hydrophobic interface provides heterogeneous nucleation sites, enabling controlled crystallization and resource recovery within a ZLD flowsheet.

This motivation is concrete for molybdenum (Mo) recovery. In IOCL's slurry hydrocracking, oil-soluble Mo catalysts deactivate and accumulate in the heavy (>540 °C) pitch fraction (≈5–10 wt% of fresh feed), creating disposal and value-loss problems [1]. In parallel, spent hydrotreating catalysts are a major secondary source of Mo, V, Ni, and Co; growing volumes and tighter environmental norms make selective metals recovery both an economic and ecological imperative [2–6]. Solvent extraction (LLE) has demonstrated high-purity, scalable separations for Mo and co-metals across multiple case studies [7–11], while VMD can concentrate mother liquors to crystallization-ready states and integrate with external crystallizers for MDC.

In this thesis, VMD is positioned as a brine-concentrating and polishing step that can (i) produce high-quality distillate for reuse and (ii) drive the reject stream towards supersaturation, creating favourable conditions for downstream crystallisation and metal recovery.

Within this thesis, two application pillars are most relevant. First, desalination, where MD particularly Vacuum Membrane Distillation (VMD) serves as a brine-concentrating and polishing step that can push recoveries beyond the limits of seawater reverse osmosis and simplify compliance for challenging species. Second, resource recovery, where coupling MD with an external crystallizer i.e. Membrane Distillation Crystallization(MDC) leverages MD's ability to generate supersaturated retentates and provide heterogeneous nucleation sites at the membrane interface, enabling selective crystallization of salts and metal-bearing phases while advancing ZLD objectives [22–25]. The following subsections detail these two pathways, Desalination, and Resource Recovery and motivate their integration for molybdenum recovery in this work.

This thesis is motivated by the opportunity to combine VMD/MDC with targeted solvent-extraction steps to (i) recover water at high quality, (ii) concentrate and crystallize valuable salts/metal species, and (iii) close loops consistent with ZLD first demonstrated on molybdate analogues and then translated to Mo-bearing streams from petroleum and pharmaceutical effluents.

Objectives

- Design and optimize an energy-efficient HF-VMD module for high-salinity, metal-bearing streams.
- Improve thermal performance via latent-heat recovery (TEHP/HP)
- Map operating variables (temperature, vacuum pressure, flow, concentration) that maximize flux, minimize wetting/scaling, and promote controlled crystallization.
- Demonstrate selective Mo recovery by coupling concentration/crystallization with solvent extraction; benchmark water/metal recoveries and specific energy use.

1.6.1 Importance of developing a mathematical model for VMD

The mathematical model for the HF-VMD system is a crucial component for designing and optimizing HF-VMD modules. These models are essential for optimizing process operating conditions and must be highly accurate and adaptable to various configurations, lengths, and operating conditions of HF-VMD modules. Developing such a model requires a comprehensive understanding of the underlying physics within the membrane module. Therefore, researchers have focused on developing first-principle models based on mass, energy, and momentum balances, along with membrane transport models, to achieve broader applicability and greater accuracy. A well-formulated model supports the evaluation of design parameters such as fibre length, vacuum level, and flow rates under varying feed compositions and thermal inputs. Additionally, it facilitates sensitivity analysis, enabling researchers to identify the most influential factors governing system performance. This in turn guides material selection, module fabrication, and process integration, especially when coupled with energy recovery systems like TEHP, HP and multistage configurations. As VMD gains attention for its applications in high-salinity brine treatment, concentration, and crystallization, robust models are indispensable for exploring phase boundaries, scaling thresholds, and fouling risks under extreme conditions. With the growing emphasis on ZLD and resource recovery, mathematical models are becoming central to optimizing the trade-offs between energy input, water recovery, and material recovery.

1.7 Summary and scope of research

Based on the overall discussion, it can be concluded that MD has the significant potential for solute rejection and can be integrated with low grade energy sources. Also, the scope for recovering the latent heat from the MD is discussed shows a promise for sustainable solution for the process industries to incorporate. In comparison with the conventional technologies like RO and FO, MD has superior performance in producing pure vapor and theoretically complete

rejection of solute. However, despite the advantages, the scaling and commercialization is still lagging due to the energy consumption and low productivity. The present thesis aims to provide further insight in developing an integrated MD system with ERD to minimize the energy consumption and energy pinch analysis to maximize the productivity of the MD system. The developed system promises to advance its future in the process industries.

1.8 Novel contributions of this thesis

- A 1-D coupled heat–mass–momentum transport model for HF-VMD built in DYMOLA, capable of predicting flux, polarization effects, and pressure drop simultaneously under varying operating conditions.
- Model validation using a commercial ePTFE HF-VMD module, covering a wide range of feed temperatures, flow rates, vacuum pressures, and salinities.
- Module-level design optimization, demonstrating that reduction of membrane length from 1 m to 0.1 m can improve flux by nearly 30 times at 343 K by minimizing thermal losses.
- First systematic integration study of VMD with multiple energy recovery devices (TEHP, HX, VC, HP), including energy pinch analysis to quantify latent-heat utilization.
- Demonstrated energy savings up to 86% using heat-pump integration, indicating strong feasibility for process scale-up.
- Application of VMD for resource recovery, achieving 99.99% rejection of sodium molybdate and demonstrating supersaturation inside the membrane for future crystallization studies targeting molybdenum recovery.

1.9 Scope of thesis details

- The experimental and modeling investigations in this thesis focus on aqueous inorganic solutions, specifically sodium chloride and sodium molybdate as representative solutes for desalination and heavy-metal resource recovery. In specific, mathematical model validated with actual experiment on pure and salt water concentration of up to 35g/L.
- All process studies are performed using a commercial ePTFE HF VMD module with pore size, porosity, and thickness provided in Chapter 4, Table 12. The membrane transport model is developed and validated exclusively for this membrane type.

- The experimental system corresponds to a laboratory-scale single-module setup with maximum membrane length of 1 m and feed flowrates up to 650 L/h, as detailed in Chapter 4 and Chapter 5 respectively.
- Energy integration is attempted theoretically with recovery equipment such as TEHP, VC, HX and HP respectively. The detailed energy consumption and the scope of recovery is studied through mathematical model.
- Long-term operational aspects such as fouling / wetting durability, chemical cleaning, and pilot-scale multi-module configuration remain outside the scope of this thesis and are identified as prospective future work in Chapter 6

1.10 Organization of the thesis

This thesis is organised into six (06) chapters, and a brief overview of each chapter is given below.

Chapter 1: Introduction

This chapter provides a general overview of existing techniques used to recover molybdenum from spent and heavy fraction residues and the role of different solvents in the extraction process. It is followed by a brief discussion on the fundamentals of MD process to understand the present status in metal ion concentration and separation as purified form. It also outlines the challenges in energy consumption aspects of MD and emerging technologies that can enhance the energy efficiency of the overall integrated system, followed by motivation associated with studies conducted in this thesis.

Chapter 2: Literature review and Objectives

This chapter is aimed to provide a detailed literature review on the following aspects:

- Hydro and pyrometallurgy techniques used in the extraction of heavy metal ion from the spent catalyst and heavy fraction residue.
- Extraction of the targeted metal ion from the organic to aqueous phase using different category of solvents
- A state of the art of fundamental principles and application of MD in process industries
- The significance of the MD technology in concentration and crystallization application
- Potential opportunities on energy recovery from the MD system for scaling up this technology

- Process Integration of VMD with TEHP for effective condensation and heating the feed stream
- Pinch analysis study on integrating the VMD system with heat exchanger, heat pump, vapor compressor and techno economic study

From the outcome of the literature survey, the prominent research gaps were identified to frame the objectives of the present research work at the end of this chapter.

Chapter 3: Theory

In this section, a one-dimensional mathematical model was developed to study the performance of VMD system. The developed 1-D HF-VMD model was validated with the actual experimental conditions. A brief discussion on membrane module optimization and process parameter estimation were discussed.

Chapter 4: Materials. Methods and Experimental Procedure

This chapter details all the analytical procedures and protocols employed in characterization of the pitch. This section also details the methodologies and experimental procedures used for studying the VMD system to understand its performance for ground water and rock salt solution concentration. It also describes the experimental set up used for the TEHP system study.

Chapter 5: Results and Discussion

This chapter reports the detailed interpretation and discussion of the results obtained from characterization of pitch followed by both the theoretical and experimental work conducted for the studying the performance of VMD system and exploring the potential for concentration and crystallization applications. It also details the feasibility of integrating the low cost TEHP for heating and cooling applications in VMD system. Further, to enhance the overall energy efficiency of the system energy recovery equipment such as HP, HX and VC were also systematically studied through mathematical modelling.

Chapter 06: Conclusion and scope of future work

Chapter 02

Literature review and objectives

2 Literature review and objectives*:*

This chapter aimed to provide an in-depth review on the fundamentals of the MD focus on theoretical modelling, membrane characteristics, system performance, energy demands and opportunities for latent heat recovery using ERD and the overall performance enhancement of the integrated system. This review also outlines the solvent extraction techniques for the recovery of metal ion. Based on the reviewed literature, critical literature gaps were identified and the detailed discussion presented in the subsequent chapters.

2.1 Historical perspective of Membrane Distillation

An early conceptualization of MD was patented by Bodell in 1966, outlining an apparatus and method for converting non-potable aqueous fluids into potable water. However, the invention lacked quantitative performance data. Building on this foundation, Weyl (1967) significantly enhanced the desalination process by introducing a novel approach utilizing an air-filled, porous, hydrophobic membrane. He demonstrated that such a membrane could effectively operate in a vapor pressure-driven system to recover demineralized water from saline feed solutions. This pioneering setup achieved a permeate flux of approximately 1 $kg/m^2 \cdot h$, establishing a critical framework for subsequent advancements in MD technology[15]. With advancements in membrane manufacturing technologies, MD has witnessed renewing interest due to improvements in module design and a better understanding of key factors such as Concentration polarization (CP) and Temperature polarization (TP), both of which significantly affect permeate flux. The growing interest in MD is also supported by its process flexibility and the integration of core engineering principles, making it a promising option for sustainable separation applications[38].

Standardized terminologies and fundamental criteria for MD were established by a dedicated committee during an MD workshop and later compiled by smolders et al.[39] The committee identified five essential conditions that a membrane must fulfil to perform effectively in MD applications.

i. The membrane must be porous, allowing vapor-phase transport through its structure.

ii. The membrane must resist wetting by process liquids to maintain phase separation between liquid and vapor.

iii. Capillary condensation within the membrane pores must be avoided to ensure uninterrupted vapor transport.

iv. The membrane must not alter the vapor–liquid equilibrium of the components in the process liquid.

v. At least one side of the membrane should be in direct contact with the process liquid.

2.2 Fundamentals of Membrane Distillation

MD is a thermally driven separation process that operates at relatively low pressures, typically in the range of a few kilopascals. These low operating pressures contribute to lower equipment costs and improved operational safety compared to conventional pressure-driven membrane processes. Since MD relies on vapor–liquid equilibrium for separation, it can theoretically achieve complete rejection of non-volatile solutes, making it particularly suitable for high-purity water production and the concentration of dissolved species. MD is implemented in four primary configurations namely DCMD, AGMD, SGMD, and VMD. DCMD is the most studied reported in the literature among other configurations where both feed and permeate streams are in direct contact with the membrane, offering operational simplicity. However, a major drawback of DCMD is its significant conductive heat loss through the membrane material, which account for approximately 20–50% of the supplied thermal energy, thereby reducing overall process efficiency. AGMD configuration attempted to minimize the conduction loss by an introduction of air gap between membrane and condensation surface while SGMD configuration used a cold inert sweeping gas thereby condensing the vapor on the external condenser. Despite the effort to reduce the mass transfer resistance and conduction loss, the system's performance was relatively less in terms of flux due to an additional resistance on air gap and inert gas. Among these, VMD stands out for its superior performance. By applying a vacuum on the permeate side, VMD maximizes the vapor pressure gradient, resulting in higher permeate flux and more efficient separation, further an external condenser allows for an efficient latent heat recovery.

2.2.1 Vacuum Membrane Distillation

An effective strategy to enhance membrane permeability in MD is to eliminate the air trapped within the membrane pores either through deaeration or by maintaining a continuous vacuum on the permeate side. This approach reduces the partial pressure of non-condensable gases, thereby minimizing molecular diffusion resistance and increasing the driving force for vapor transport across the membrane. Among the conventional MD configurations, VMD typically delivers the highest permeate flux. This is primarily due to the continuous removal of air from the membrane pores via a vacuum pump, which significantly enhances the vapor pressure

gradient. VMD also benefits from reduced conductive heat loss, as there is no direct contact with a cold liquid on the permeate side, and it avoids additional mass transfer resistance associated with gaps or sweep gases.

A key operational advantage is that the applied permeate pressure is maintained below the saturation pressure of the target volatile components, facilitating efficient vapor transport. Additionally, condensation occurs externally, outside the membrane module, allowing for better thermal management and easier integration with energy recovery systems. The schematic of heat and mass transport through the membrane is shown in Figure 2. In VMD, the hydrophobic nature of the membrane prevents the liquid feed from penetrating into the membrane pores, provided that the transmembrane hydrostatic pressure remains below the membrane's liquid entry pressure (LEP). To maintain selective vapor transport and prevent pore wetting, the system must be operated within this critical pressure range, ensuring that the applied vacuum does not exceed the LEP threshold.

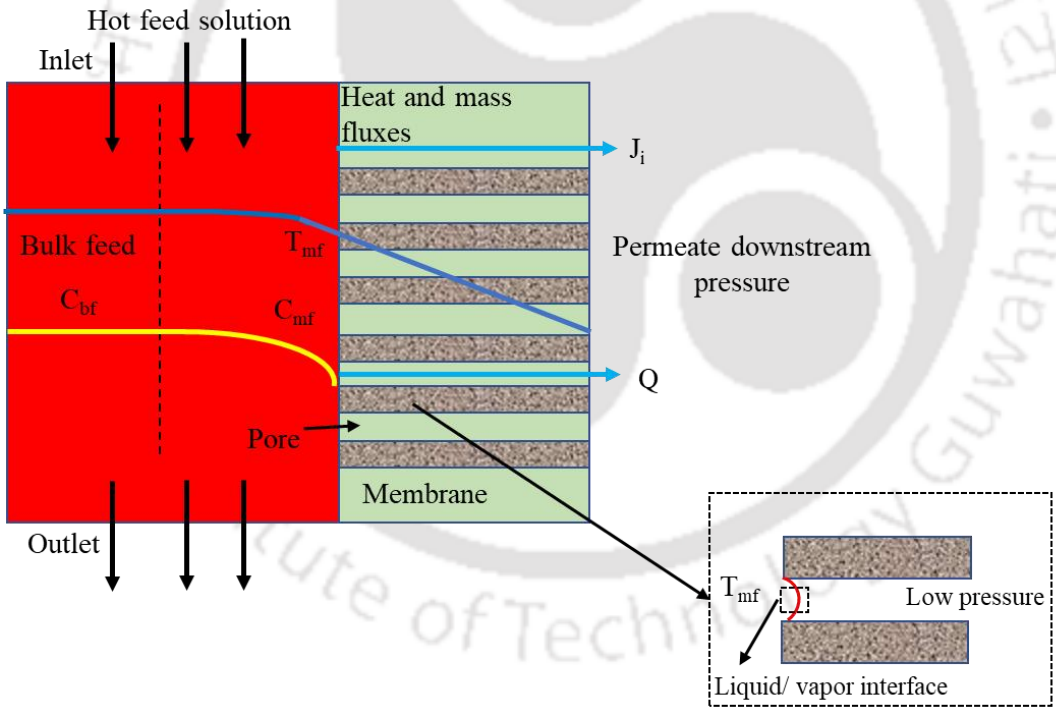

Figure 2 Schematics of heat and mass transport through hydrophobic membrane

2.3 Membrane characteristics

Membrane selection is a critical factor influencing the separation performance in MD. The membrane must inherently exhibit hydrophobicity and adequate porosity to enable vapor transport while preventing liquid water intrusion. While many commercially available membranes meet these basic criteria, the overall efficiency of the MD process is also governed by additional properties such as mass transfer resistance, thermal stability, thermal conductivity, resistance to wetting, and compatibility with module configurations[40]. This section provides an overview of the key membrane and module characteristics that guide the selection of appropriate membranes for specific MD applications.

2.3.1 Membrane materials

A wide variety of membranes, encompassing both polymeric and inorganic hydrophobic types, have been employed in MD processes. Among these, polymeric membranes have attracted significant attention due to their tunable intrinsic properties, which enable performance optimization through adjustments in porosity, hydrophobicity, and thermal behaviour. Microporous polymeric membranes for MD can be fabricated using techniques such as phase inversion, stretching of dense polymer films, and thermally induced phase separation[41]. Additionally, hydrophilic membranes that are subsequently surface-modified to impart hydrophobicity have also demonstrated successful application in MD. These fabrication approaches aim to develop membranes with suitable pore structures, surface characteristics, and thermal stability necessary for efficient vapor transport and separation in MD systems.

Polytetrafluoroethylene (PTFE), Polypropylene (PP) and polyvinylidene fluoride (PVDF) are the most commonly used polymeric membranes due to their low surface tension values. It can be prepared through different techniques such as stretching, sintering, phase inversion or thermally induced phase separation depending on the properties of the material to be used[42]. The detailed surface tension and surface energy are discussed in Table 4. PTFE membranes are the most hydrophobic ones showing outstanding thermal stability and chemical resistance properties. The main advantage of PTFE membranes is the difficulty of processing and mostly prepared by sintering and stretching. PP exhibits excellent solvent resistant properties and high crystallinity. PVDF membranes exhibit good thermal and chemical resistance however this polymer easily dissolves at room temperature in a variety of solvents[43].

Table 4 Physical properties of different membrane materials

Material	Surface Tension (mN/m)	Surface Energy (dynes/cm)	Contact Angle with Water (deg)	Thermal Conductivity (W/m·K)
PTFE	18	18–22	110–120	0.25
PVDF	25	30–35	85–95	0.19
PP	30	30–34	90–100	0.22

There are some additional criteria that should be taken into considerations for the appropriate selection of the membrane such as pore size, tortuosity, porosity, membrane thickness and thermal conductivity.

2.3.2 Membrane pore size

Membranes with pore sizes ranging from 10 nm to 1 µm are suitable for MD applications. When selecting the appropriate pore size, two key factors must be considered.

i. The pores must be sufficiently small to prevent liquid intrusion under the specified operating conditions, maintaining membrane integrity and preventing wetting.
ii. The pores must be large enough to allow adequate vapor transport, thereby ensuring the desired permeate flux.

As a result, an optimal pore size must be carefully determined for each MD application, considering the nature of the feed solution and the operating conditions.

2.3.3 Membrane Porosity and Liquid Entry Pressure

Membrane porosity is defined as the ratio of the pore volume to the total volume of the membrane. Higher porosity increases the effective evaporation surface area, which enhances vapor transport and consequently results in improved permeate flux. However, porosity also influences thermal performance, as it can lead to heat loss by conduction through the membrane matrix. Therefore, optimizing porosity is essential to balance mass transfer efficiency and thermal losses in MD.

LEP is the minimum pressure required for a liquid to penetrate a hydrophobic membrane. To prevent membrane wetting, the operating pressure must remain below the LEP. LEP is primarily influenced by the membrane's maximum pore size, the liquid's surface tension (γ), and the contact angle (θ) between the liquid and the membrane surface. It can be estimated using the equation (2-1).

$$LEP = \frac{-2B\gamma cos\theta}{r} \quad (2\text{-}1)$$

where *B* is a geometric factor, and *r* is the largest pore radius. Membranes with smaller pore sizes, higher surface tension, and greater hydrophobicity exhibit higher LEP, which is essential for stable and effective membrane distillation.

2.3.4 Pore tortuosity

Tortuosity is the ratio of the actual vapor path length through membrane pores to the membrane thickness. Since membrane pores are typically irregular and winding, higher tortuosity increases mass transfer resistance and reduces permeate flux. Membranes with lower tortuosity enable more efficient vapor transport, enhancing flux. Additionally, tortuosity influences thermal transport, as highly tortuous structures can increase solid-phase contact and elevate conductive heat losses[44]. Advances in membrane fabrication techniques, such as electrospinning and 3D structuring, are increasingly aimed at controlling pore geometry and reducing tortuosity for improved MD performance.

2.3.5 Membrane thickness and pore size distribution

To balance permeate flux and conductive heat loss, membrane thickness must be carefully optimized in MD system. While thinner membranes are desirable for enhancing vapor transport and achieving higher flux due to reduced diffusion resistance. On the other hand, increasing membrane thickness reduces thermal losses but introduces additional mass transfer resistance, resulting in reduced flux[38].

Pore size distribution plays a crucial role in determining the uniformity and stability of vapor permeation in MD. Generally, a uniform pore size is preferred over a broad distribution, as it ensures consistent vapor transport across the membrane surface and minimizes localized variations in flux[45]. Non-uniform or widely distributed pore sizes can lead to uneven vapor flow, and poor separation performance.

2.3.6 Thermal conductivity

The thermal conductivity of the membrane is a critical parameter in MD, as it directly influences conductive heat losses from the feed side to the permeate side. To minimize this heat transfer and improve thermal efficiency, membranes with low thermal conductivity are preferred. One promising strategy is to increase membrane porosity, thereby reducing the

proportion of solid polymer matrix and increasing the presence of air or vapor both of which have much lower thermal conductivity than solid polymers. This shift lowers the effective thermal conductivity of the membrane.

Typically, the thermal conductivity of polymers used in MD falls within the range of 0.15 to 0.45 $W \cdot m^{-1} \cdot K^{-1}$, depending on factors such as temperature and the degree of polymer crystallinity. Since the thermal conductivity of water vapor within the pores is significantly lower (around 0.02 $W \cdot m^{-1} \cdot K^{-1}$), increasing the vapor phase fraction through high porosity can significantly reduce overall heat loss. However, care must be taken to ensure that the structural integrity and mechanical strength of the membrane are not compromised when optimizing for thermal properties.

2.4 Membrane modules configuration

In MD literature, the selection of membrane module configurations is often guided by both engineering parameters and economic considerations. The most commonly studied configurations include plate-and-frame, spiral wound, tubular, capillary, and hollow fibre modules. Each configuration presents distinct advantages depending on the application context. Plate-and-frame modules offer ease of cleaning and membrane replacement, making them suitable for laboratory and small-scale applications. Spiral wound modules are compact and efficient but are more prone to fouling. Tubular modules provide robustness and are ideal for treating viscous or particle-laden feeds. Capillary and hollow fibre configurations offer high packing density and are widely investigated for their superior surface area-to-volume ratios, which enhance mass transfer efficiency in MD systems. These configurations continue to be evaluated for their performance, scalability, and cost-effectiveness in various MD applications.

2.4.1 Plate and frame module

The plate and frame module is the simplest and most configuration used in MD systems. It consists of flat sheet or disc-shaped membranes sandwiched between two plates, with appropriate spacers to facilitate feed and permeate flow. This design allows for easy assembly, disassembly, cleaning, and membrane replacement, making it ideal for laboratory studies and pilot-scale applications. Polymeric flat sheet membranes used in this configuration are easy to fabricate, handle, and mount. Additionally, these membranes can be mechanically supported to improve structural integrity under varying pressure and thermal conditions. However, a key limitation of this module is its relatively low packing density, typically ranging from 100 to

400 m^3/m^2, which affects space efficiency and scalability in industrial applications. Studies have shown that with proper flow channel design and module optimization, water fluxes in the range of 10–13 $kg/m^2 \cdot h$ can be achieved under DCMD mode[46].

2.4.2 Hollow fibre module

The HF module is widely recognized for its exceptionally high packing density, which can reach up to 3000 m^2/m^3, making it the most space-efficient configuration among MD modules. HF modules consist of numerous fine capillary membranes enclosed within a tubular shell sealed at both ends. In typical operation, the feed flows either inside the hollow fibres with the permeate collected on the shell side, or vice versa, depending on the process design. This configuration allows for compact design and high surface area utilization, contributing to relatively low energy consumption per unit of water produced. From an economic perspective, HF modules are also advantageous due to their cost-effective mass production and the potential for high-pressure operation, withstanding pressures exceeding 100 bars. However, a significant drawback of HF membranes is their susceptibility to fouling, particularly due to the narrow internal diameter of the fibres, which complicates cleaning and maintenance. As such, pre-treatment of feed water to remove macromolecules and particulates is essential to enhance MD flux and maintain long-term performance. Effective fouling control remains a critical challenge for the widespread adoption of HF modules in MD systems [47]. J-H. Tsai et al. [48]investigated a multi-pass HF module for MD. Their results revealed that while the conventional single-pass configuration achieved higher permeate flux, the multi-pass design demonstrated superior energy efficiency. Specifically, the novel configuration consumed approximately 35% less thermal energy compared to the traditional single-pass module of equivalent length, highlighting its potential for energy-optimized MD applications.

Despite their high surface-area-to-volume ratio and compact module design, HF membrane configurations also present certain limitations. The small lumen diameter and dense fiber packing can increase susceptibility to fouling and scaling, particularly under high-salinity or supersaturated operating conditions. Cleaning of HF modules is more challenging compared to flat-sheet configurations due to limited access to individual fibers and the risk of fiber breakage during aggressive backwashing or chemical cleaning. In addition, localized wetting may occur if crystallization or fouling initiates at the fiber inlet or membrane surface, potentially compromising long-term stability. These limitations highlight the importance of appropriate

hydrodynamic design, operating below critical wetting conditions, and implementing suitable cleaning strategies when employing HF membranes in MD systems.

2.4.3 Spiral wound module

The spiral wound membrane module is a compact configuration widely used in pressure-driven membrane processes and has been adapted for MD applications. In this design, the membrane sheets, feed and permeate spacers, and a porous membrane support are assembled into a flat-sheet envelope. This envelope is then spirally wound around a perforated central collection tube and housed within an outer tubular pressure vessel. During operation, the feed solution flows axially along the feed channel, while the permeate is collected through the central tube after passing across the membrane. This module offers a moderate packing density, typically ranging from 300 to 1000 m^2/m^3, which balances performance and footprint. The compact design allows for efficient space utilization and has been considered for scaling up MD systems[49]. However, a major limitation of this module type is its sensitivity to membrane fouling, particularly due to the narrow flow paths and limited accessibility for cleaning. Therefore, maintaining feed water quality and implementing effective pre-treatment protocols are critical to sustaining long-term performance in spiral wound MD systems.

A well-designed membrane module in MD should facilitate efficient heat and mass transfer between the bulk solution and the membrane interface. The overall performance and productivity of the MD process are often constrained by resistances to heat and mass transfer within the boundary layers on both the feed and permeate sides. These boundary layers can create temperature and concentration polarization effects, which reduce the effective driving force across the membrane. Therefore, optimizing module design to minimize these resistances is critical for enhancing water vapor flux and improving the overall efficiency of the MD process[50].

2.5 Mathematical model development in MD

The mathematical model for the MD system is a crucial component for designing and optimizing the modules. These models are essential for optimizing process operating conditions and must be highly accurate and adaptable to various configurations, lengths, and operating conditions. Developing such a model requires a comprehensive understanding of the underlying physics within the membrane module. Therefore, researchers have focused on developing first-principle models based on mass, energy, and momentum balances, along with membrane transport models, to achieve broader applicability and greater accuracy.

In first-principle models, the modelling approach varies depending on the size, and configuration of the module. For instance, in test cells where there is minimal variation in process parameters along the membrane, it is often assumed that these parameters are nearly uniform. Therefore, researchers have adopted lumped steady-state models that use mass balance across the membrane, incorporating membrane transport models[18,51–53]. To account for concentration polarization, and temperature polarization effect across the membrane, different transport theories were employed. For membrane transport, Knudsen, and Poiseuille flow models are widely used. Some researchers exclusively used the Knudsen model[54–60], while a few combines both in a resistance-in-series approach to achieve a more accurate membrane transport model[61,62].

Accurately predicting the temperature at the membrane surface requires considering both mechanisms; otherwise, discrepancies between predicted and actual temperatures at membrane surface can occur. Neglecting concentration polarization may lead to overestimated vapor pressure. Researchers have developed various models, integrating these factors to different extents[53,63,64], but extending these models to distributed systems like long-length HF modules remains challenging. Further, studies focus on developing a one-dimensional (1D) model to achieve more accurate predictions. Many studies have reported that this approach improves model accuracy for HF modules compared to lumped steady-state models[61,65–67]. However, neglecting conduction can lead to introducing errors on estimated model parameter such as tortuosity, and coefficients of mass and heat transfer correlation. Also, the exclusion of these effects will lead to bias on model parameters i.e. increasing errors in correlation coefficients. Thus, models that integrates the mathematical equation for mass, energy, and momentum balance along with membrane transport, concentration polarization and temperature polarization are expected to be more accurate and suitable for reliable modelling and optimization applications. Recently, researchers have attempted to develop 2D and 3D models to account for variations in temperature and concentration along radial and angular directions[54,63,68–76]. However, for axial flow HF-MD modules, radial variations are negligible, rendering 2D and 3D models are computationally intensive and impractical for real-time process optimization and design applications. Validation of these models plays a critical role in ensuring their accuracy. Traditionally, model validation has focused primarily on flux measurements[52,62,77–80].

Recent advancements in MD have explored various configurations including flat sheet, spiral wound and HF membranes to evaluate performance under diverse operating conditions.

Theoretical study has achieved the highest flux of 388 L/h using PTFE flat sheet membrane at the for the length of 1m at the best operating conditions and by performing optimization of modelling parameters[16], but often lack comprehensive experimental validation. Further, substantial literatures have addressed the detailed heat, and mass transport phenomena in membrane[18,59] yet lacks to address the momentum balance and spatial variations in mass and energy transport along the module length. In MD, membrane length is a critical parameter which predominantly governs the flux. Membrane module which has lower area, and length have significantly reported the higher flux[51,56], as energy loss is minimum across the module. The detailed summary of the literature review consist of governing heat and mass transport phenomena with concentration and temperature polarization and membrane performance are given in the Table 5.

Table 5: Summary of Reviewed Literature Pertaining to the Modeling Experimental Study on MD System

MC	MaB	EB	MB	Membrane Transport		CPC	TPC	CL	Model Calibration			ML (m)	MA (m^2)	Flux (LMH)	Model	MM	Ref
				KD	PD				Flux	RT	RP						
HF	✔	✔	✕	✔	✕	✕	✔	✕	✔	✔	✕	0.064	0.0251	71	0D	PP	[51]
HF	✔	✔	✕	✔	✕	✕	✕	✕	✔	✕	✕	0.47	0.1	80	0D	PP	[18]
FS	✔	✔	✕	✔	✕	✕	✕	✕	✔	✕	✕	0.7	1	388	0D	PTFE	[16]
HF	✔	✔	✕	✔	✔	✕	✕	✕	✔	✕	✕		0.015	9	0D	PP	[52]
HF	✔	✔	✕	✔	✕	✕	✕	✔	✔	✕	✕	0.47	0.1	26	2D	PP	[54]
HF	✔	✔	✔	✔	✕	✕	✕	✔	✔	✔	✕	0.2	0.018	32.4	1D		[56]
HF	✔	✔	✕	✔	✕	✕	✔	✕	✔	✕	✕	0.25	0.0084	9.25	0D	PP	[57]
HF	✔	✔	✕	✔	✔	✕	✔	✔	✔	✕	✕	0.25		40	1D		[61]
FS	✔	✔	✕	✔	✔	✕	✕	✕	✔	✔	✕		0.037	32	1D	PTFE	[62]
HF	✔	✔	✔	✔	✕	✔	✔	✕	✔	✕	✕	0.47	0.0017	5.8	3D	PP	[64]
FS	✔	✔	✕	✔	✔	✕	✔	✕	✔	✕	✕	0.1	0.005	10	0D	PTFE	[53]
FS	✔	✔	✔	✔	✕	✕	✕	✕	✔	✕	✕	0.47		25	1D	PP	[65]
HF	✔	✔	✕	✔	✕	✕	✕	✕	✔	✕	✕	0.28		30	1D	PVDF	[66]
HF	✔	✔	✔	✔	✔	✕	✕	✕	✔	✕	✕	0.2	0.006	1	1D	PP	[67]
HF	✔	✔	✕	✔	✕	✕	✕	✕	✔	✔	✕	0.2		25	2D	PP	[68]
HF	✔	✔	✔	✔	✔	✕	✔	✔	✔	✔	✕	0.25	0.057	45	3D	PTFE	[69]
FS	✔	✔	✕	✔	✕	✔	✕	✕	✔	✕	✕	0.48	0.16	14	0D	PTFE	[77]
FS	✔	✔	✕	✔	✕	✔	✕	✕	✔	✕	✕	0.46	0.005	21	1D	PTFE	[78]
HF & FS	✔	✔	✕	✔	✕	✕	✕	✕	✔	✕	✕		0.1	9	1D	PP	[79]
HF	✔	✔	✔	✔	✔	✔	✔	✔	✔	✔	✔	1	1	9.2	1D	ePTFE	PW

MC – Module Configuration, MaB- Mass Balance, EB- Energy Balance, MB-Momentum Balance, KD-Knudsen Diffusion, PD- Poiseuille Diffusion, CPC- Concentration Polarization Co-efficient, TPC- Temperature Polarization Co-efficient, CL- Conductive Loss, RT- Reject Temperature, RP- Reject Pressure, ML- Membrane Length, MA- Membrane Area, MM- Membrane Material

Table 6 Summary of the literature on HP/TEHP/VMD system

Theory (✓/✕)	Experiment (✓/✕)	IM	ERU	Heating	Cooling	WF (L/m^2.h)	SEC (kWh/m^3)	GOR	PC (kW)	Year	Reference
✓	✕	VMD	HE	✓	✕	140.4	225	-	-	2015	[81]
✓	✕	VMD	HP	✓	✓	9	142.89	19.92	-	2024	[82]
✓	✕	DCMD	VC-HP	✓	✓	60	10	60	-	2020	[34]
✓	✕	DCMD	HP	✓	✓	90	400	2.1	2	2021	[35]
✓	✕	VMD	HP	✓	✓	4	4.67	-	0.48	2020	[83]
✓	✓	VMD	MVR	✓	✕	1.7	202.2	11	16.8	2022	[84]
✕	✓	SGMD	TEHP	✓	✓	-	10000	-	0.85	2018	[85]
✕	✓	DCMD	TEHP	✓	✓	48	662	-	-	2024	[86]
✓	✕	DCMD	TEHP	✓	✕	240	217	3.24	-	2024	[87]
✕	✓	AGMD	HP	✓	✓	0.8	25	1.6	-	2021	[88]
✓	✓	DCMD	HE	✓	✓	2	670	0.942	-	2020	[89]
✓	✓	-	TEHP	✓	✓	0.0418	-	0.81	0.045	2021	[90]
✓	✓	EPSCD	TEHP	✓	✓	10	780	-	0.02	2021	[91]

ERD- Energy Recovery Unit, SEC- Specific Energy Consumption, GOR- Gained Output Ratio, IM- Integrated Module, WF-Water Flux, PC-Power Consumption

2.5.1 Heat Transfer in Membrane Distillation

Heat transfer models in MD are essential for characterizing the thermal behaviour near the membrane interface and for predicting interface temperatures that directly influence process efficiency. These models also complement mass transfer models by providing key inputs such as the average membrane temperature and interfacial vapor pressures for accurately estimating vapor flux. In MD, the overall heat transfer process comprises three primary steps and a schematic shown in Figure 3.

1. Heat transfer through the feed-side boundary layer, where thermal energy is transferred from the bulk feed to the membrane surface.

2. Heat transfer across the membrane, which involves both conductive heat loss through the membrane material and latent heat carried by vapor molecules.

3. Heat transfer through the permeate-side boundary layer, where heat is removed by the condensing vapor or a cooling medium. In a thermally equilibrated membrane distillation (MD) module, the heat flux through the feed channel, membrane, and permeate channel must be equal under steady-state conditions. This thermal balance is represented by equations (2-2) to (2-4) respectively, ensuring consistency in energy transfer across all transport domains.

Heat transfer through the feed side boundary layer can be calculated using

$$Q_f = h_f\left(T_{fb} - T_{fm}\right) \tag{2-2}$$

Wherein h_f is the feed side heat transfer co-efficient.

Heat transport through the membrane (Q_m) can be represented as the combination of latent heat of vaporization (Q_v) and the conductive heat transfer (Q_c) across both the membrane matrix respectively.

$$Q_m = J\Delta H_v + \left(\frac{k_m}{\sigma}\right)(T_{fm} - T_{pm}) \tag{2-3}$$

Where k_m is the thermal conductivity of the membrane, σ is membrane thickness, J is membrane permeate flux and ΔH_v is the latent heat of vaporization

Heat transport through the permeate side can be written as

$$Q_p = h_p(T_{pm} - T_{pb}) \tag{2-4}$$

Where h_p is the permeate side heat transfer coefficient T_{pm}, T_{pb} are interface and bulk temperature at the permeate side respectively.

Various models have been proposed for estimation of k_m. Two of the preferred ones are given below in equations (2-5) and (2-6) respectively.

$$k_m = \epsilon k_g + (1 - \epsilon)k_s \tag{2-5}$$

$$k_m = \left(\frac{\epsilon}{k_g} + \frac{(1 - \epsilon)}{k_s}\right)^{-1} \tag{2-6}$$

Where k_g is thermal conductivity of the vapor filled in the pores, k_s is thermal conductivity of the membrane matrix.

The heat transfer coefficients can be estimated through Dittus Boelter equation

$$\frac{hd_h}{k} = a * Re^b * Sc^c \tag{2-7}$$

Where h is the heat transfer coefficient, d_h is the hydraulic diameter, k is the thermal conductivity, Re is the Reynolds number, and Sc is the Schmidt number. The empirical coefficients a, b, and c depend on the flow regime and specific experimental conditions and are typically determined through calibration or literature correlations.

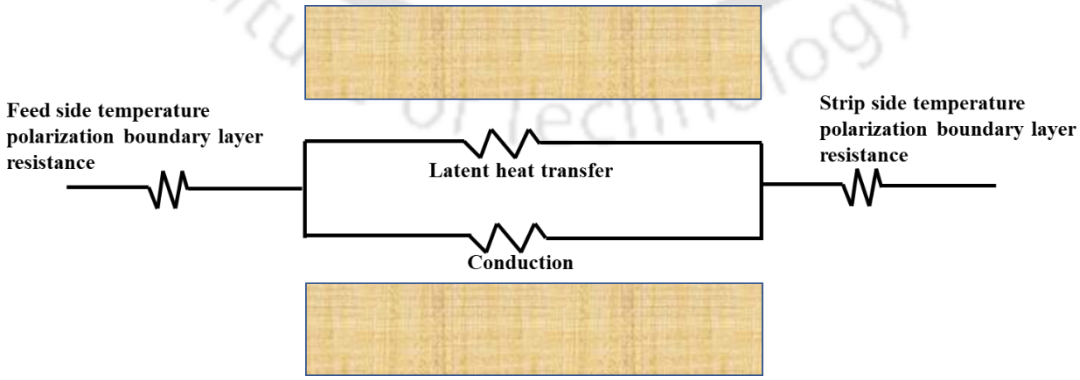

Figure 3: Heat transfer resistance in MD

In MD, heat transfer involves a combination of convective and conductive mechanisms, each dominating at distinct regions within the system. Initially, heat moves from the bulk feed solution to the membrane interface predominantly through convection. From the membrane interface to the permeate side, heat transfer occurs primarily by conduction across the solid membrane and through the latent heat of vaporization, the latter directly associated with vapor transport.

The specific transport mechanisms, however, depend significantly on the downstream conditions and the type of MD configuration utilized. Various literature extensively studied in modelling heat transport through the discussed model equations through lumped and 1-D modelling[92–95]. For instance, in DCMD, the presence of boundary layers on both sides of the membrane introduces notable convection effects. These boundary layers significantly impact the overall heat transfer resistance, making convection critical to the overall heat transport analysis in DCMD[96].

VMD configuration, operates under conditions of significantly reduced pressure on the permeate side. This substantial reduction in pressure diminishes the role of conduction due to the reduced gas-phase density and negligible heat loss through conduction[56,59,77]. Hence, the conductive contribution across the membrane in VMD systems is typically minimal. Instead, heat transport predominantly occurs through convective vapor transport, accompanied by the latent heat associated with vaporization. Overall, understanding these distinctions and clearly identifying regions of dominance for conduction and convection, along with the latent heat effects associated with vapor transport, are crucial for accurate modelling and optimization of heat transport in MD processes.

2.5.1.1 Temperature polarization

In MD, heat transfer across the boundary layers often constitutes the rate-limiting step for mass transfer, as a substantial amount of thermal energy must be delivered to the membrane surface to sustain vaporization. It refers to the temperature difference between the bulk feed temperature and the membrane surface temperature on the feed side. Due to the heat consumed for vaporization at the membrane interface and the thermal resistance across the boundary layer, the membrane surface temperature is lower than the bulk feed temperature as shown in Figure 4. A widely used parameter to quantify the relative contribution of boundary layer resistance to the overall heat transfer resistance is Temperature Polarization Co-efficient

(TPC). A TPC value close to 1 indicates minimal polarization and efficient heat transfer, while values significantly lower than 1 suggest strong polarization and reduced performance[53].

$$TPC = \frac{T_{fm} - T_{pm}}{T_f - T_p} \quad (2\text{-}8)$$

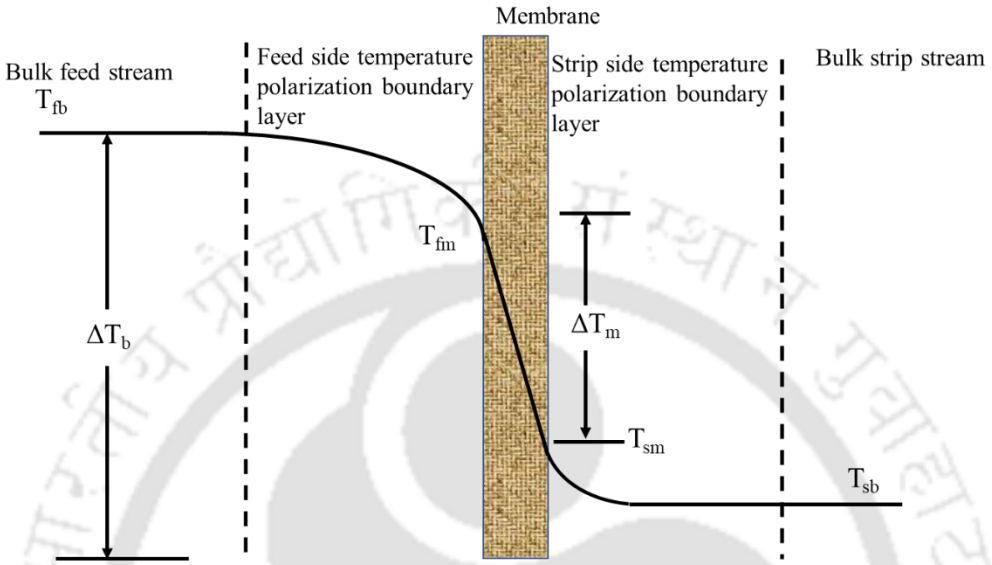

Figure 4 Temperature polarization phenomena in MD

2.5.2 Mass Transfer in Membrane Distillation

MD is primarily driven by a vapor pressure gradient established between the two sides of the hydrophobic membrane. The overall mass transfer involves three sequential steps

1. Evaporation of water molecules at the liquid–vapor interface on the membrane surface at the feed side, where thermal energy provides the latent heat required for phase change.

2. Transport of water vapor through the membrane pores, governed by mechanisms such as Knudsen diffusion, molecular diffusion, or a combination of both, depending on pore size and operating conditions.

3. Condensation of the transported water vapor at the vapor–liquid interface on the permeate side, either within a condensing fluid or on a cooled surface, completing the separation process.

The mass flux in MD can be expressed using a form of Darcy's law, which relates vapor flux to the vapor pressure difference across the membrane.

$$J = K\Delta P \tag{2-9}$$

The overall mass transfer resistance K is sum of the three-individual resistance is determined by the combined resistances of three regions in series: the feed boundary layer, the membrane, and the permeate boundary layer as shown in Figure 5. This relationship is given by:

$$\frac{1}{K} = \frac{1}{\mathrm{K_f}} + \frac{1}{\mathrm{K_m}} + \frac{1}{\mathrm{K_p}} \tag{2-10}$$

Where k_f, k_m and k_p are the mass transfer coefficients of feed layer, membrane and permeate layer respectively.

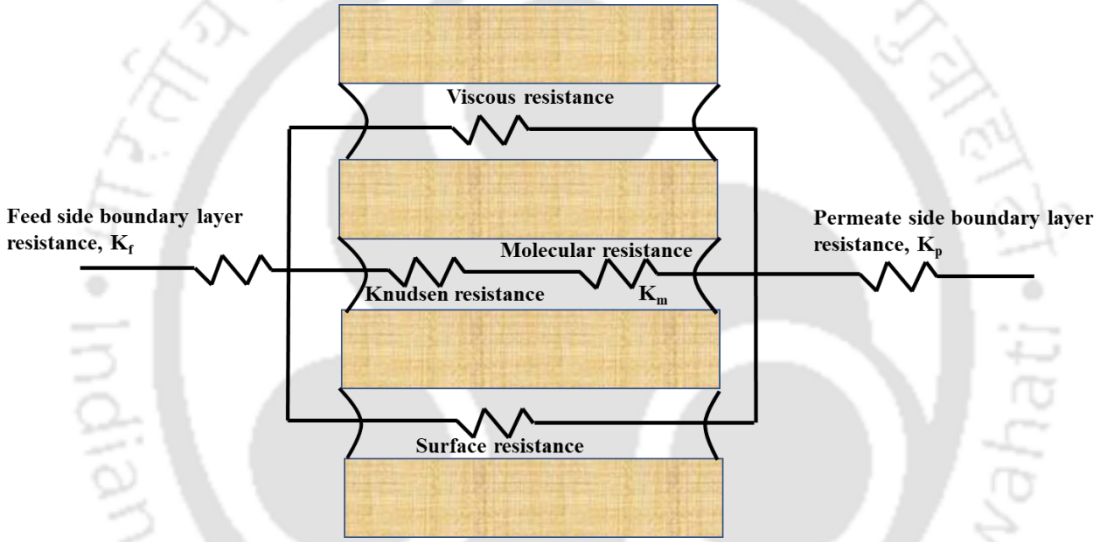

Figure 5: Mass transfer resistance

The coefficient K depends on several factors, including temperature, pressure, membrane composition, and structural properties. Notably, the vapor pressure difference ΔP is not based on bulk fluid conditions but is instead determined by the temperatures and concentrations at the membrane interfaces. To accurately predict flux, a simultaneous solution of heat and mass transfer equations is required, typically using numerical methods and iterative computation. Under steady-state conditions, the vapor pressure on each side of the membrane corresponds to the saturation pressure of water at the membrane surface temperature. This saturation pressure can be estimated using the Antoine equation

$$\mathrm{P_{fm}^{o}} = \mathrm{e}^{\mathrm{A}-\frac{\mathrm{B}}{\mathrm{T_{fm}}-\mathrm{C}}} \tag{2-11}$$

Where A, B and C are Antoine equation constant.

Three different mechanisms have been invoked to explain the transport of water vapour through the pores of membrane. These are described as molecular diffusion, Knudsen diffusion and Poiseuille (convective) flow. This type of mechanism in operation is dictated by the pore diameter and air pressure within the pores as shown in Figure 6.

2.5.2.1 Molecular Diffusion

Molecular diffusion mass transfer mechanism occurs in MD when the membrane pores retain a stationary film of air and are sufficiently large such that intermolecular collisions between water vapor and air molecules occur more frequently than collisions with the pore walls. In this regime, the primary resistance to mass transfer arises from momentum exchange between dissimilar molecules (i.e., water vapor and air), rather than wall interactions. The membrane mass transfer coefficient under molecular diffusion-limited conditions can be estimated using established diffusion equations that account for binary gas interactions within the membrane pores. The membrane mass transfer coefficient applicable to molecular diffusion can be estimated as follows.

$$k_m = \left(\frac{P_{av}}{P_{a(lm)}}\right)\frac{\in}{\sigma\gamma}\frac{(D_w M_w)}{(RT_{av})} \tag{2-12}$$

Where P_{av} is the average gas pressure in the pores, $P_{a(lm)}$ is the log mean air pressure in the pores, $\in$ is the membrane porosity, σ is the membrane thickness, T_{av} is the average temperature in the pores, D_w is the diffusion coefficient of water vapor in air, R is the universal gas constant.

2.5.2.2 Knudsen diffusion

Knudsen diffusion occurs when the pores are sufficiently small for the frequency of collisions between water molecules and the pore walls to be substantially grater than that between water and air molecules. The membrane mass transfer coefficient under Knudsen diffusion conditions can be modelled by

$$k_m = \left(\frac{M_w}{RT}\right)\left(\frac{2 \in r}{3\sigma\tau}\right)\left(\frac{8RT}{\pi M}\right)^{0.5} \tag{2-13}$$

Where r is the pore radius

Although the overall selectivity in MD is predominantly governed by vapor–liquid equilibrium at the membrane interface and the mass transfer resistances in the boundary layers, the membrane itself contributes to selectivity in Knudsen-limited transport conditions**.**

2.5.2.3 Poiseuille flow

Poiseuille flow describes the convective transport of water vapor through fully deaerated membrane pores, driven by a vapor pressure gradient induced by temperature differences or vacuum on the permeate side. This transport mechanism is relevant in configurations such as deaerated DCMD and VMD, where non-condensable gases are absent or minimal within the pores.

$$k_m = \left(\frac{r^2 \in}{8\delta\tau}\right)\frac{M_w P_{av}}{\eta R T_{av}} \tag{2-14}$$

Where η is the viscosity of water vapor at the temperature of operation. This equation shows that the membrane mass transfer coefficient decreases with increasing temperature. Here, mass transfer resistance is due to momentum transfer to the pore walls through viscous drag.

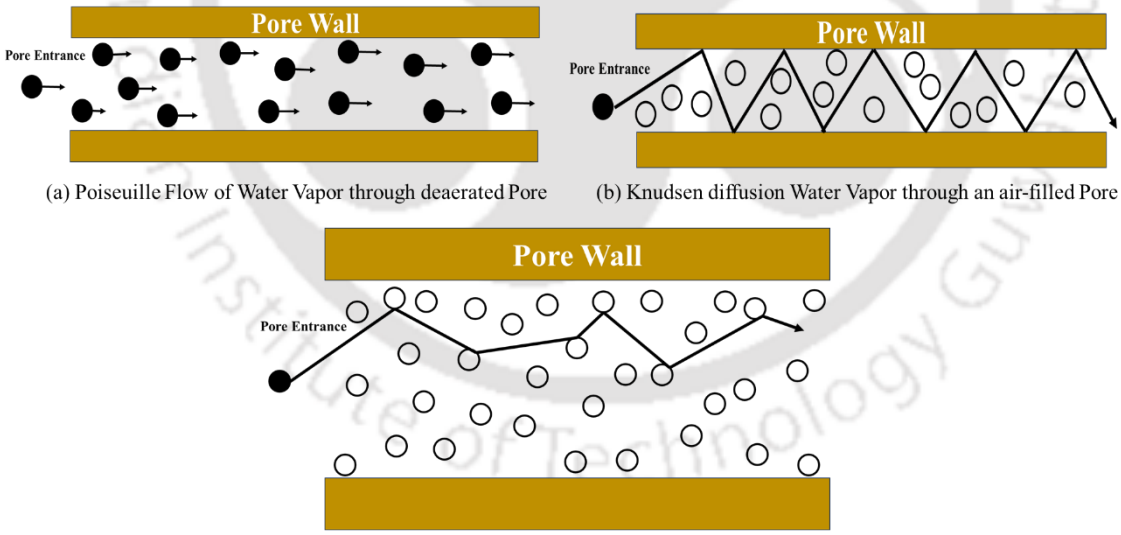

(a) Poiseuille Flow of Water Vapor through deaerated Pore

(b) Knudsen diffusion Water Vapor through an air-filled Pore

(c) Molecular diffusion Water Vapor through an air-filled Pore

Figure 6 Diffusion phenomena in MD

2.5.3 Concentration polarization

CP is a phenomenon inherent to all membrane separation processes. In MD, CP refers to the accumulation of solutes near the membrane surface on the feed side, caused by the continuous evaporation of water and its subsequent transport through the membrane pores. This localized increase in solute concentration at the feed–membrane interface creates a concentration gradient relative to the bulk feed solution, forming a boundary layer that imposes additional resistance to mass transfer as shown in Figure 7. CP is considered an equilibrium-driven process: under steady operating conditions, the rate at which solutes accumulate at the membrane surface becomes equal to the rate at which they diffuse back into the bulk solution. This dynamic balance results in a stable polarization layer, which hinders water vapor transport due to the relatively slow diffusion of solutes.

In DCMD, CP is primarily a feed-side phenomenon, as the permeate condenses directly into a pure water stream, eliminating concentration build-up on the permeate side. In VMD, CP on the permeate side is also negligible due to the low-pressure conditions that limit solute accumulation in the vapor phase. Mathematically, CP in MD is typically modelled using film theory, which assumes the presence of a stagnant boundary layer where solute transport occurs primarily by diffusion. This model provides a framework to estimate the extent of CP and its impact on flux performance

$$C_{fm} = C_{fb} \cdot e^{\frac{N}{K_f}} \tag{2-15}$$

$$CPC = \frac{C_{fm}}{C_{fb}} \tag{2-16}$$

where N is the mass flux of vapor and K_f is the mass transfer coefficient in the feed boundary layer, C_f is the bulk feed concentration, and C_{fm} is the solute concentration at the membrane surface. K_f can be evaluated using equation below for mass transfer coefficient correlation.

2.5.3.1 Determination of mass transfer mechanism

The governing mass transport phenomena widely reported in the literature are based on Knudsen flow or a combination of Knudsen and Poiseuille flow, as determined by the correlation and Knudsen number (Kn) values presented in Table 7

$$kn = \frac{\lambda}{d_p} \tag{2-17}$$

wherein λ is the mean free path of water vapor and d_p is the membrane pore size.

The value of λ is calculated as per the below equation

$$\lambda = \frac{3\mu_v}{P}\sqrt{\frac{\pi R T_m}{8 M_w}} \tag{2-18}$$

The mean free path (λ) for temperatures typically ranging between 40°C and 80°C was determined to lie within the bounds of approximately 0.084 to 0.11 μm[61,66]. Using these values in the governing mass transfer equation, the dominance of Poiseuille flow versus Knudsen diffusion was analysed. Due to the very small pore size in MD membranes, interactions between molecules are negligible compared to the interactions between molecules and the pore wall. Therefore, molecular diffusion can generally be neglected, leaving Knudsen diffusion and Poiseuille flow as the primary mechanisms of mass transfer in the MD system.

Table 7 Mass transport mechanism inside the membrane pore[61]

Total Pressure Difference	**k_n<0.01**	**0.01<k_n<1**	**k_n>1**
ΔP≠0	Poiseuille flow	Poiseuille flow–Knudsen diffusion transition mechanism	Knudsen diffusion

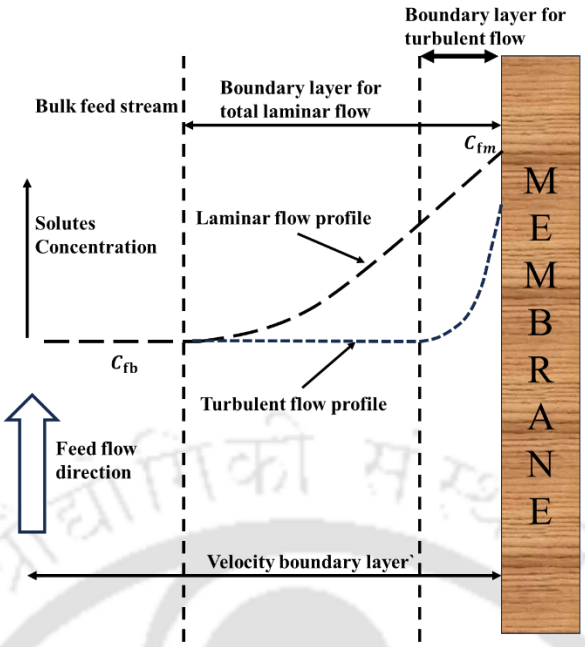

Figure 7: Concentration polarization in MD

2.6 Optimization of operating parameters and MD configurations

Numerous literatures have addressed on optimizing the MD process through operating variables as shown in Table 8 to enhance its overall performance. The secondary decision variables for optimization such as module design aspects, including module length, channel geometry, and structural configuration. Key performance indicators commonly used to characterize the MD process include permeate flux, retention rate and energy consumption. Among these, energy and flux metrics are particularly significant, as they reflect the influence of both operational and capital expenditures of the entire system.

Table 8: Influence of MD performance in various operating parameters

Parameters	Effects
Feed Temperature	Temperature is an exponential function of vapor pressure, as the feed temperature increases rapid increase in flux is expected[97,98]. For every 10^{o}C increase, two-fold increase in the flux reported. Subsequently with increase in permeate flux, membrane fouling accelerates and also certain membrane properties has inherent thermal limitations which limits the operation beyond certain temperature. Therefore, optimizing the feed temperature is critical in MD.
pH	MD is less sensitive to changes in the feed pH
Feed velocity	Feed velocity plays a crucial role in modulating the hydrodynamic conditions within the membrane module, particularly by influencing the thickness of the boundary layer adjacent to the membrane surface. As the feed velocity increases, the dominance of boundary layer across the membrane surface decreases which increases the permeate flux[99]. It also contributes in increasing heat transfer coefficient leading to reduction in temperature and concentration polarization effects. Though higher feed velocity enhances mass transfer, it also increases the risk of membrane wetting. Therefore, the flow rate should remain within the module's maximum capacity to ensure effective and stable separation.
Feed concentration	Increase in feed concentration, contributes in increase in boiling point of the feed solution, which significantly affects the vapor pressure gradient and membrane performance in permeate flux. More often contributes to concentration polarization hindering mass transfer[100].
Long term operation	The surface morphology of MD membranes exhibited significant alterations, leading to a reduction in both membrane hydrophobicity and surface roughness. These changes can impact membrane performance and long-term stability. Therefore, specific cleaning techniques has to be incorporated after certain cycle of operation[101].

J. Bose et al. [98] investigated direct contact membrane distillation (DCMD) for brackish water desalination using polyvinylidene fluoride (PVDF) membranes, focusing on the optimization of process variables through advanced modelling techniques such as Artificial Neural Networks (ANN) and Response Surface Methodology (RSM). Among these, ANN demonstrated superior predictive accuracy for both permeate flux and salt rejection compared to RSM. Furthermore, optimization using a Multi-Objective Genetic Algorithm (MOGA) yielded a pareto-optimal set of solutions, achieving a maximum permeate flux of 21.4 LMH at a feed flow rate of 44.75 LPH, and an alternative configuration attaining 100% salt rejection at 52.48 LPH. This study provides valuable insights into the scalable application of DCMD systems for efficient brackish water desalination.

Ali et al [102]evaluated multistage DCMD using a commercial hollow-fiber membrane to achieve high recovery with low-grade heat. The study identified module length as a critical design variable and optimized it with respect to feed-to-permeate flow ratio, feed temperature, and feed concentration. Results showed that thinner membranes significantly reduce the optimum length at 8% feed concentration, decreasing thickness from 450 μm to 20 μm reduced optimum length from 9.12 m to 0.48 m**,** but with a corresponding SEC penalty, increasing from 912 to 1240 kW/m³ due to lower heat-recovery. Practical operation was observed when optimum length remained < 6 m at F/P ratios above 4. The study highlights the importance of balancing membrane thickness and module length to ensure energy-efficient DCMD performance..

In a comparative study on membrane performance, J. Xu et al.[103] evaluated ten commercially available membranes composed of PTFE, PP, and PVDF using an AGMD system. The investigation considered both operational variables such as feed temperature, feed velocity, and salt concentration and membrane-specific characteristics including material, thickness, pore size, and support layers. Among the membranes tested, PP exhibited superior flux performance compared to PVDF and PTFE. Optimal performance was observed for membranes with pore sizes in the range of 0.2–0.45 μm; smaller pores resulted in reduced flux, while larger pores increased the likelihood of pore wetting due to lower Liquid Entry Pressure (LEP). Permeate flux decreased with increase in salt concentrations, especially at 80 g/L, as vapor pressure declines. The presence of a support layer slightly reduced flux by approximately 2.35%. Additionally, increasing feed velocity in the laminar regime enhanced permeate flux, though the effect was limited at lower feed temperatures. These insights widen the

understanding of membrane performance under varying operating conditions and membrane properties.

Ruiz-Aguirre et al[104] conducted a pilot-scale comparison of two Aquastill AGMD spiral-wound modules (7.2 m^2, 1.5 m length and 24 m^2, 5 m length) for seawater desalination. The shorter module achieved higher permeate flux (4.20 LMH) but lower energy efficiency (STEC 295.6 kWh/m^3), whereas the longer module delivered improved heat recovery with lower flux (1.35 LMH) and significantly better STEC (106.6 kWh/m^3). Evaporator inlet temperature was the dominant factor affecting both flux and STEC, while feed flow rate showed mixed influence. An optimal channel length of 3.72 m was identified, yielding 2.44 LMH flux and 141.5 kWh/m^3 STEC, confirming a clear trade-off between productivity and energy efficiency in AGMD design.

In an effort to optimize the energy efficiency of the DCMD system, Duong et al.[105] implemented a strategy of recycling the brine back into the system to improve seawater desalination efficiency. This approach resulted in a 50% reduction in STEC and enhanced water recovery up to 60%. However, severe membrane scaling was observed at a recovery rate of 80%, leading to the conclusion that the optimal recovery is around 70%, where continuous operation could be maintained without any scaling. Additionally, increasing the feed temperature and recirculation rates further improved thermal efficiency and allowed for effective operation with higher feed salinity while maintaining good recovery.

R. Ullah et al. [106] investigated the DCMD system with a focus on improving its energy efficiency. The study addressed key limitations hindering the scalability of the technology, such as the lack of standardized units and definitions for energy efficiency. It emphasized the importance of integrating DCMD with solar energy and waste heat recovery to enhance energy efficiency, as well as incorporating heat exchangers to recover latent heat within the system. Additionally, the research highlighted the need for optimized module designs to reduce temperature and concentration polarization effects. Standardizing membrane properties, including thickness, water contact angle, pore diameter, porosity, and membrane structure (e.g., hollow fibre, flat sheet), are essential for the successful upscaling of this technology.

2.7 Process integration of MD with energy recovery unit

A major limitation associated with MD is the challenge of improving energy efficiency, especially due to the high energy demand for preheating the feed in all configurations, as well

as the external condensation of vapor in the case of VMD and SGMD. Among the energy-demand, feed heating represents a significant portion of the overall energy consumption. The integration of waste heat and renewable energy has been extensively reported in the literature, highlighting its importance in minimizing power consumption However, MD generates saturated vapor that can be effectively utilized for preheating the feed solution, thus promotes to minimize STEC. Several studies have explored methods to maximize the utilization of valuable latent heat to enhance energy efficiency.

Numerous studies have focused on improving STEC through various strategies, such as feed recirculation, optimization of process variables, module design modifications, membrane physical properties and optimization of membrane length. These steps have significantly added value to the improvement of energy efficiency in the MD. Additionally, MVR has been employed to increase the pressure and temperature of the latent heat, thereby enhancing the release of enthalpy to the incoming feed. The results from MVR integration have been promising in terms of energy recovery and process efficiency[107].

Another emerging area of interest is the integration of MD with HP system, which can simultaneously condense the vapor and heat the feed solution by circulating refrigerants[108]. This integration holds potential for significant energy savings. Exergy analysis has also been extensively conducted to evaluate the maximum utilization of latent heat within MD processes[109]. This analysis helps to identify inefficiencies and optimize energy recovery strategies.

The integration of MD with TEHP has been studied for small-scale systems. This integration effectively utilizes both the hot and cold sides of the system, significantly reducing the energy requirements for both heating and cooling. As a result, the overall performance of the system is enhanced, making it a promising solution for more energy-efficient MD processes.

2.7.1 Thermo Electric Heat Pump

A TEHP is a device that utilizes the Peltier effect to transfer heat between two materials, enabling both heating and cooling functions. It works by passing an electric current through a junction of two different semiconductors, creating a temperature difference that can absorb or dissipate heat as shown in Figure *8*. The direction of heat flow can be reversed by changing the polarity of the electric current, allowing the device to function as both a cooler and a heater.

TEHPs are particularly valued for their modularity and scalability, that they can be easily adapted to different sizes and applications. The most promising applications of TEHPs is in applying simultaneous evaporation and condensation processes, which is highly beneficial in energy-intensive applications like seawater desalination and dehumidification[85,110,111].

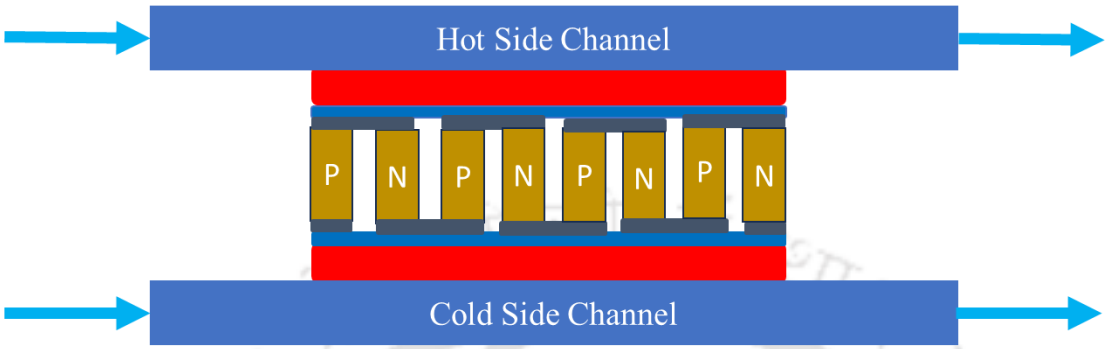

Figure 8: TEHP device for heating and cooling applications

In MD to tackle the energy limitation on cooling and heating demand, an extensive theoretical and experimental studies have been reported. For instance, a comparative study by Daniel et al.[112] , MD technology consumes 120-170 kWh of thermal energy and 0.6-1.8 kWh of electric energy to produce one m^3 of distilled water from seawater, while the RO system consumes only 2.5-7.0 kWh electric power. This study highlights the impact of energy efficiency of the stand-alone MD system. Enhancing the energy efficiency of MD through heat recovery or more energy efficient design could substantially reduce the operational costs, making MD a more economical and widespread its application.

Recently few studies to improve the heat transfer efficiency between hot and cold stream have integrated TEHPs with MD configurations like DCMD. Study reveals that integrating TEHP device can significantly decrease the specific energy consumption (SEC) of the entire process. Among the studied parameters like current, feed flowrate, permeate flowrate, membrane thickness, hot fluid recirculation, thermoelectric cooler plate type and size involving in the operations, current and feed flowrate found to be critical factors. Keeping all the parameters at optimal level and optimizing the feed flowrate can drastically reduce the SEC by 34% in the operation. Recycling the hot fluid tremendously contributed in decreasing the thermal energy requirement in the process.

D. Afaneh et al.[87] proposed and evaluated a hybrid system combining a TEHP with DCMD. Numerical simulations of four different configurations under varying operating parameters

(feed flow rate, electric current, temperature, TEHP size, and water production). Among the four configurations, the version with recycling of permeate-side water energy showed the best performance. Under a low electric current of 2.1 A and feed flow of 4 L/min, they reported a SEC reduced to 217 kWh/m³.The integration shows significantly improved energy recovery and water production potential, using the TEHP for both heating and cooling.

O. Makanjuola et al[86] conducted an experimental study on a thermoelectric-driven membrane distillation system (TE-MD) using an experimental-design approach and systematically varied operating parameters to evaluate performance under different conditions. Provided empirical data on permeate flux and system behaviour under different parameter sets, showing the feasibility of TE-MD as a desalination route. The study validates that TE-driven MD can function and produce permeate under controlled lab conditions. However, energy efficiency, long-term performance, and practical scalability remains as challenge.

The integration of AGMD with TEHP has been explored to enhance energy efficiency. In addition to this integration, various surface modifications, including hydrophobic and hydrophilic coatings on the condensing surface, as well as the adjustment of the condenser's inclination angle, have also been investigated. However, during process integration, experimental limitations were observed, particularly with higher operating voltages around 10-12V, which led to instability in the system. The developed process addresses this issue by operating at lower voltages, ensuring greater stability. This system is capable of managing both the hot and cold sides, effectively handling both heating and cooling applications. Moreover, this approach reduces the resistance created by the gap between the condensing plate and vapor, further improving the process efficiency[113].

Al-Madhhachi et al[114] proposed a novel design for a TEHP module that facilitates simultaneous water evaporation on the hot side and condensation on the cold side. The developed system achieved a water production rate of 28.5 mL/h with a specific energy consumption (SEC) of 0.0014 kWh/mL, using a feed tank with a volume of 3000 mm³ of water. The results concluded that maintaining a maximum temperature difference between the hot and cold sides of the TEHP significantly improves performance, with a temperature increase of 26.4°C on the hot side and a decrease of 8.4°C on the cold side. This system demonstrated the lowest SEC reported in the literature, and its energy efficiency could be further enhanced by integrating it with solar energy.

2.7.2 Heat Exchanger

MD faces two critical challenges that limit its commercial viability: low permeate flux and high STEC. To address these issues, extensive research efforts have focused on enhancing system performance by maximizing flux and reducing energy demands. A key strategy is the integration of HX for improving the latent heat recovery during vapor condensation. Two primary integration strategies are commonly employed: Using HXs to harness external waste heat or renewable energy sources (e.g., solar or geothermal) for preheating the feed solution before it enters the MD module, and capturing the latent heat released during vapor condensation in the permeate stream and releasing the heat to the incoming fresh feed or reject brine. This internal heat recovery loop is particularly effective in configurations like AGMD, where the design facilitates efficient condensation and minimizes conductive heat losses.

G. Guan, et al[27] studied theoretically the energy efficiency of DCMD by integrating with HX for latent heat recovery. An implicit expression for the GOR was developed to link system performance with module-level parameters, avoiding complex full-system simulations. Results showed that low and equal recirculating flowrates on both feed and permeate sides are essential for achieving high GOR values, a maximum of 6 was observed at low flowrates and although this reduces water productivity. Simulation results demonstrated that the degree of heat recovery measured by the temperature difference between the outlet of the permeate stream and the inlet of the feed stream in the heat exchanger strongly influenced GOR. A larger temperature difference indicated less effective heat recovery and led to a decline in GOR by up to 30%. Membranes with higher thermal resistance improved heat recovery, but a trade-off was observed between GOR and permeate flux higher water production led to lower energy efficiency.

R. Gonzalez-Bravo et al.[115] investigated the optimal integration of TMD that are thermally coupled with processing facilities, focusing on the role of heat exchanger networks (HENs) for energy recovery. This superstructure-based optimization model simultaneously designs the TMD unit and its thermal integration with the host process plant. The model aimed to maximize net annual profit by balancing capital and operational costs. A key component of the integration was the strategic placement of HX to recover waste heat from industrial streams and preheat the TMD feedwater, thereby minimizing external heating utility requirements. This integration led to a 31% reduction in cooling utility demand and a 50% increase in profit compared to non-

integrated setups and also it eliminated the need for extra heating by recovering 131 MW of thermal energy.

Q. Li et al.[116] developed an innovative solar power integrated system for generating water and thermal energy for both potable water and domestic hot water for commercial buildings. experimental findings demonstrated that a permeate flux of 4 to 10 LMH can be achieved when the feed temperature is maintained between 50 and 70 °C, effectively reducing the salinity from a seawater-level concentration of 35,000 ppm to a low range of 10–200 ppm. A system configuration combining a solar absorber area of 1.6 m^2 with approximately 0.2 m^2 of membrane surface was shown to produce around 4 L of potable water and recover about 4.5 kWh of thermal energy at 45 °C per day, under an average solar irradiance of 4 $kWh/m^2/day$.

Bamufleh et al.[117] developed an optimization framework for a MED–MD hybrid system utilizing industrial excess heat to improve energy efficiency and lower desalination cost. In this configuration, MD further recovers distillate from MED brine while heat exchangers recycle thermal energy for feed preheating and sustaining both units. A superstructure-based Mixed Integer Non-Linear Programming (MINLP) optimization identified the optimal number of MED effects, MD membrane area, and heat-exchanger duties to minimize annualized cost. Case studies demonstrated that combining internal heat recovery with external process heat can reduce the water cost to $\$0.61/m^3$**,** highlighting the techno-economic potential of integrated MED–MD systems.

A Najib et al.[118] experimentally evaluated a DCMD system under two cooling strategies: single-stage cooling (SSC) and double-stage cooling (DSC). At high hot-side flow rates (> 300 L/h), SSC could not maintain the required cold-side temperature, leading to reduced flux and rising cold-tank temperature. The DSC configuration, achieved by adding an additional immersed heat exchanger, successfully extended the operating range by sustaining lower inlet cold temperatures. As a result, DSC delivered higher permeate flux, recovery ratio, GOR, and energy efficiency while reducing STEC. However, exergetic efficiency gains were limited at high flow rates due to increased unused thermal energy and exergy destruction in the central cooling unit.

Liu et al.[119] studied a novel “in-situ latent heat recovery” strategy in VMD by designing a jacketed-VMD module that integrates HF membranes with thin-walled heat exchange tubes. This configuration enables direct and localized heat transfer between the condensation and

evaporation processes, significantly reducing the distance over which heat must travel and eliminating delays associated with external heat recovery setups. Compared to conventional and externally recovered VMD systems, this internal heat exchange approach improved both water production and energy efficiency. The jacketed-VMD achieved up to 47.4% increase in permeate flux**,** 173.1% GOR, and reduced STEC by 63.4% and cooling water demand by 41.2%**.**

Swaminathan et al. [120] developed a simplified heat-exchanger-based modeling framework for MD, enabling rapid comparison of AGMD, PGMD, CGMD, and DCMD using module effectiveness (ε) and thermal efficiency (η). The ε–NTU-based model predicted MD performance with < 11% deviation and showed that energy recovery (ε) has a stronger influence on GOR than conduction losses (η). CGMD demonstrated the highest efficiency, achieving nearly twice the GOR of PGMD due to enhanced internal heat recovery, while DCMD could match CGMD performance only with significantly larger external HX area. AGMD benefits from reduced heat losses but limited heat recovery, resulting in lower GOR

2.7.3 Mechanical Vapor Compressor

MVR is employed in MD to increase the temperature and pressure of the vapor produced in the system. This pressurized vapor is then condensed, allowing its latent heat to be effectively transferred back into the system. Specifically, the recovered heat is reused to preheat both the incoming feed stream and the reject stream, significantly reducing external energy demands. Z. Si et al. [121] investigated a hybrid desalination system combining VMD with MVR to enhance latent heat recovery and reduce energy consumption. The system achieves a STEC of 85 kWh/m³, which is 39.3% lower than that of a solar-powered MD system under similar membrane and operating conditions. Key findings reveal that the proposed system effectively mitigates thermal and concentration losses through parameter tuning, which reduces compressor power demand. Simulations show that by minimizing the influence of TPC, CPC, and BPE, compressor power can be significantly reduced. For instance, increasing feed velocity and permeate-side pressure lowers polarization effects and heat loss, thereby improving system efficiency.

The study by Swaminathan et al. [122] evaluated a hybrid MVC–MD system in which the conventional brine-to-feed heat exchanger is replaced by an MD module, enabling reuse of brine thermal energy for feed preheating while simultaneously generating additional freshwater. Three MD configurations (AGMD, PGMD, and CGMD) were studied, with

CGMD showing the best heat-transfer performance and economic benefit due to enhanced thermal conductivity and reduced area requirement. Under optimal operation at a 70 °C top brine temperature and 50% MVC recovery, the MVC–CGMD hybrid reduced the water production cost by up to 6%. This integration provides a cost-effective pathway to improve MVC performance by converting reject heat into productive desalination work.

Z. Si et al.[123] The study investigated a VMD system integrated with mechanical vapor recompression (MVR) for sulfuric-acid waste treatment and resource recovery. Thermodynamic models based on the first and second laws were developed and validated against experimental data to analyze the effects of feed concentration, temperature, velocity, and permeate pressure on heat and mass transfer. Results showed that increasing feed temperature and velocity enhances convective and mass-transfer coefficients, whereas higher feed concentration reduces heat transfer but improves solute driving force due to elevated acid activity. Increasing membrane area from 10 to 200 m^2 initially lowered compressor power and increased exergy efficiency, but excessive area resulted in higher pumping power and reduced flux. An optimal area of 60 m^2 minimized total power consumption to 10.04 kW and maximized exergy efficiency at 19.06%**,** demonstrating the importance of properly balancing system size and energy use in VMD–MVR integration.

Z. Si et al.[124] analysed the contribution of MVR with Multiple Vacuum Membrane Distillation modules (MVMD) to strategically explore the energy reduction for industrial water treatment. Water production performance was found to be highly dependent on feed temperature, followed by permeate side pressure, feed flow rate, and feed concentration as determined by an orthogonal multi-factor experiment. Experimental results showed that under the feed concentration 5%, flow rate 25 m^3/h, membrane area 200 m^2 the MVR-MVMD system achieved a STEC of 81.95 kWh per ton, representing a 79.24% energy saving compared to a conventional MVMD system. This approach not only makes the process more energy-efficient but also supports sustainable and cost-effective industrial wastewater treatment by leveraging advanced heat recovery and membrane separation technologies.

In addition, to that Z. Si et al.[125] also investigated the integration of MVR with HF-VMD to treat high-salinity industrial wastewater, aiming for ZLD and resource recovery. Experiments demonstrated excellent airtightness, ensuring reliable operation and preventing leaks that could affect performance. The system achieved a high separation efficiency of 99.9% and significantly lower evaporation energy consumption compared to conventional methods. By

recovering and reusing the latent heat from the secondary vapor through the MVR process, the system's STEC was reduced to a range of 70–150 kWh per ton of treated water and this demonstrates to an energy savings of up to 79% compared to traditional VMD systems, which typically lack effective latent heat recovery.

Z. Si et al.[126] studied hydrophobic PTFE HF membrane for VMD, which provides strong corrosion resistance and high separation efficiency for sulfuric acid wastewater. MVR technology is integrated to recover and reuse the latent heat from secondary vapor, which is compressed and used to preheat the feed, drastically reducing the need for fresh external heating. The proposed VMD-MVR system achieves energy savings of 77.6% compared to conventional VMD and 20.4% compared to multi-effect MD systems, due to the significant thermal efficiency improvements from latent heat recovery.

The study by Ali et al [107] demonstrated a hybrid desalination system combining MVC with DCMD to enhance energy efficiency and water production. In this configuration, the DCMD module replaces the brine preheater in MVC, using the thermal energy from the reject brine to simultaneously preheat the feed and generate additional freshwater. The hybrid system reduces STEC consumption by 25–37% which is down to 9.6–24.3 kWh/m³ and increases freshwater output by 3–10% compared to standalone MVC, depending on brine temperature. However, this improvement comes with a 60% increase in required surface area. Adjusting the permeate-to-feed ratio showed minimal performance gain, while extending MD module length by 50% yielded a 3% rise in water production and 10% drop in compression power. A modified structure leveraging the distillate stream's heat achieved a 5% production increase and 43% reduction in specific compression energy.

2.7.4 Heat Pump

HP acts as versatile integration with MD for better energy efficiency as it recovers latent heat through condensation at the evaporator section and preheats the feed solution at the condenser section simultaneously using the heat transferred from evaporator to condenser, thereby minimizing the external thermal input. Between evaporator and condenser, a compressor unit that elevates the saturated vapor to a superheated state, resulting in an increase in both temperature and pressure of the vapor, which further facilitates efficient heat transfer. A throttle valve is employed for pressure reduction at constant enthalpy, for enhancing the evaporation process as shown in Figure 9. Throughout this closed-loop system, a selected refrigerant

continuously circulates, undergoing phase transitions in response to the thermodynamic conditions imposed by each unit operation, as discussed.

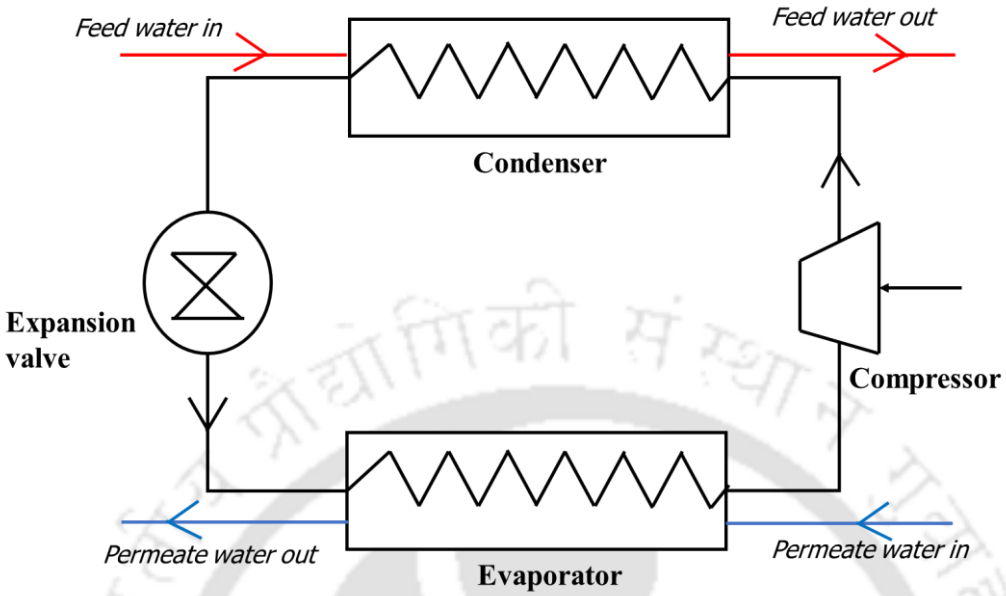

Figure 9: Utilization of HP for heating and cooling application for MD

W. Su et al[82] performed energy modeling and optimization of a hybrid solar with heat-pump and VMD system applied to liquid desiccant regeneration. The result showed significant reduction in thermal energy use when compared to conventional regeneration methods. Identified optimal VMD operating conditions to improve SEC, COP, and water recovery. Demonstrated energy-efficient regeneration using VMD integration. However, system complexity, reliance on solar availability, and economic feasibility under climate variability were not fully addressed.

Q. Ma, et al.[83] proposed a small-scale desalination system integrating VMD with a solar flat-plate collector and a heat pump, enabling latent-heat recovery and feed pre-heating through a closed refrigerant loop. A dynamic model was developed and optimized using a multi-objective evolutionary algorithm to balance water production and electricity consumption. The system achieved stable SEC values of ~52–60 kWh/m³, with freshwater production strongly influenced by membrane surface area, vacuum pressure, and permeability. Sensitivity results showed that improving heat-recovery efficiency reduces dependence on solar input and shifts performance

control toward VMD variables. The study demonstrates feasibility of autonomous desalination for remote sites with modest photovoltaic capacity.

E. Shaulsky et al.[34] evaluated a heat-pump assisted DCMD system as an energy-efficient alternative for thermal desalination, particularly in ZLD applications. By recovering latent heat from the permeate side and reusing it to heat the feed, the heat pump maintains a strong temperature gradient while lowering the overall energy requirement. The system achieved water fluxes > 60 LMH and GOR values up to 60, outperforming conventional DCMD and approaching MVC performance. Increasing the membrane temperature difference enhanced flux but reduced GOR, indicating the need for optimal operating balance. Its modular design, low capital cost, and use of polymeric components make HPMD attractive for compact, distributed desalination..

A. Khalifa et al.[127] performed a theoretical evaluation of DCMD integrated with a heat pump using different refrigerants and cycle configurations. Their results showed that heat pump coupling substantially reduces energy consumption and freshwater production cost compared to standalone DCMD, with optimized closed-loop systems achieving respectable GOR and SEC values alongside lower cost, indicating strong potential for compact, low-cost desalination.

M. Bindels and B. Nelemans et al. [128] investigated three V-AGMD + heat pump configurations aimed at improving energy efficiency and enabling ZLD. The heat pump provided both heating and cooling simultaneously, improving water flux and reducing SEC for concentrated brines to values similar to MVC. The study highlighted the potential of HP-MD systems in advanced desalination and ZLD applications, while noting practical challenges associated with refrigerant pressure and system cost.

L. Wang et al. [129]studied a novel Heating Tower Heat Pump (HTHP) system integrated with AGMD regenerator, designed to enhance energy efficiency and prevent frost formation during low-temperature operation. By utilizing the sensible heat of high-temperature refrigerant gas for solution regeneration, the system achieves significant performance improvements over traditional reverse-defrosting air-source heat pumps. Key results show that the deterioration of coefficient of performance is reduced from 4.4% to 2.6% as the evaporating temperature drops from −15 °C to −25 °C, and the GOR reaches up to 5.6, indicating efficient thermal energy use. Additionally, the system maintains a higher coefficient of separation performance than

conventional up to 0.0052 kg/kJ at −20 °C demonstrating superior water removal efficiency and suitability for cold-climate applications.

Z. Si et al.[130] studied an innovative hybrid VMD-HP system to enhance the energy efficiency of VMD for treating sulfuric acid waste. The system integrates a HP to simultaneously heat the feed solution and cool the permeate-side vapor, thereby reclaiming latent heat. Mathematical models, validated by experiments using a PTFE membrane, demonstrated that the system can operate effectively at low temperatures from 318.15 to 333.15 K. Key findings showed that increasing feed temperature, feed velocity, and permeate pressure or reducing feed concentration significantly improved performance by lowering the STEC and increasing the COP. Under specific conditions of 20% sulfuric acid, 333.15 K feed temperature, 2 t/h flow rate, the VMD-HP system achieved a SHEC of 181.47 kWh/t and a COP of 3.44, with an evaporation cost reduction of 58.74% compared to a conventional VMD setup.

2.8 Strategies to recover molybdenum

2.8.1 Recovery through hydrometallurgy techniques

Numerous studies have investigated molybdenum recovery through hydrometallurgical processes, utilizing both single and multi-stage solvent contact methods. Menglei et al. [131] developed an integrated process comprising acid leaching, solvent extraction, and stripping for the efficient recycling of spent catalysts. The study focused on selectively recovering molybdenum from other co-existing metals and elucidating the extraction mechanisms using various solvents. The extractants evaluated included methyl trioctyl ammonium chloride, tri-n-octylamine, tris(2-ethylhexyl) amine, bis(2-ethylhexyl) phosphate, and tributyl phosphate each representing distinct functional groups. Among these, tri-n-octylamine and methyl trioctyl ammonium chloride demonstrated superior extraction performance, achieving over 98% molybdenum recovery in the organic phase. For the stripping stage, Ammonium hydroxide (NH_4OH), Soidum hydroxide (NaOH), and Sulphuricacid (H_2SO_4) were employed as stripping agents to effectively recover molybdenum from the loaded tri-n-octylamine phase.

Seyed et al. [132] investigated the selective leaching of molybdenum from spent catalysts using a liquid membrane technique. Cyanex 272 and ammonium fluoride (NH_4F) were identified as effective extractant and stripping agent, for the selective extraction of molybdenum. Key operational parameters including surfactant concentration, agitation speed, contact time, treat ratio, and internal-to-membrane phase volume ratio were systematically optimized. As a result,

over 75% of molybdenum was selectively transferred to the internal phase as shown in Figure 10, demonstrating the efficiency of the liquid membrane method for molybdenum recovery.

.

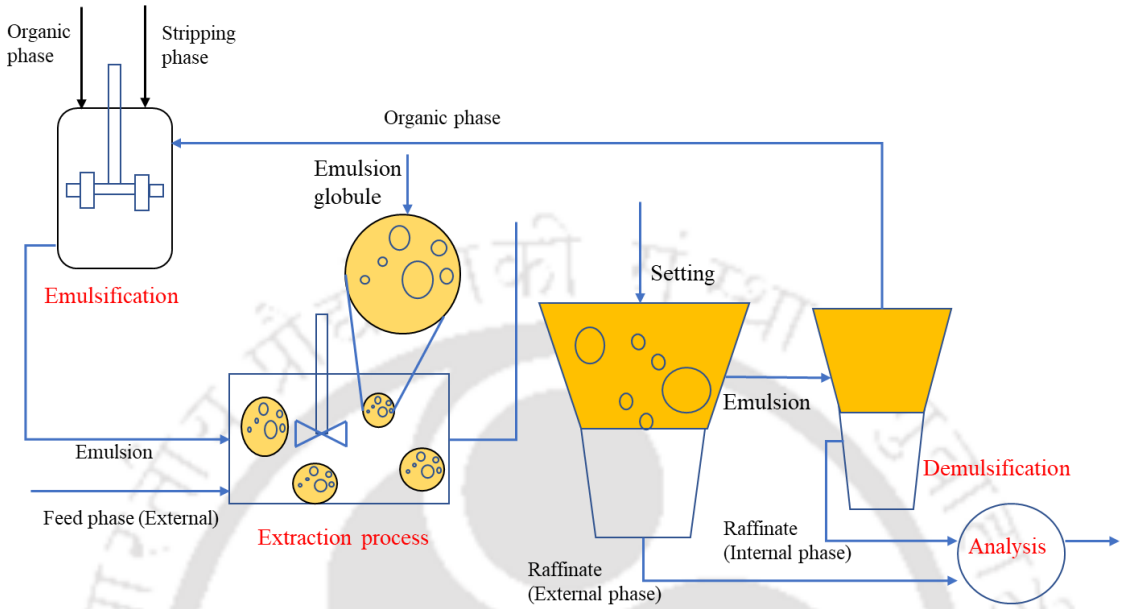

Figure 10: Recovery of molybdenum through emulsification

2.8.2 Recovery through pyrometallurgy techniques

Pyrometallurgy is a high-temperature metallurgical process used to extract and refine metals from their ores or recycled materials. This technique involves the application of heat to bring about chemical and physical transformations that separate metals from impurities. Common pyrometallurgical processes include roasting, smelting, and refining, often conducted at temperatures exceeding 500 °C. It is widely used for the recovery of metals such as copper, nickel, iron, and precious metals, particularly when dealing with sulfide ores or spent industrial catalysts. K.K.Sahu et al. [133] reported that metals such as nickel, vanadium, aluminum, and molybdenum can be effectively separated through an initial roasting step at 550 °C, followed by acid leaching using dilute sulfuric acid. This process enables the dissolution of molybdenum, nickel, and a portion of aluminum. Furthermore, selective leaching of molybdenum and vanadium can be accomplished using an organic solvent, leaving nickel and aluminium in the raffinate phase. To recover molybdenum in its purest form, ammonia is employed as a stripping agent, leading to its precipitation as an ammonium salt via selective precipitation.

Dizhang et al [134] reported the extraction and recovery of nickel, molybdenum, and vanadium from spent hydro processing catalysts using an integrated process involving ammoniacal leaching followed by selective separation. Initially, the spent refinery catalyst was roasted at 400 °C to facilitate metal liberation. In the first leaching step, selective extraction using ammoniacal liquor at pH 9 achieved leaching efficiencies of 88.74% for nickel and 97.92% for molybdenum. In the subsequent step, vanadium was effectively extracted from the leach residue at pH 12, attaining an efficiency of 97.13%. Nickel was further separated using neo-decanoic acid in sulfonated kerosene as the solvent, achieving an extraction efficiency of 96%. Complete stripping of nickel was accomplished using NaOH. Wang et al. [135] developed an integrated process combining blank roasting and alkaline leaching to recover vanadium, molybdenum, and aluminium from spent HDS catalysts. Roasting at 650 °C oxidized MoS_2 and V_2S_3 into leachable MoO_3 and V_2O_5, enabling co-leaching of V up to 97%, Mo 85% and Al 88% using 35 wt% NaOH at 110 °C. At 1000 °C, Al_2O_3 transformed into its stable α-phase, allowing selective leaching of V up to 91% and Mo 96% while Al remained in the residue. The process offers a clean and efficient alternative to traditional solvent extraction, with recyclable leachate and minimized waste.

Neha et al.[136] investigated an integrated bio-pyro-hydrometallurgical approach for recovering nickel and molybdenum from spent petroleum refinery catalysts. The process involves three key steps: (1) bioleaching using a mixed culture of iron and sulphur-oxidizing microorganisms, achieving leaching yields of 94% for Ni and 71% for molybdenum; (2) roasting of the bioleached residue at 700 °C for 1 hour, which reduces SO_2 emissions by 64.95% and liberates an additional 23% of molybdenum from the aluminosilicate matrix; and (3) alkaline leaching using Na_2CO_3–$NaHCO_3$ in a 2:1 ratio, further increasing molybdenum recovery to 92%. The combined method also achieved partial recovery of other critical elements such as rhenium 65%, copper 58%, aluminium 30%, and trace precious metals like palladium.

2.9 Research Gap

MD has the potential to recover higher rejection rate of solute and pure solvent production with minimal fouling and that can also be integrated with waste heat, lower grade energy and renewable energy etc. This technique has shown tremendous performance in concentration of metal ion along with crystallization. However, MD lacks wider commercialization due to its limitations in energy requirement and low productivity. Theoretical model that incorporates all

the fundamental transport equations such as mass, momentum and energy along with conduction loss, concentration and temperature polarization is still lags in the literature. This study will help to optimize the module parameters, module design for membrane module manufacturers. The detailed optimization study on operating variables would significantly contribute in improving the productivity. To provoke the scaling up of this technology, integrating it with heat recovery units such as HX, VC, TEHP and HP or other membrane-based processes needs to be critically analysed. A proper study on energy pinch analysis in an integrated MD system is of high demand. This research work carries a significant effort on optimizing membrane module parameters with theoretical model which is well validated with actual experimental condition. Energy pinch analysis by integrating with energy recovery device such as HX, VC, TEHP and HP. MD application is also extended in this research work by studying an industrial effluent heavy fraction pitch to recover the solute molybdenum. This enables the concept of ZLD in process industries and also address the scope of this technique in application in desalination and solvent recovery.

Chapter 03

Theory

3 Theory

This chapter provides a brief overview of the theory underlying the development of a one-dimensional steady-state mathematical model for the VMD system to evaluate the performance and to identify the optimal operating conditions with module dimensions. Extending further, lumped modeling and integration of energy recovery equipment such as TEHP, HX, VC, and HP were highlighted.

3.1 1-D mathematical model development for VMD performance evaluation

In this study, mathematical model for the steady state one dimensional VMD process was developed by integrating a system of model equations such as:

(i) First principle model equations such as heat, mass and momentum balance to capture the coupled heat and mass transport phenomena and pressure drop across the module.

(ii) Knudsen and Poiseuille diffusion model for vapor transport through the membrane pores, accounting for the transitional flow regime.

(iii) Film theory model to capture the concentration polarization phenomena.

The Process Flow Diagram (PFD) for a HF-VMD system is depicted in Figure 11. The setup comprises of feed tank mounted with heater, the hot water is circulated through the lumen side of HF-VMD module, while the shell side is maintained under vacuum. Vapor generated from shell side is condensed in condenser and collected in collection tank. For continuous operation, make up feed is supplied to feed tank and reject is purged from recycle stream.

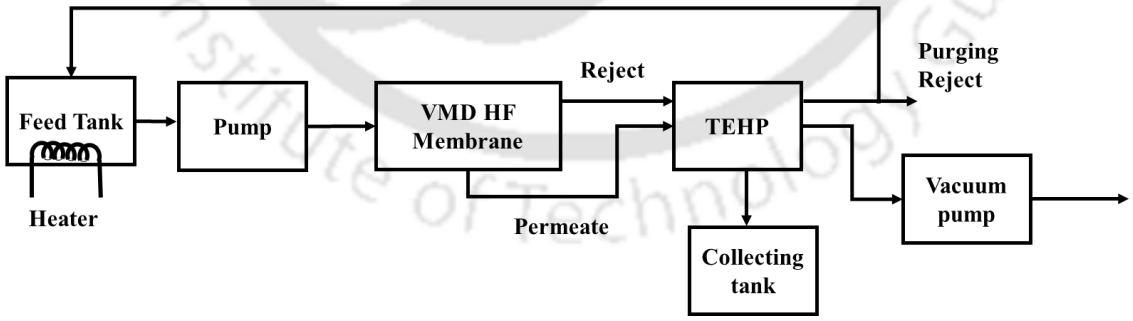

Figure 11 Process flow diagram of VMD setup

3.2 Model Hierarchy for Object-Oriented Modeling

Developing the mathematical model of PFD described in Figure 11 requires an Object-Oriented Modeling (OOM) approach to capture the complex interactions and dependencies among the various components of the VMD system. This approach allows for modular and reusable model development and easy integration and coherence between different sub-models. Moreover, an OOM approach can facilitate the analysis and optimization of the system performance by enabling sensitivity studies, parameter estimation, and scenario evaluation. Therefore, this study adopts an OOM approach to develop a comprehensive and flexible mathematical model for a VMD system.

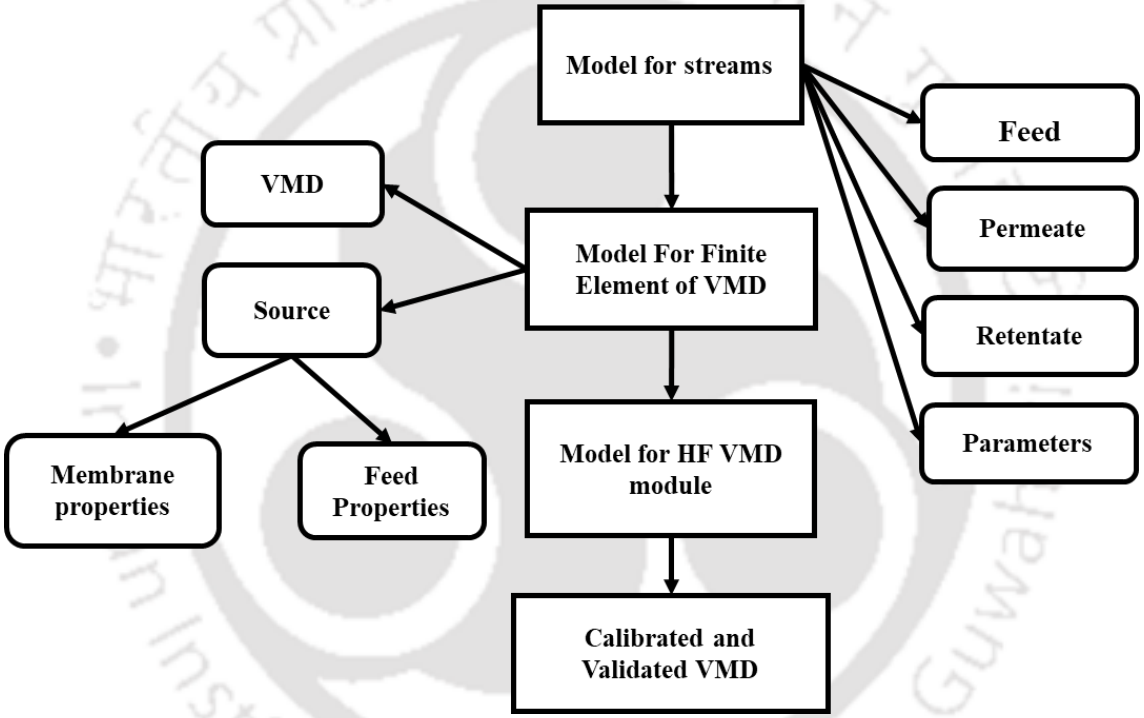

Figure 12 OOM hierarchy

The OOM hierarchy, as depicted in Figure 12 comprises of interconnected components that explains the operational details of the system. Central to this hierarchy is the flow stream connector, which describes various flow parameters within the system, including the feed, permeate, and retentate streams. The feed stream is used to define the aqueous feed solutions, while the permeate stream signifies the purified stream that has passed through the membrane, with retentate representing the concentrated aqueous solution post-separation. The parameters of all the models incorporated through connector named parameter. The values of all the parameters and process conditions passed through the source model such as membrane and feed properties. This allows an OOM approach where all the parameters are fixed from the top

layer of model architecture. This flow stream enables connectivity between different models of VMD.

3.3 Finite element 1-D mathematical modeling for the VMD module

VMD finite element model comprises essential streams like feed, permeate, and retentate. The governing model equations were explained in section **Error! Reference source not found.Error! Reference source not found.**. The mathematical model of single VMD finite element model is developed by solving mass, energy and momentum balance across the HF length and vapor transport across the membrane thickness.

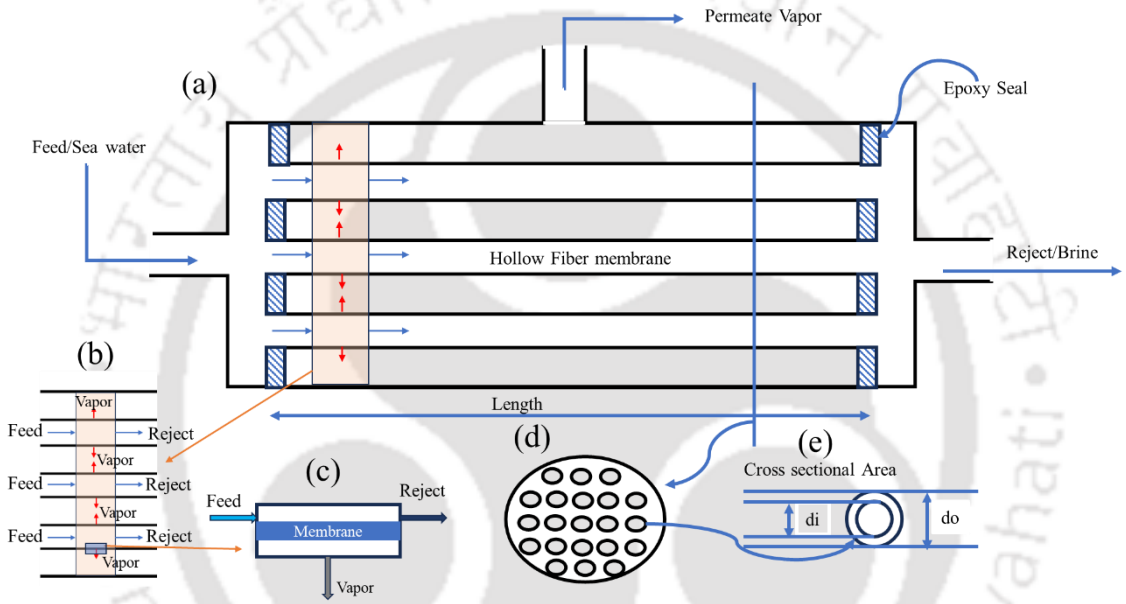

Figure 13 Modeling of VMD by Finite Element method

As illustrated in Figure 13(a), the model for VMD module is developed by segregating the HF model into ‘n’ number of Finite Elements (FE) along the length direction depicted in Figure 13Figure *12*(b), each represented as an individual localized single finite element. Then these individual elements considered as VMD finite elements are interconnected using flow stream connector.

Further, the individual FE-HF-VMD model is developed as described in Figure 13(c). Further Figure 13(d) provides a cross-sectional view of the hollow fibre module, and Figure 13(e) specifically illustrates the cross-sectional view of a single fibre. This comprehensive modeling and visualization are critical for describing the interactions within the module and for optimizing the system’s performance through detailed analysis.

3.3.1 Assumptions

These following assumptions are considered to simplify the model equation that will represent the actual VMD module used in the experimental study.

Table 9: Assumptions of mathematical model

Assumption	Justification	Expected Impact on Model Accuracy
Steady-state operation	Experiments were conducted after thermal and hydraulic stabilization; transient behaviour is negligible over long runs	Dynamic start-up effects and fluctuations are ignored, minor impact on long-duration operation predictions
1-D axial variation only	High aspect-ratio hollow fibers; dominant gradients are along the flow direction	Neglects radial non-uniformity, may slightly underpredict local flux variations near inlet region
Negligible radial gradients in temperature & concentration	Thin membrane and well-mixed lumen flow reduce radial resistance; vacuum side has minimal mass accumulation	Assumes uniform interfacial conditions, could marginally deviate under very high flux or viscous feeds
Ideal gas behaviour for vapor in membrane pores	Recovered vapor operates at low pressure and low partial density, real-gas effects minimal.	Minor error in vapor pressure estimation at high feed concentration or very low permeate pressure
Isothermal membrane matrix	Membrane has low thickness and high thermal conductivity; axial temperature drop dominates	Local conduction losses within membrane ignored, small underestimation of total heat loss

No heat loss to surroundings	Module is thermally insulated in lab setup, conduction/radiation losses limited	Could slightly overestimate energy efficiency in real systems with external losses
Concentration polarization modeled using film theory	MD hydrodynamics create a thin boundary layer near the membrane; film theory captures solute transport resistance without requiring detailed CFD	Minor underprediction at high flux or viscous feeds, but accurate for typical VMD operating conditions.
Lumen-side pressure drop calculated by modified Hagen–Poiseuille (laminar flow)	Flow inside narrow hollow fibers is predominantly laminar due to low hydraulic diameter and moderate Reynolds number; simplified formulation reduces computational complexity.	Slight deviation if flow transitions to turbulence, but negligible effect on thermal-driven flux prediction.
Vapor transport through the membrane is modeled as combined Knudsen + Poiseuille diffusion	The membrane pore size used in VMD (0.05–10 μm) places vapor flow in the transition regime, where both molecular collisions with pore walls (Knudsen) and gas-phase viscous flow (Poiseuille) occur simultaneously. This is widely adopted in MD literature to accurately represent mass transport when the mean free path of vapor is comparable to the pore diameter.	Neglecting slip-flow or surface diffusion introduces only minor error under VMD conditions. The combined mechanism accurately captures flux variation with pressure and temperature.

3.3.2 Mass and Energy balance

The mass balance for the single element shown in Figure 13(a) is given below.

$$F_f = F_r + F_p \quad 3\text{-}1$$

Where F_f is the volume flow rate of the feed stream, F_r is the volume flow rate of the retentate stream, and F_P is the volume flow rate of the permeate stream.

The solute balance for salt can be written below, where C_r, C_f, and C_p are the concentrations of retentate, feed, and permeate, respectively.

$$C_f \cdot F_f = C_r \cdot F_r + C_p \cdot F_p \quad 3\text{-}2$$

Since vapor flux in single finite element is constant, the permeate flow is calculated by multiplying flux with membrane surface area as shown in equation below.

$$F_p = N \cdot A_m \quad 3\text{-}3$$

where N is the mass flux and A_m is the membrane surface area.

For any VMD system in a permeate stream, there will be no solute, so the concentration of salts is zero ($C_p = 0$) as per vapor liquid equilibria at membrane pore water vapor alone transported and salt molecules are restricted to pass through the membrane pores.

Mass flux across the membrane is proportional to vapor pressure at the feed side and vacuum pressure at the permeate side where the proportionality constant is mass transfer coefficient.

$$N = K_m \cdot \Delta P \quad 3\text{-}4$$

$$\Delta P = \left(P_{fm}^o - P_p^o\right) \quad 3\text{-}5$$

where ΔP is the difference between vapor pressure of feed and permeate vacuum pressure, P_{fm}^o corresponds to the vapor pressure at the feed side and P_p^o is the vacuum pressure at the permeate side. N is the mass flux and K_m is the membrane mass transfer co-efficient respectively.

The vapor pressure at the liquid/vapor interface is correlated with temperature through Antoine's equation, assuming negligible curvature effects

$$P_{fm}^o = e^{A - \frac{B}{T_{fm} - C}} \quad 3\text{-}6$$

where P^{o}_{fm} and T_{fm} are vapor pressure and temperature at membrane interface facing feed side respectively. A, B and C are Antoine constants and the values taken to be 23.196, 3816.44 and 46.13 respectively[89]

As described in the section 2.1, the resistance of the membrane mass transport model that incorporates the mass resistance is shown in figure 5 . However, considering the mass transport domination of vapor at the experimental temperature and pore size of the membrane, the governing diffusion model is incorporated in the mathematical model. The governing equation to determine the mass transport is given by[137]

$$k_n = \frac{\lambda}{d_p} \qquad 3\text{-}7$$

wherein λ is the mean free path of water vapor and d_p is the membrane pore size.

The value of λ is calculated as per the below equation

$$\lambda = \frac{3\mu_v}{P}\sqrt{\frac{\pi R T_m}{8M_w}} \qquad 3\text{-}8$$

The bounds of highest and lowest mean temperature from the experimental data is used and the value found to be $0.084<\lambda>0.11\mu m$ which is comparable with the existing literature[138]. These values are substituted in the below governing equation, and the values lies in the range of $0.01 < Kn < 1$, confirming the combined dominance of Poiseuille flow and Knudsen diffusion as the primary mass transport mechanisms.

By summing up all these the terms K_m is calculated as summation of $K_{Poiseuille}$ and $K_{Knudsen}$. The overall mass transfer coefficient $K_{overall}$ can be calculated by using the resistance network model as shown below

$$\frac{1}{K_{overall}} = \frac{1}{K_f} + \frac{1}{K_m} + \frac{1}{K_s} \qquad 3\text{-}9$$

Where K_f is the feed side mass transfer and K_s is the permeate side mass transfer co-efficient respectively.

The permeate side mass transfer is neglected because of the low pressure maintained by the vacuum pump. So, equation 3-9 becomes as shown below.

$$\frac{1}{K_{overall}} = \frac{1}{K_f} + \frac{1}{K_m} \qquad 3\text{-}10$$

$$K_{Poiseuille} = \frac{r^2 \varepsilon}{\tau d} \cdot \frac{P_{av} \cdot Mw}{\eta \cdot \Re \cdot T_{avg}} \quad 3\text{-}11$$

Here, r is the pore size, ε is the fractional void volume of the membrane, δ is the membrane thickness, τ is the pore tortuosity

Mw is the water molecular mass and $\Re$ is the gas constant, T_{avg} is the average temperature across the membrane length, T_p is the temperature at permeate side and T_{fm} is the membrane feed surface temperature.

$$T_{avg} = \frac{T_p + T_{fm}}{2} \quad 3\text{-}12$$

3.3.3 Momentum balance

Pressure drop study along the HF-VMD module is studied using the Haigen Poiseuille equation as given below

$$\frac{\Delta P_m}{L_m} = \frac{32 \mu v}{{d_i}^2} \quad 3\text{-}13$$

Where ΔP_m is the pressure drop across the membrane length, μ is the viscosity of the feed liquid, v is the velocity of the feed liquid in the membrane module and d_I is the inner diameter of the hollow fibre membrane.

3.3.4 Concentration Polarization

Due to concentration polarization at feed side, partial pressure of feed at membrane surface is expected to be higher than the bulk feed vapor pressure. Therefore, film theory is used to calculate flux concentration variations in boundary layer near the membrane surface. The concentration and temperature profile are as shown in figure 1 and 2 respectively where the temperature at the membrane surface is expected to be lower than the bulk temperature due to heat loss through the membrane.

According to film theory solute balance in film boundary layer the equation for concentration of solute at membrane surface is derived and given below.

$$C_{fm} = C_{fb} \cdot e^{\frac{N}{K_f}} \quad 3\text{-}14$$

$$CPC = \frac{C_{fm}}{C_{fb}} \quad 3\text{-}15$$

where N is the mass flux of vapor and K_f is the mass transfer coefficient in the feed boundary layer, C_f is the bulk feed concentration, and C_{fm} is the solute concentration at the membrane surface. K_f can be evaluated using equation 3-17 below for mass transfer coefficient correlation.

$$Sh = a_2 . Re^{b_2} . Sc^{c_2} \quad 3\text{-}16$$

$$\frac{k_f L_e}{D_{ab}} = a_2 \left(\frac{d_i \, v \, \rho}{\mu}\right)^{b_2} \left(\frac{\mu}{\rho \, D_{ab}}\right)^{c_2} \quad 3\text{-}17$$

where L_e is effective length, D_{ab} is diffusivity of solute in bulk solution, μ is viscosity of feed ρ is density of feed and a_2, b_2, c_2 are mass transfer parameters respectively. This equation reflects the influence of concentration polarization, where a higher concentration gradient between the bulk and membrane surface leads to a reduction in the effective driving force (vapor pressure), thereby affecting the overall performance of the VMD process.

3.3.5 Temperature Polarization

The VMD process involves coupled heat and mass transfer, encompassing latent heat transfer during transmembrane vapor flux and heat conduction through the membrane matrix. The relationship between these transfers is intricate due to the presence of an unstirred boundary layer at the feed side, resulting in temperature polarization. This phenomenon leads to the membrane surface temperature T_{fm} being lower than the well-stirred bulk phase temperature T_{fb}, complicating the assessment of the driving force magnitude.

The liquid temperature at the membrane surface can be estimated by doing surface energy balance as shown in below equation 3-18.

$$\frac{k_m}{\delta} \cdot (T_{fm} - T_p) + N \cdot \Delta H = h_f \cdot (T_{fb} - T_{fm}) \quad 3\text{-}18$$

The empirical equations employed are usually written in simplified form:

$$Nu = a_1 . (Re)^{b1} \cdot (Pr)^{c1} \quad 3\text{-}19$$

$$\frac{h_f \, d_i}{k} = a_1 \cdot \left(\frac{d_i \, v \, \rho}{\mu}\right)^{b_1} \cdot \left(\frac{Cp \, \mu}{k}\right)^{c_1} \quad 3\text{-}20$$

Where a_1, b_1, c_1 are characteristic constants based on the module design and flow regime.

In VMD, the temperature polarization coefficient (θ) is defined as the ratio of the temperature at the feed side membrane interface to the bulk feed side. The co-efficient can be expressed as

$$\theta = \frac{T_{fm}}{T_{fb}} \qquad 3\text{-}21$$

Where, T_{fb} and T_{fm} are bulk feed temperature and temperature at the feed-membrane interface respectively.

The overall flux equation after incorporating the governing heat and mass transport equations is given as

$$N = K_{overall} \cdot \Delta P \qquad 3\text{-}22$$

Where, $K_{overall}$ is the mass transport combining both Knudsen diffusion and poiseulle flow and ΔP is the difference between vapor pressure at the feed side and vacuum pressure at the permeate side respectively.

Table 10 Boundary condition at the inlet and outlet of the membrane module

Equation	Domain	Axial position	Boundary condition	Physical meaning
Mass balance (feed side)	Lumen(feed)	Inlet, z=0	$m_f(0) = m_{f,in}$; $c_f(0) = c_{f,in}$	Feed mass flow rate and solute concentration specified at module inlet based on pump setting and feed composition.
Energy balance (feed side)	Lumen(feed)	Inlet, z=0	$T_f(0)=T_{f,in}$	Feed temperature at module inlet fixed by upstream heater.
		Outlet, z=L	$T_f(L)$ computed from integrated energy balance with latent heat loss	Outlet temperature is a model prediction reflecting cumulative heat transfer.

Momentum balance (feed side)	Lumen (feed)	Inlet, z=0	$P_f(0)=P_{f,in}$ (or specified by inlet pump/valve)	Inlet pressure set by feed pump / control valve
		Outlet, z=L	$P_f(L)$ obtained from integrated pressure-drop correlation	Outlet pressure is not imposed; it follows from Hagen–Poiseuille / friction model.
Solute transport / concentration polarization	Feed boundary layer	Inlet, z=0	$C_{m,f}(0)$ from film theory	Membrane-surface concentration at inlet obtained from local mass-transfer correlation.
		Outlet, z=L	$C_{m,f}(L)$ from same relation using local $C_f(L)$ and $J_v(L)$	Interface concentration at outlet is a result of local flux and bulk concentration.
Vapor transport / permeate side pressure	Shell/permeate	Inlet and outlet z=0, L	$P_v(0)=P_v(L)=P_{vac}$(const)	Vacuum pump maintains nearly uniform low pressure along shell; axial pressure gradient neglected.
Membrane energy balance	Membrane	All z∈[0,L]	Continuity of heat flux and temperature at both interfaces	membrane temperature is determined by local coupled balances.

3.4 Modeling of HF-VMD module

The development of the FE model for the HF-VMD module, as described in chapter 3.3, involves a 1D lumped system model suitable for short-length modules where variations in concentration and temperature are minimal and negligible. To extend this model to a distributed system capable of capturing axial variations in heat, mass, and momentum, the 1-meter length of the HF membrane is discretized into 'n' FE. Each element is treated as a lumped system, with its membrane surface area calculated using the following equation

$$A_{FE} = \frac{\pi\, d_i\, L_m}{n} \qquad 3\text{-}23$$

Where n is the number of fibers, d_i is the inner diameter of fiber and L_m is the length of the membrane.

The finite elements are connected in series to form a complete model for the HF-VMD module, as illustrated in Figure 14. This approach allows the model to account for axial variations by integrating permeate flux and feed mass balance across the fiber lumen. Section 3.3 provides details on the equations governing an individual finite element, while the present section elaborates on how these elements are connected to model the entire module.

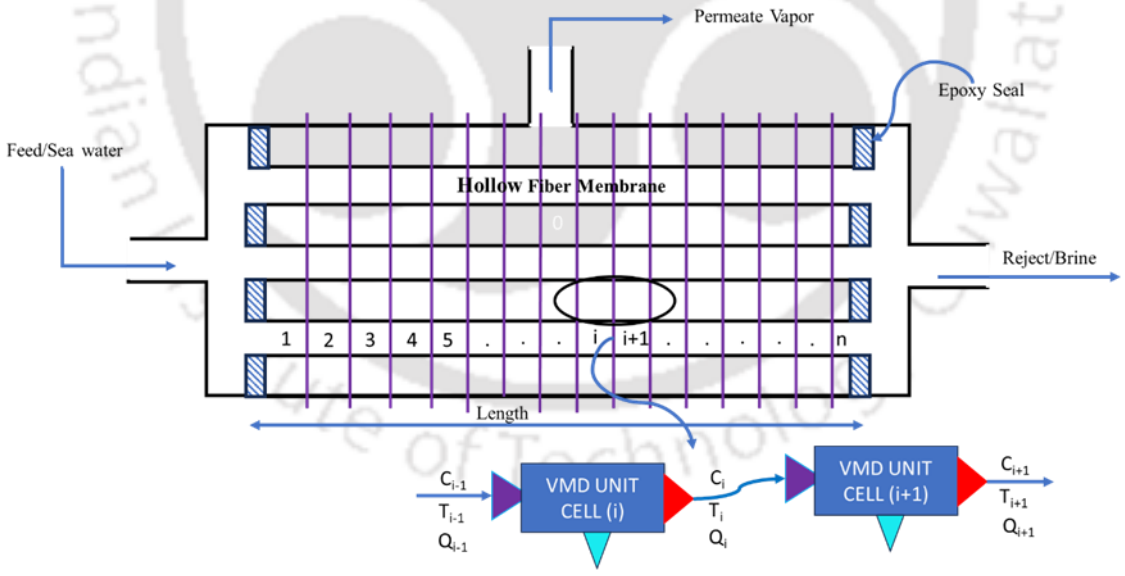

Figure 14: Discretization of HF membrane

3.4.1 Model Implementation

This system of nonlinear equations describe above for a HF-VMD module are solved by using Differential Algebraic System Solver (DASSL) available in DYMOLA (2023x) tool using Modelica (version 4.0.0), an object-oriented programming language which allows better model

reusability and efficiency. The model requires following inputs: feed temperature, flowrate, pressure, concentration, vacuum pressure, number of finite elements and model parameters to calculate the output variables of interest such as permeate flow and reject flowrate, temperature and concentration. The detailed model implementation follows the model hierarchy represented in section 3.2 where connectors are implemented to model for HF-VMD finite elements units and parameters are implemented. Then the flowsheet model for HF-VMD is developed.

3.4.2 Model Calibration

Some of the model parameters are estimated from experimental data as described in below model calibration section and the remaining parameters are fixed as per the module design data given by membrane supplier. The number of finite elements is estimated by performing Grid Independency Test (GIT).

After finding the optimal number of finite elements the model is calibrated and validated for coherence between experimental and simulation results were in 70% of the data is used for model parameter estimation(calibration) and 30% for model validation where the performance of model is evaluated by using estimated parameters. The unknown model parameters are estimated by formulating an optimization problem that minimizes the error between experimental observation and model prediction as shown in the objective function below.

$$\text{objective function} = \sum_{i=1}^{n} w_1 \left| N_{p_{model,i}} - N_{p_{exp,i}} \right| + w_2 \left| T_{r_{model,i}} - T_{r_{exp,i}} \right| + w_3 \left| P_{r_{model,i}} - P_{r_{exp,i}} \right| \quad \text{3-24}$$

subjected to $LB < \tau < UB$, $LB < a_1 < UB$, $LB < a_2 < UB$

Where the model parameters such as tortuosity (τ), the coefficients of heat and mass transfer correlation (a1, a2) are varied by using genetic algorithm (version 4.1 available in DYMOLA optimization toolbox) shown in Figure 15.

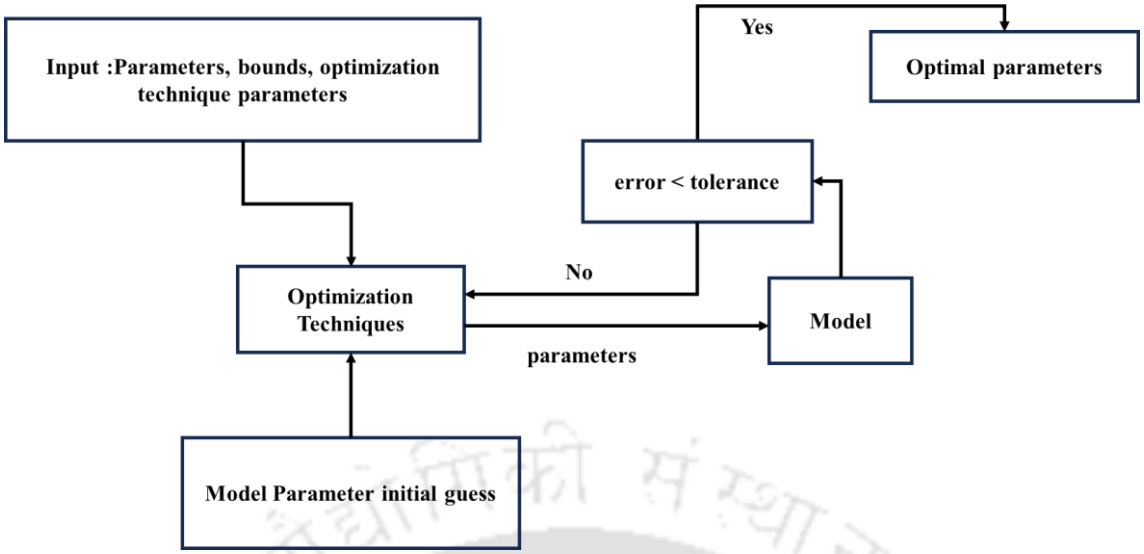

Figure 15: Optimization and calibration of the mathematical model

3.5 Integration of HF-VMD module with Energy recovery units

3.5.1 Modeling of TEHP module

TEHP model developed using lumped analysis approach was applied due to the relatively uniform temperature distribution within the TEHP module. The heat exchanger on the hot and cold sides had minimal dead volume with a residence time of 1.5 seconds, resulting in negligible dynamic variations. Numerical results were validated against experimental data, refining parameters like heat transfer coefficients and thermoelectric material properties to optimize energy efficiency and water production, ensuring feasibility for TEHP-VMD integration.

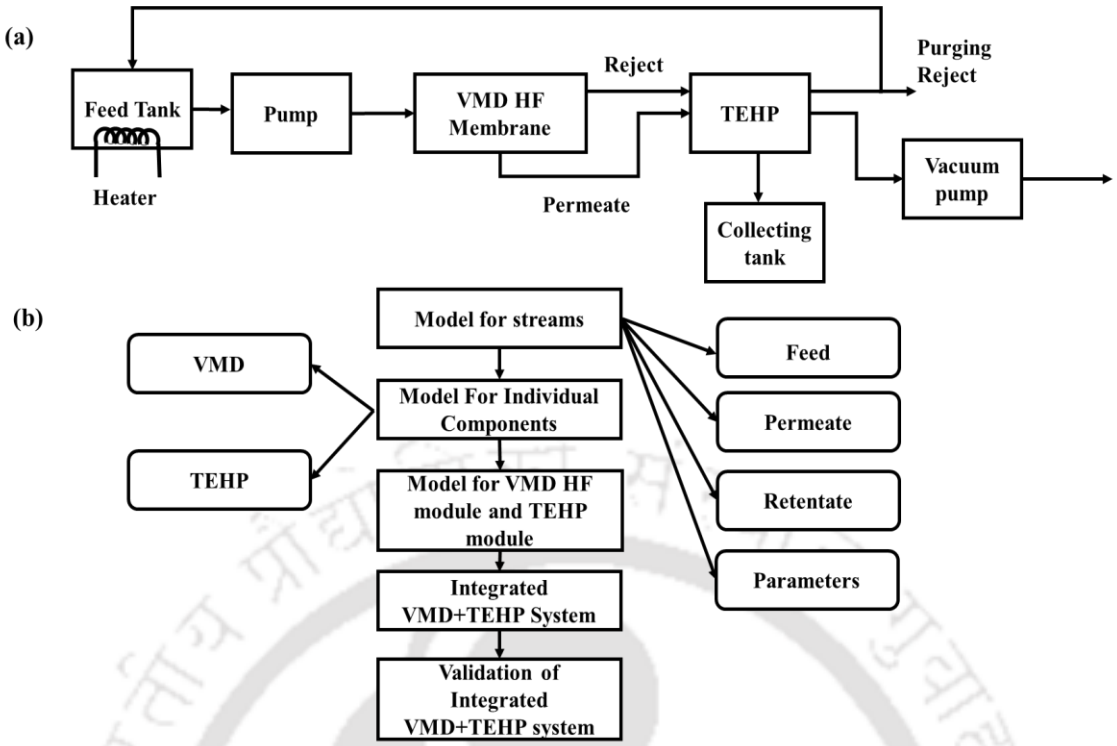

Figure 16: (a) PFD and (b) Modeling hierarchy of VMD integrated with TEHP system

3.5.1.1 Assumptions

- Heat loss from the system to its surroundings is negligible since it is well insulated.
- As planned, the model is developed for steady-state simulation to test and analyze the TEHP system for the HF-VMD+TEHP integrated system.
- Idealized Peltier performance, neglecting losses, focuses on core thermoelectric behavior, which is valid in optimized designs that minimize inefficiencies like electrical resistance.
- TEHP properties are constant across the length when operating within a narrow temperature range, avoiding unnecessary complexity due to minor variations in thermoelectric coefficients.
- The fluid properties used in this study are constant within the system's operating range

3.5.1.2 Mass Balance

The overall mass balance across the HX placed on two sides of the TEHP module is stated in the equation, where, $F_{H,in,}$ and $F_{H,out}$ are the flow rate of the feed entering and exiting at the hot

side HX, $F_{C,in}$ and $F_{C,out}$ are the flow rate of the feed entering and exiting at the cold side HX, respectively.

$$F_{\mathrm{H,in}} = F_{\mathrm{H,out}} \quad 3\text{-}25$$

$$F_{\mathrm{C,in}} = F_{C,\mathrm{out}} \quad 3\text{-}26$$

The electric power consumed by the TEHP module equals the product of the voltage input (V) and the electric current input (I), as stated in the equation.

$$P_{el} = V \cdot I \quad 3\text{-}27$$

3.5.1.3 Energy Balance

The electrical energy supplied to the TEHP module enables heat transfer from the cold to the hot side against the temperature gradient. Therefore, heat is removed from the cold side and added to the hot side, i.e., heat is transferred from the permeate vapor to the reject VMD water.

The equation gives the overall energy balance across the TEHP module

$$F_{\mathrm{H,in}}\,\rho Cp_{\mathrm{v}} T_{\mathrm{H,in}} + Q_{\mathrm{H}} = F_{H,out}\rho Cp_{\mathrm{v}} T_{\mathrm{H,out}} \quad 3\text{-}28$$

$$F_{\mathrm{C,in}}\,\rho Cp_{\mathrm{l}}\, T_{\mathrm{C,in}} - Q_c = F_{\mathrm{C,out}}\rho Cp_{\mathrm{l}} T_{\mathrm{C,out}} \quad 3\text{-}29$$

Where Q_{H} and Q_{c} are the heat load available at the hot and cold side, ρ is density, Cp_{v} *and* Cp_{l} are specific heat of hot and side water respectively.

3.5.1.4 TEHP Effect

Due to the Peltier effect, heat is transferred from low to high temperatures. The required heat transfer from the low to high-temperature side can be calculated as the sum of heat generated by the TEHP module due to electrical resistance and heat transfer by the Peltier effect.

The equation below asserts that the sum of electrical power input, heat transferred out, and heat transferred in must equal zero. This equation reflects the principle of conservation of energy, indicating that the total energy within the system remains constant.

$$Q_{\mathrm{H}} = P_{\mathrm{el}} + Q_{\mathrm{C}} \quad 3\text{-}30$$

Where P_{el} electrical input, Q_{H} and Q_{c} are the heat load available at the hot and cold side.

The heat transfer in the Peltier effect is represented by the Peltier coefficient term, along with two loss terms: conductive loss and Joule heating. The second term in the equation accounts for the Joule heating resulting from the current flowing through the TEHP module. The third term represents the conductive loss, which corresponds to the heat transfer due to thermal conduction between the hot and cold sides of the TEHP module.

$$Q_{\mathrm{c}} = \alpha T_{\mathrm{C}} I - 0.5VI - k(T_{\mathrm{H}} - T_{\mathrm{C}}) \quad \text{3-31}$$

Where α represents the Seebeck coefficient, and 'k' represents the thermal conductivity of the TEHP module.

The COP of a TEHP module measures its energy efficiency. It is the ratio of the desired heat gained (Hot or Cold side) to the input energy supplied to the module. $\mathrm{COP_H}$ on the hot side is expected to be consistently higher than one, but $\mathrm{COP_C}$ can attain less than one depending on the efficiency of the Seebeck effect of TEHP.

$$COP_{\mathrm{H}} = Q_{\mathrm{H}} / P_{\mathrm{el}} \quad \text{3-32}$$

$$COP_{\mathrm{C}} = Q_{\mathrm{C}} / P_{\mathrm{el}} \quad \text{3-33}$$

Where COP_{H} and COP_{C} are co-efficient of performance of hot and cold side respectively.

VMD+TEHP system of non-linear equations were solved using DASSL solver available in DYMOLA tool using modelica, an OOM language. The model equations were solved by giving model inputs such as feed temperature, feed flow rate, model parameters and fluid properties to find the output variables of interest such as outlet temperature. The detailed model implementation follows the hierarchy as shown in Figure 16(b). The developed HF-VMD+TEHP model is validated with experimental data generated in this work. This methodology systematically compares the model's predictions with actual measurements and iteratively refines the parameters to minimize the error function. The best parameters enhance the model's accuracy and reliability, making it a powerful tool for predicting system behaviour under various conditions. This process is crucial for validating theoretical models and ensuring their practical applicability in real-world scenarios.

3.5.1.5 TEHP system calibration

TEHP calibration involves tuning key model parameters to ensure the accuracy of simulation outputs against experimental data. For TEHPs, the primary tuneable parameters include the Peltier coefficient (α), electrical resistance (R), and total thermal conductivity (κ). These

parameters are pivotal in defining the thermoelectric effects, which are crucial for the TEHP's operational efficiency. The flowsheet for the model calibration in Dymola using a Genetic Algorithm (GA) is shown in Figure 15. The error function in this work is represented as

$$\in = \sum_{i=1}^{n} \left| T_{\mathrm{C,out_{exp,i}}} - T_{\mathrm{C,out_{model,i}}} \right| + \left| T_{\mathrm{H,out_{exp,i}}} - T_{\mathrm{H,out_{model,i}}} \right| \quad 3\text{-}34$$

Where n is the number of experimental data points.

3.5.1.6 Deployment of the flowsheet with recycle

As shown in Figure 16(a), recycling the reject stream in a VMD system enhances process efficiency. A steady-state tank model is developed to simulate the HF-VMD module with the reject recycle configuration. The tank serves as a reservoir for the feed to the HF-VMD module, where fresh feed and recycled reject streams are mixed, ensuring a uniform composition and temperature before re-entering the HF-VMD module. The flowsheet model is implemented in Dymola using an object-oriented drag-and-drop interface to connect the HF-VMD module, tank, and source stream for feed water using appropriate connectors. The OOM is deployed in as flowsheet approach, and the representation of the flowsheet is shown in Figure 16(b).

3.5.2 Modeling of Heat Exchanger

The HX model is developed based on the effectiveness Number of Transfer Unit (NTU) method to allow the prediction of both the outlet temperature. Upon integrating HX, the latent heat is attempted to recover and reheat the reject and fresh feed solution to minimize the heat load in the VMD system. The fundamental equations for the energy balance are defined in this section.

Mass balance of the exchanger as already discussed in the equation 3-25 and 3-26 respectively.

Heat capacity rate C (W/K) for the cold and hot side are given by the equation respectively

$$C_{\mathrm{cold}} = F_{\mathrm{cin}} C_{ph} \quad 3\text{-}35$$

$$C_{\mathrm{hot}} = F_{\mathrm{hin}} C_{pc} \quad 3\text{-}36$$

The amount of heat energy carried by the steam generated from VMD is given by the equation 3-37

$$Q_{\mathrm{steam}} = F_{\mathrm{hin}} \lambda \quad 3\text{-}37$$

Where λ is the latent heat of vaporization.

NTU of the exchanger can be calculated using the equation 3-38

$$NTU = \frac{UA}{C_{\text{cold}}} \tag{3-38}$$

Where U is the overall heat transfer co-efficient and NTU is the number of transfer unit.

Effectiveness of the exchanger is calculated based on the equation as shown below

$$\epsilon = 1 - \exp(-NTU) \tag{3-39}$$

Where ϵ is the Effectiveness of the exchanger.

3.5.3 Modeling of Vapor Compressor

Integration of VC is expected to improve the energy efficiency of the system as it increases both the temperature and pressure of the generated steam from the VMD system. The enhanced steam property is used to heat the reject and feed solution to compensate the energy loss occurred across the HF VMD module.

$$P_{out} = P_{in}\left(\frac{T_{out}}{T_{in}}\right)^{\frac{\gamma}{\gamma-1}} \tag{3-40}$$

Where P_{out} and T_{out} are the outlet pressure and temperature respectively from the VC, γ is the adiabatic index.

$$W = F_v(h_{out} - h_{in}) \tag{3-41}$$

Where h_{out} and h_{in} are the outlet and inlet enthalpy of the vapor, F_v is the vapor flowrate generated from the VMD system respectively.

3.5.4 Modeling of Heat pump

In the ideal vapor-compression refrigeration (VCR) cycle, the compression process is assumed to be isentropic, reversible and adiabatic. The refrigerant enters the compressor as a saturated vapor at the evaporator pressure and exits at a higher pressure as a superheated vapor. This high-pressure vapor then passes through the condenser, where it rejects heat at constant pressure and condenses into a saturated liquid at the condenser pressure. Following condensation, the refrigerant undergoes an isenthalpic expansion process through an expansion valve, reducing its pressure and temperature. It then enters the evaporator, where it absorbs

heat from the surroundings at low pressure, completing the cycle as it returns to the saturated vapor state.

This VCR cycle is applied in VMD system, where both heating and cooling are required. The evaporator side of the cycle is utilized to condense the saturated refrigerant vapor, while the condenser side is employed to heat the feed solution. The selected refrigerant, R-134a, circulates through the cycle, undergoing thermodynamic changes. It absorbs heat at the evaporator side, where it undergoes phase change from liquid to vapor, and releases heat at the condenser side and turns from superheated vapor to saturated vapor as shown in Figure 17.

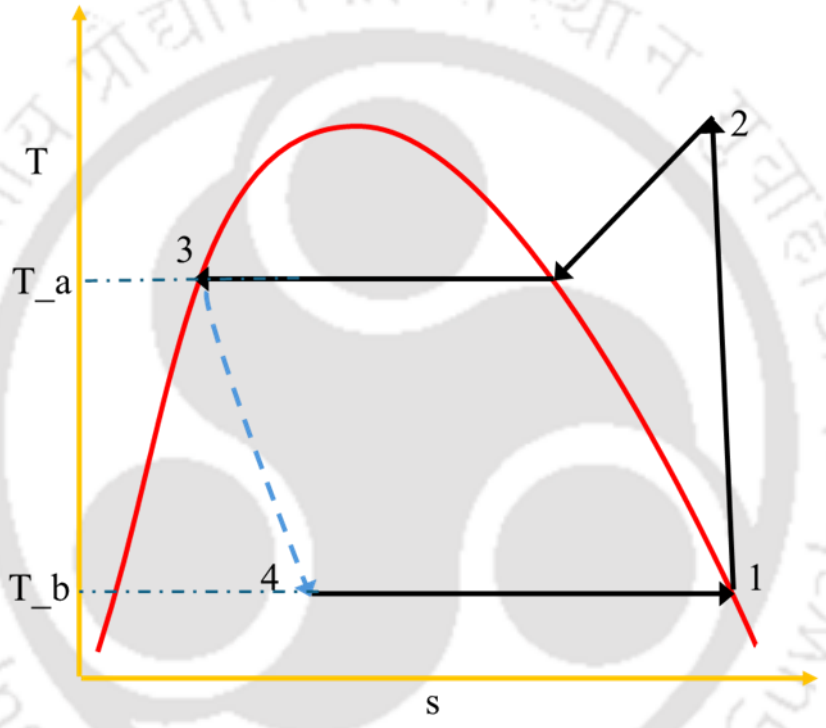

Figure 17 Ideal VCR cycle for heating and cooling application

Table 11: Refrigerant state in vapor compression cycle

Refrigerant	Equipment	Refrigerant state
1	Evaporator	SV
2	Compressor	SH vapor
3	Condenser	SV
4	Expansion valve	Partial VL

3.5.4.1 Assumptions

- The system is considered an ideal VCR Cycle.
- Enthalpy values are explicitly used for direct calculations and some values are interpolated. The stated values are collected from the R-134a property table.
- Steady state operation condition.
- Kinetic and potential energy changes are negligible.

3.5.4.2 Modelling equations for Heat Pump

Enthalpy of the superheated vapor after compression is calculated by interpolating the known values of enthalpy, corresponding to entropy s_1, since entropy at compressor inlet is equal to compressor outlet.

$$h_2 = h_{lower} - \left(\frac{s_1 - s_{lower}}{s_{upper} - s_{lower}}\right).\left(h_{upper} - h_{lower}\right) \quad 3\text{-}42$$

Where h_{lower}, h_{upper}, s_{lower} and s_{upper} are the lower and upper value of enthalpy and entropy, such that the s_1 value lies in between these values, and the h_{lower} , h_{upper} are selected accordingly.

Similarly, the temperature of the superheated vapor, T_2 can be calculated as given by equation (3-43)

$$T_2 = T_{lower} - \left(\frac{s_1 - s_{lower}}{s_{upper} - s_{lower}}\right).\left(T_{upper} - T_{lower}\right) \quad 3\text{-}43$$

The work input(W_{in}) the compressor is calculated by equation (3-44)

$$W_{in} = \mathrm{F}_{ref}.\left(h_{2out} - h_{1in}\right) \quad 3\text{-}44$$

Where F_{ref} is the flowrate of the refrigerant, h_{2out} is the enthalpy of superheated vapor and h_{1in} is the enthalpy of the saturated vapor respectively.

The heat removal rate (Q_L) is calculated as given in equation (3-45)

$$Q_L = F_{ref}.\left(h_{1out} - h_{4in}\right) \quad 3\text{-}45$$

Where Q_L is the heat load at the evaporator section of heat pump, h_{1out} and h_{4in} are enthalpy at evaporator inlet and outlet respectively

The heat rejection rate (Q_H) is calculated by equation (3-46)

$$Q_H = Q_L + W_{in} \quad 3\text{-}46$$

Where Q_H is the heat rejected by the condenser, and W_{in} is the work input to the compressor of the heat pump.

The outlet temperature of reject from the condenser($T_{out,cond}$) is given by the equation (3-47)

$$T_{out,cond} = T_{in,cond} + \left(\frac{Q_H}{\dot{F}_{cond}.C_{p,water}}\right) \quad 3\text{-}47$$

Where $T_{out,cond}$ and $T_{in,cond}$ are the temperature of the fluid at the inlet and outlet of the condenser respectively.

Chapter 04

Materials, Methods and Experimental procedure

4 Experimental Procedure, Material and Methods

This chapter details the methodologies and experimental techniques employed to evaluate the performance of the VMD system under various operating conditions as well as assessing the performance of TEHP system. This chapter also investigates the analytical procedures and protocols employed in characterizing the pitch sample.

4.1 Experimental Setup

4.1.1 Feed solution preparation

In this study, two distinct feed solutions were prepared to evaluate the performance of the VMD system. The first solution represented a low salinity feed, simulating brackish groundwater conditions, with a Total Dissolved Solids (TDS) concentration of 1 g/L. The second solution was a high salinity feed simulating sea water and concentrated brine conditions, with a TDS concentration of 35 g/L. To prepare the 1 g/L solution, deionized water was used, and the required amount of sodium chloride salt was accurately weighed using an analytical balance. Specifically, 1 gram of NaCl was dissolved in 1L of deionized water under continuous stirring to ensure complete dissolution and uniformity. Similarly, for the 35 g/L of feed solution, 35 grams of NaCl were dissolved in 1L of deionized water following the same procedure. Both solutions were prepared fresh prior to each experimental run to maintain consistency and minimize the risk of contamination or concentration changes due to evaporation or crystallization.

The brackish and seawater feeds were prepared as single-salt NaCl solutions to provide controlled and reproducible conditions for baseline flux measurements and model calibration. These synthetic solutions were intentionally used to avoid multi-ionic interactions, divalent ions, and premature scaling that could obscure fundamental heat and mass transfer behaviour. Accordingly, they are not intended to represent the full chemical complexity of real brackish or seawater. The salinity of each prepared feed solution was verified using a calibrated conductivity meter to ensure accuracy in the experimental setup.

4.1.2 VMD system

The experimental setup comprises a HF-VMD module and associated utilities, as depicted in Figure 18. The setup includes a 100 L capacity cylindrical feed tank equipped with an electrical heating system and an agitator to ensure uniform mixing of the feed solution. The heating

system consists of four electrical heating coils, each with a capacity of 6 kW, supplied by M/s Milman Thin Film Private Limited, India.

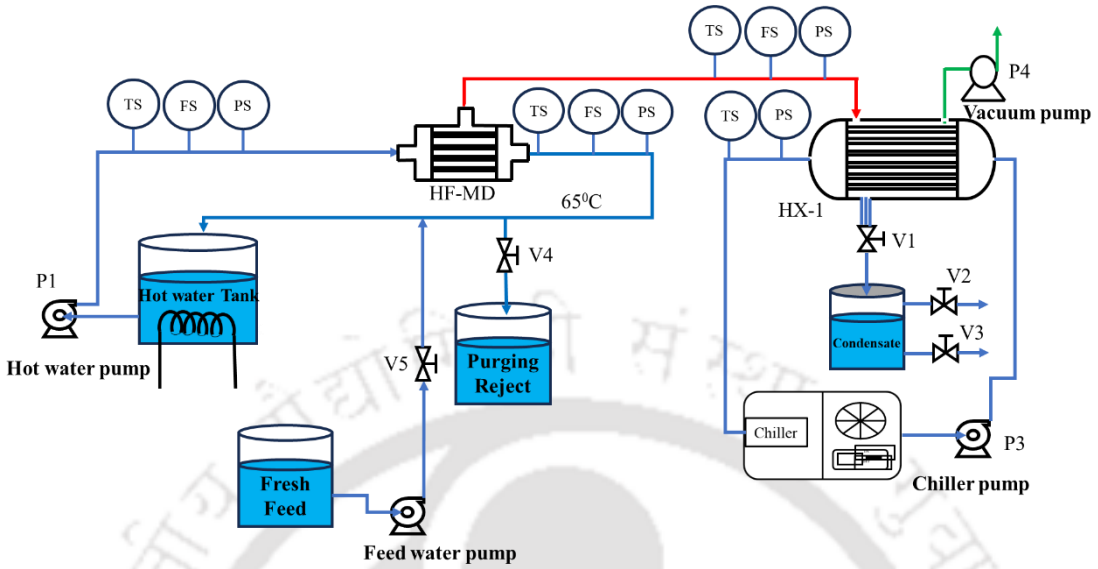

Figure 18: PID of the VMD experimental set up

The heating system is mounted circumferentially on the tank. A Proportional-Integral-Derivative (PID) controller (model TC-344) is used to maintain the feed tank temperature at the desired set point with high precision. The PID controller regulates the temperature with a variation of less than ±1°C. The hot water pump (1 HP) manufactured by M/s Marathon is employed for feed circulation through the HF-VMD module. The flow and temperature of the feed stream are continuously monitored using digital flow and temperature sensors with two-digit precision, supplied by M/s Amici Kart and M/s Selec Controls, USA, respectively. A digital pressure gauge with four-digit precision, manufactured by M/s ASCORP, is installed at both the feed and reject streams to measure process pressures accurately. All measuring instruments were calibrated against standard conditions before the commencement of experiments to ensure data accuracy. The experimental set up with its associated sensors and other equipment shown in Figure 19.

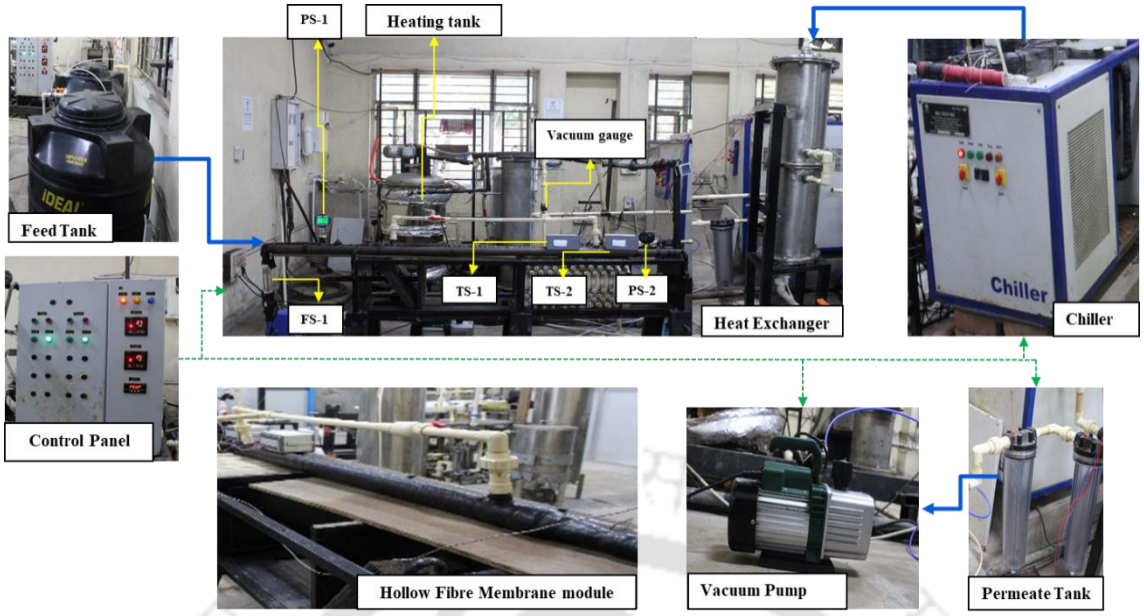

Figure 19: Experimental set up of VMD

Prior to experimentation, the feed solution's pH and conductivity were measured using a digital conductivity meter from M/s HANNA Instruments, USA, and the solution was then transferred to the hot water tank. The membrane used in this study is a HF membrane made of expanded polytetrafluoroethylene (ePTFE), with a pore size distribution ranging from 0.05 to 10 µm, supplied by M/s Dongyang Hanchen Membrane Technology Co. Limited, China. The detailed specifications of the HF-VMD membrane module properties were presented in Table 12.

Table 12: Specification details of membrane

Component	Make/Model	Specification details	Function in system
HF membrane	commercial ePTFE HF	Pore size: 0.05 to 10μm Porosity: 75% Thickness: 200 μm Material: Hydrophobic	Vapor transport and salt rejection
HF module geometry	Hanchen	No. of fibers: 270; Inner dia: 1.0 mm; Outer dia: 2 mm; length: 1000 mm	Provides high effective surface area for VMD
Feed circulation pump	Mono block centrifugal	Total membrane area: 1 m^2 Flow rate: up to 500 L/h; Max head: 1 b**ar**	Supplies feed through lumen of fibers
Vacuum Pump		Ultimate vacuum: 745 mmHg	Maintains low-pressure vapor side
Condenser	Shell and tube (SS104)	Coolant: Chilled water (5–15 °C) Tube side flow: 120–150 L/h	Condenses vapor to produce permeate
Feed Heater	12 kW helical coil heater	Temperature range: 25–80 °C	Maintains feed temperature
Temperature sensor	M/s Selec Controls	Accuracy ±0.15°C	Measures feed and reject temperature
Pressure gauge	Digital - ASCORP	Range: 0–1 bar Accuracy: ±0.2 kPa	Feed & vacuum line monitoring
Flow Sensor	Amici Kart (Digital)	Accuracy: ±2 digits Range: 1–500 L/h	Monitors lumen flow rate
PID Controller	TEC TC-344	Control accuracy: ±1 °C	Feedback control for feed heater

The vacuum system comprises a 1 HP vacuum pump supplied by M/s i-Rex, connected to the shell side of the membrane module. A vacuum gauge from M/s Ramco monitors the vacuum pressure. To handle the vapor exiting the shell side, the vacuum pump is connected to a condenser supplied by M/s Tech Inc. The condenser is cooled by chilled water maintained at a temperature range of 5 to15°C using a 2-ton refrigeration (TR) chiller, also supplied by M/s Tech Inc. Chilled water flows through the tube side of the condenser, ensuring efficient condensation of vapor. The condensed permeate is collected at regular intervals to measure its flow rate and quality.

4.1.3 TEHP system

TEHP's experimental setup consists of a water tank with a capacity of 50L and a centrifugal pump of M/s Kemflo with a rated capacity of 72 L/h. Two flow sensors make M/s Amici kart, and four digital temperature sensors make M/s Selec Controls, USA, with two-digit precision, were used to measure the flow and temperature of water entering the TEHP module and outlet temperature, as shown in Figure 20. This study used the TEHP module made by Hebei I.T. Shanghai (model TEC-12706). The detailed specifications for the TEHP module are shown below. An AC (Alternating Current) to DC (Direct Current) converter of M/s Scientific was used to ensure the regulation of the DC power supply to the TEHP module. Three TEHP modules are placed between the HX module.

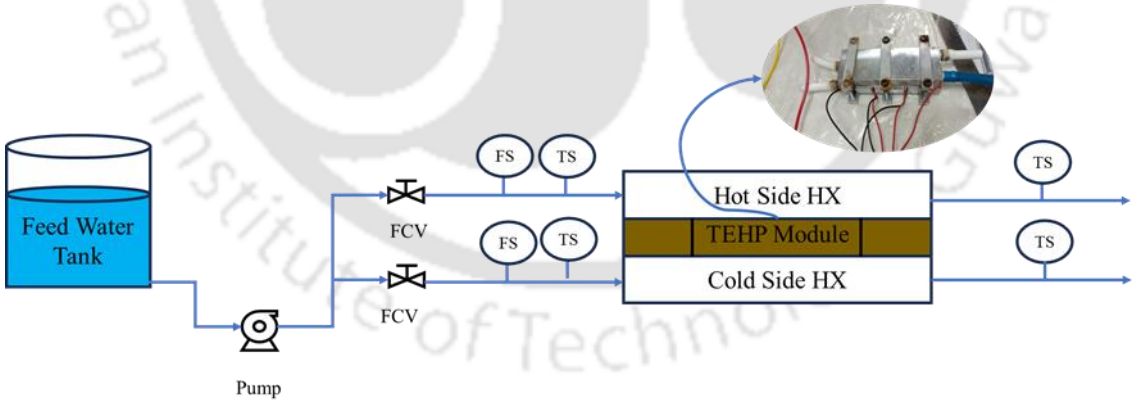

Figure 20: Experimental set up of TEHP system

4.2 Experimental Procedure

4.2.1 VMD system

In this study, the experiments were designed to evaluate the HF-VMD module's performance with respect to operating conditions such as feed flowrate, feed temperature, feed concentrations and vacuum pressure. To begin, the initial experiments were performed with pure water for a fixed vacuum pressure and feed temperature varying feed flowrate to find the optimum feed flowrate. The next set of experiments were performed by fixing optimum feed flowrate and varying feed temperature. Similarly, all the remaining variables are varied one by one where the remaining variables are fixed at its optimum condition. For the given fixed operating conditions, the experiment is started by filling the hot water tank with feed solution of desired concentration.

Feed solution is heated up to the desired temperature where agitator is on. The hot water pump is switched on to supply the hot feed to lumen side of HF-VMD module. Since the hot water is passing through the module the temperature is getting reduced to less than desired temperature, further supplying the heat to the hot water tank the desired temperature is achieved. Once it is achieved, vacuum pump is switched ON. Under this operating condition, feed flowrate, feed temperature, reject pressure, reject temperature, permeate flowrate, vacuum pressure was monitored and maintained to its desired operating conditions. Wherein both conductivity and flowrate of permeate is measured for every one hour. The vacuum pressure can be controlled through the control valve between HF-VMD module and vacuum pump. Permeate gets start collecting in permeate collection tank and they are collected by closing the valve V1 and opening the valves V2 and V3. During normal operation V1 is open and V2 and V3 were closed as shown in Figure 18.

Each VMD experiment was conducted following a standard procedure as the membrane module was installed, and the system was allowed to circulate the feed solution at the desired flow rate and temperature while the vacuum pump was initiated on the permeate side to attain the target transmembrane driving force. After start-up, the system was allowed to stabilize until the feed temperature, feed/permeate pressures, and permeate flux showed no noticeable drift. Steady state was confirmed when the measured operating variables (feed temperature, pressure, and vapor flux) varied by less than ±3% over a continuous period of at least 30 minutes. Only data collected within this steady-state window were used for the calculation of flux and rejection performance.

All VMD experiments were performed in triplicate for each operating condition to ensure reproducibility. The reported values of permeate flux and rejection correspond to the arithmetic mean of these three independent measurements. The uncertainty for each data point is presented as the standard deviation of the replicates, representing the experimental variability under identical conditions. Error bars shown in the figures therefore indicate one standard deviation from the mean.

4.2.2 Sample preparation of Pitch

4.2.2.1 ICP-MS

Samples for ICP-MS analysis were prepared by acid digestion using analytical-grade nitric acid. Liquid samples were diluted appropriately to fall within the calibration range, while solid pitch samples were digested under controlled heating conditions to ensure complete metal dissolution. Calibration was performed using single-element molybdenum standard solutions, and linear calibration curves with correlation coefficients ($R^2 > 0.99$) were obtained. The limit of detection (LOD) for Mo was determined as three times the standard deviation of procedural blanks and was fixed at 1 $\mu g \cdot L^{-1}$, while the limit of quantification (LOQ) was defined as ten times the blank standard deviation. All measurements were conducted in triplicate to ensure reproducibility.

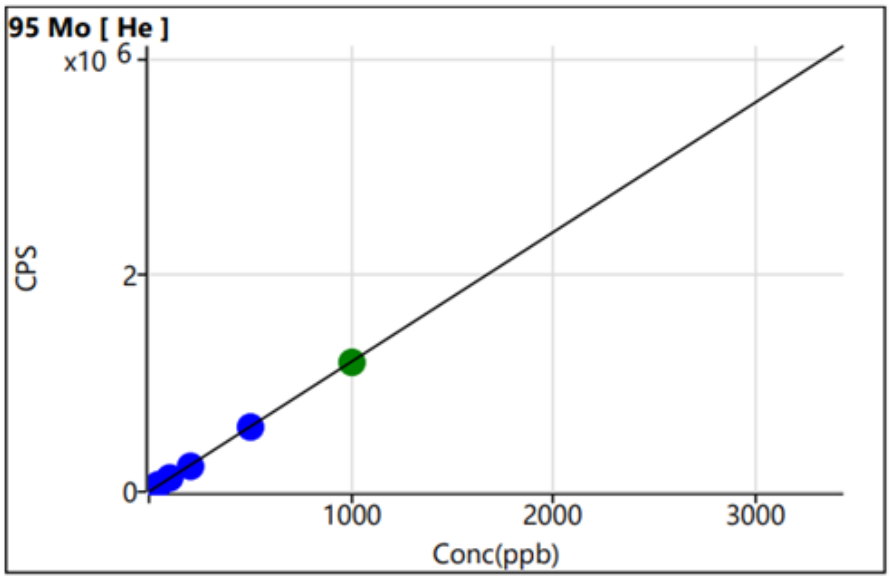

Figure 21: Calibration curve for Mo in ICP-MS analysis

4.2.2.2 XPS

X-ray photoelectron spectroscopy (XPS) samples were prepared by drying and mounting representative solid samples on conductive carbon tape. Spectra were acquired under high vacuum conditions using monochromatic Al Kα radiation. Binding energies were calibrated using the C 1s peak at 284.8 eV as a reference. The analysis focused on identifying elemental composition and oxidation states on the sample surface.

4.2.2.3 X-Ray Diffraction

XRD analysis was carried out on dried solid samples to identify crystalline phases formed during the experiments. Samples were finely ground to minimize preferred orientation effects and scanned over a suitable 2θ range using Cu Kα radiation. Phase identification was performed by comparison with standard diffraction patterns from reference databases.

4.2.2.4 Thermo Gravimetric Analysis

TGA was conducted on dried samples to assess thermal stability and compositional changes. Measurements were performed under a controlled inert atmosphere with a constant heating rate. Sample mass loss profiles were recorded as a function of temperature to identify thermal decomposition and volatilization behaviour.

4.2.3 Protocols for handling the pitch and sample preparation

Experiments and acid digestion were conducted in accordance with established laboratory safety protocols. Acid digestion procedures were performed in a fume hood using appropriate personal protective equipment, including chemical-resistant gloves, safety goggles, and lab coats. Concentrated acids and digested samples were handled with caution to prevent exposure and contamination. All acidic wastes and metal-containing residues were neutralized and disposed of following institutional hazardous waste management guidelines and local environmental regulations.

4.2.4 TEHP system

Flow and temperature sensors were calibrated using a thermometer for temperature measurement and by determining the volumetric flow rate through a standard beaker over a fixed time interval. After calibration, TEHP experiments are performed by manipulating the water flow rates to the module between 5 and 30 L/h on both sides. The DC power supply successfully maintained a voltage of 12 V and a current of 6 A, ensuring the TEHP module operated at its maximum limits. The temperature of the hot side outlet stream is increasing, and the cold end outlet stream is decreasing from its respective feed temperature. During experiments, a constant flow rate is fixed on one side of the TEHP module, and the flow rate varies on the other side of the TEHP module as shown in Figure 20. Thus, the performance of the TEHP module is evaluated concerning hot and cold side surface temperature and its COP.

4.2.5 Uncertainty analysis

All experimental measurements were subjected to rigorous uncertainty analysis to ensure the reliability and validity of the results. Standardized methodologies for evaluating experimental uncertainty were employed, consistent with the recent investigations in MD systems[89]. A comprehensive summary of the estimated uncertainties for the primary measured variables and derived parameters is provided in Table 13 . Temperature measurements were performed using calibrated K-type thermocouples, with a specified accuracy of ±0.5 °C. The feed flow rate was controlled using a metering pump and independently verified using a rotameter, yielding an estimated uncertainty of ±2% of the reading (equivalent to ±0.1 L/min at typical operating conditions). Vacuum pressure measurements were obtained using a digital vacuum gauge, with an uncertainty of ±0.2 kPa across the relevant operational range.

Table 13 Estimated uncertainties in experimental measurements

Quantity	Instrument / Method	Uncertainty
Temperature	Digital with K-type thermocouple	±0.5 °C
Feed flow rate	Rotameter (5 - 100 L/h range)	±2% of reading (±0.1 L/h)
Vacuum pressure	Digital vacuum gauge	±0.2 kPa
Collected volume	Graduated cylinder	±5 mL
Time (for flux calc.)	Digital stopwatch	±0.5 s

Derived: Flux	Calculated from volume, area, and time	±~5%
Derived: COP	Calculated from ΔT and power readings	±~3%

Permeate flux (expressed in LMH) was determined based on the collected volume and membrane area. The associated uncertainty was calculated by propagating the individual measurement errors in volume (recorded using a 1000 mL graduated cylinder with ±5 mL accuracy), time (measured with a digital stopwatch with ±0.5 s precision), and membrane area (considered negligible due to precise and consistent membrane dimensions). Employing the Kline and McClintock error propagation method, the relative uncertainty in flux was estimated to be approximately ±5%.

All experimental data are reported with error bars corresponding to ±1 standard uncertainty. For instance, during integrated VMD-TEHP operation at a feed flow rate of 5 L/h and a feed temperature of approximately 60 °C, the observed permeate flux was 2.4 ± 0.1 L/m²·h (±4.2%), while the hot-side COP of the TEHP was recorded as 1.10 ± 0.05. These quantified uncertainty margins underscore the statistical significance of the performance enhancements observed upon TEHP integration. The systematic quantification and propagation of measurement uncertainties provide a robust foundation for model validation and performance evaluation, thereby enhancing the overall credibility of the experimental findings.

4.3 Materials and methods

4.3.1 Material

The heavy hydrocarbon pitch used in this study was derived from a vacuum residue conversion process developed by IOCL, which employs a slurry-phase reactor for the production of middle distillates using oil-soluble, sulphide organometallic catalysts containing molybdenum (95–99 wt%). This metal, upon catalyst deactivation, accumulate in the pitch fraction (boiling point >540 °C), representing 5–10 wt% of the fresh feed. The pitch was first subjected to comprehensive characterization using XPS, XRD, TGA, EDX, FESEM, and ICP-MS to understand the interactions of molybdenum and nickel with elements like sulfur, nitrogen, and carbon, and to assess metal distribution, valency, thermal behaviour, and elemental concentration. These findings inform the leaching process, wherein ground pitch particles are contacted with aqueous or acid-based solvents under hydrothermal conditions (50–150 °C, 1–20 bar) for selective metal recovery. Both sequential and single-step selective leaching strategies for molybdenum extraction were explored.

4.3.2 Characterization techniques

To comprehensively investigate the interaction metal ion such as molybdenum within the pitch matrix, a range of advanced characterization techniques was employed. These methods provided complementary insights into the chemical bonding, structural arrangement, thermal stability, concentration of metal ion and elemental composition of the samples.

4.3.3 EDX

FESEM analysis was performed using a Carl Zeiss Sigma 300 VP Field Emission SEM, designed for high-resolution imaging and surface characterization. This instrument employs a field-emission cathode that delivers a focused electron beam with minimal energy dispersion, enabling imaging at resolutions down to 1 nm. It is equipped with in-lens SE, standard SE, and BSE detectors, facilitating detailed analysis of surface morphology, contrast, and elemental composition. The pitch samples were examined to assess the distribution and surface interaction of metal ions, as well as structural textures, across a magnification range of 10 to 300,000.

4.3.4 TGA

Thermal analysis was performed using a Netzsch STA 449 F3 Jupiter system (Model: STA449F3A00), which integrates both TGA and Differential Scanning Calorimetry (DSC) in a single platform. This system allows simultaneous measurement of mass change and heat flow from room temperature up to 1200°C. TGA tracks weight loss related to thermal decomposition, while DSC detects endothermic or exothermic transitions by measuring the heat flow difference between the sample and a reference. This dual capability makes the instrument particularly useful for assessing thermal stability, decomposition patterns, and phase transitions in a wide range of materials. TGA/DSC analysis is particularly valuable for characterizing heavy fraction pitch due to its complex mixture of high-molecular-weight hydrocarbons and metal-containing species. Using this technique, the thermal decomposition behaviour of pitch can be systematically studied by monitoring weight loss across a controlled temperature range.

4.3.5 XRD

XRD analysis was carried out using a Bruker D8 XRD system equipped with a Copper K-alpha radiation source to minimize another compound interference. The system includes a high-efficiency 1 kW line-focus X-ray source and detector, enabling high-speed data acquisition

with superior angular resolution and peak clarity. Powdered samples of pitch were analysed to investigate phase composition, crystallite size, and strain broadening. The system is well-suited for phase identification, microstructural analysis, and crystallographic characterization. The samples were finely ground and pressed into flat holders. Scans were performed in the 2θ range of 10°–90° with a scan rate of 10°/min.

4.3.6 XPS

XPS analysis was conducted using the PHI 5000 Versa Probe III system (M/s Physical Electronics, USA), equipped with a monochromatic, micro-focused X-ray source. The instrument offers high-resolution surface chemical analysis with an information depth of approximately 5 nm. Its micro-beam capability (beam size <10 µm) enables detailed spectroscopy, imaging, and depth profiling. Elemental distribution across the surface was obtained via raster scanning, while compositional depth profiling was achieved through ion sputtering. The system supports advanced features such as angle-resolved XPS and vacuum transfer for air-sensitive samples, making it well-suited for the analysis. Samples were pelletized and mounted onto conductive stubs using carbon tape. The spectra were collected in the binding energy range of 0–1200 eV, with high-resolution scans focused on the Mo 3d. Deconvolution was performed using a mixed Gaussian–Lorentzian fitting to determine oxidation states and chemical environments.

4.3.7 ICP-MS

ICP-MS analysis was carried out using an Agilent 7900 ICP-MS system, designed for ultra-trace elemental analysis with high precision and sensitivity. The technique operates by introducing liquid samples into an argon plasma, where they are atomized and ionized. The resulting ions are then separated based on their mass-to-charge ratios in a quadrupole mass spectrometer. For this study, pitch samples were digested using a microwave-assisted acid digestion protocol involving nitric acid to ensure complete dissolution of the heavy hydrocarbon pitch.

Chapter 05

Results and Discussion

5 Results and Discussions:

This chapter presents the experimental and theoretical results relating to the performance and concentration of salt using VMD, the energy recovery potential of TEHP integrating with VMD further with equipment such as HX, VC and HP, and finally the extraction of molybdenum from pitch are all thoroughly interpreted and discussed.

5.1 Model Calibration

5.1.1 VMD system

The model calibration requires the upper and lower bound of the decision variable and are given in Table 14. Further, to solve the optimization problem, the weights of error function w_1, w_2, w_3 must be known wherein w_1 for permeate flux, w_2 for reject temperature and w_3 for reject pressure.

Table 14 Constraints and Bounds

Decision Variable	Min	Max
τ	2	3
a_1	0.001	0.1
a_2	0.001	0.1

These weight parameters can be estimated either by using secondary optimization loop in addition to described in parameter estimation section or trial and error approach. The first approach may lead to complex optimization problems which are not part of this manuscript scope. Therefore, these weights are estimated in the trial-and-error method. The total number of experimental points available for parameter estimation and validation is 60, a further 40 points were used for parameter estimation and 20 points used for validation. In this method, all three weights are systematically varied as shown in Table 15 to calculate model parameters and corresponding error values. The w_1 represents permeate flux and model is expected to predict permeate at high accuracy, w_1 was fixed to be 1 for all the cases. The subsequent important model prediction parameters were reject temperature, and reject pressure. These weights are manipulated between 0 to 1.

Table 15 Model Calibration for Parameter Estimation

Weights			Estimated Parameters			Calibration	Validation	% Difference
w_1	w_2	w_3	τ	a_1	a_2	MAE	MAE	
1	0	0	2.52	0.002	0.023	4.502	4.387	2.55
1	1	0	2.6	0.018	0.024	3.205	3.186	0.59
1	1	1	2.62	0.027	0.029	2.866	2.530	11.73
1	**0.5**	**0.5**	**2.68**	**0.012**	**0.032**	**1.522**	**1.256**	**17.47**
1	0.5	0.001	2.72	0.0115	0.032	1.837	1.495	18.62
1	0.001	0.001	2.54	0.0082	0.027	3.703	3.527	4.75

As shown in Table 15 the Mean Absolute Error (MAE) values for the model in calibration varies with changing weights and the least error is found for the case of w_1, w_2, and w_3 are 1, 0.5, 0.5 respectively. The lowest calibration MAE is 1.522 and then further it increases when reducing the weight for w_2 and w_3, so which indicates that the optimum weight for this case is somewhere around w_1 is 1 and w_2 is 0.5, w_3 is 0.5. Similar observations on MAE for validation dataset conclude that model is capable of predicting unseen data. Experimental observation and model prediction of all the 60 points are shown in Figure *23* to Figure *30* respectively. The results conclude that the model is able to predict within the error value of 1.5% for permeate flux, 1% for reject temperature and 1% for reject pressure. There were no significant changes in the values of b, c and b1 and c1 in the parameter estimation. The overall model parameters and its estimated value is presented in the Table 16.

Table 16: Estimated parameters from model

Tortuosity	Heat Transfer parameters from Dittus- Boelter relation			Mass Transfer parameters from Sherwood relation		
τ	a	b	c	a1	b1	c1
2.68	0.012	0.8	0.33	0.032	0.6	0.33

5.1.2 TEHP system

The TEHP model was validated before being integrated with the HF-VMD model. For the calibration of the TEHP model, it is crucial to establish the bounds for the decision variables, including the Seebeck coefficient (α), thermal conductivity (k), and electrical resistance (R) of the TEHP module. These parameters, initially unknown, must be calibrated to achieve accurate model predictions and optimize the system's performance. The calibrated values obtained were

$\alpha = 0.028$, $k = 0.189$, and $R = 1.2$ by calibrating with actual experimental conditions using the Dymola calibration toolbox. The model effectively predicts the COP and the hot and cold outlet temperatures, aligning closely with the expected system behaviour.

5.2 Performance analysis of VMD system by varying operating conditions

The performance of HF-VMD module is investigated by using both experimental data and validated with the HF-VMD model. The analysis focuses on identifying the optimal operating conditions within the experimental range explored in this study. The validated model is then employed to investigate the variations in process parameters and flux along the membrane length, providing a deeper understanding of the module's performance. This model is used to simulate the impact of all operating parameters on the overall performance of the HF-VMD module.

5.2.1 Grid independency test

To ensure the results are invariant of size and distribution of number of finite elements a GIT is proposed. The primary focus of GIT is to find the right balance between computational efficiency and model accuracy. Simulation studies for finite elements from 1 to 14 were performed, and the relative absolute percentage change (RAPC) is observed to be invariant after 10. Hence the optimized number of FE is found to be 10 as the RAPC in permeate flux is <1% as shown in Figure 22 So, each FE is modeled with a length of 0.1m as shown accounting for a membrane total length of 1m.

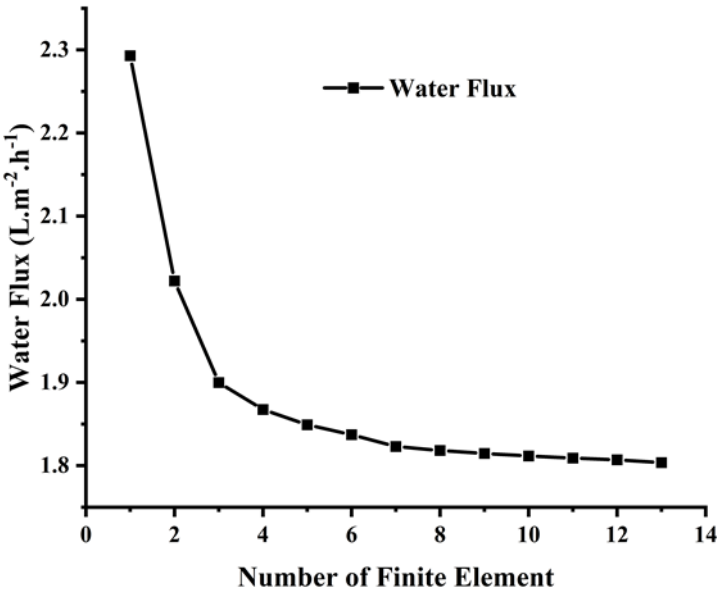

Figure 22: Grid Independency Test

5.2.2 Effect of feed flowrate

The HF-VMD module performance is studied by varying the feed flowrate from 150 to 200 L/h for the fixed temperature of 333K, salt concentration 1g/L and absolute vacuum pressure of 7.3 kPa, the observed flux improved by around 25% by increasing feed flowrate from 150 to 200 L/h as shown in Figure 23. The experimental maximum feed flowrate is limited to 200L/h since the LEP of the membrane (1.5 bar) at the feed temperature of 333K is very closer at this flowrate. However, in this study, mathematical model is used to simulate for higher feed flowrate to study the module performance at higher flowrates as shown in Figure 24. For conducting the experiments at higher flowrates, one of the methods can be HF diameter can be increased such that the optimum pressure drop is achieved simultaneously mechanical strength of the HF sufficient to hold the vacuum required for VMD. Increasing the flowrate also contributes in increase in the membrane interface temperature along with heat transfer coefficient as shown in Figure 25.

Similar to flux, the reject temperature is also linearly increasing with the increase in the feed temperature. As described for heat and mass transfer equation across the membrane when temperature at the membrane surface increases both the heat flux and conduction loss is expected to increase simultaneously. This will lead to higher heat loss through the membrane, however, beyond certain flowrate the improvement in the flux will be limited. Therefore, the

simulated reject temperature for higher feed flowrate is observed to be exponential increase. According to the Haigen Poiseuille equation, while increasing the feed flowrate, the pressure drop increases as shown in Figure 23.

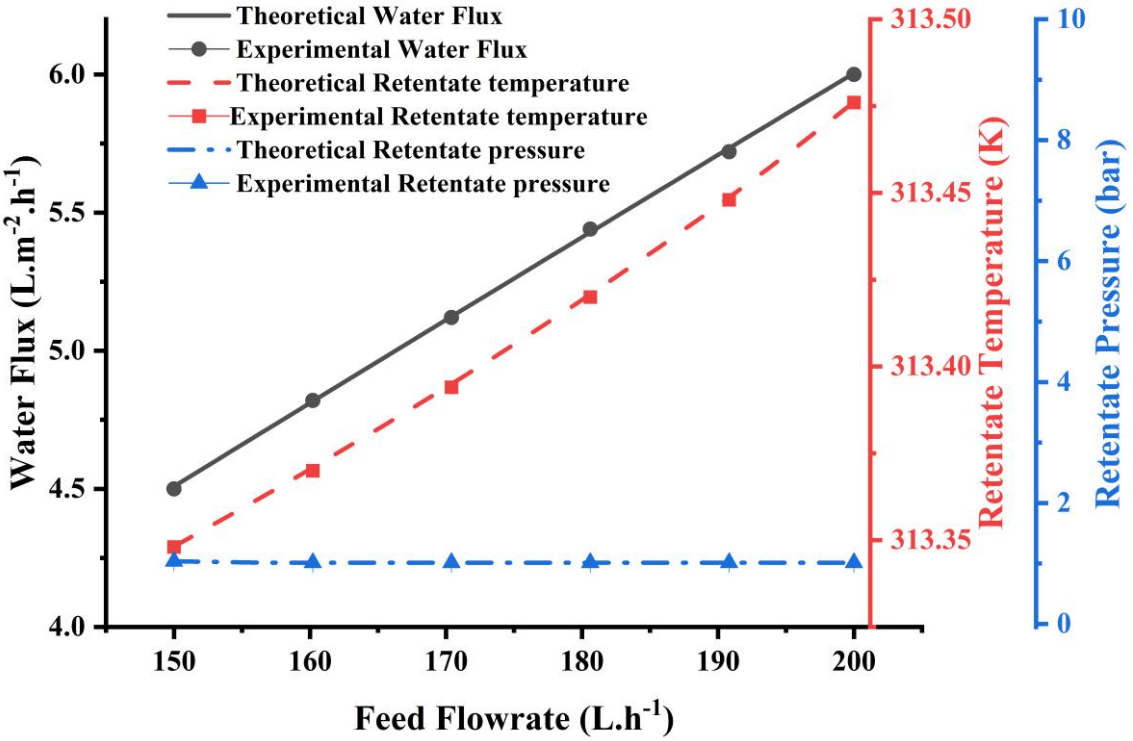

Figure 23: The effect of feed flowrate(L/h) on flux at the operating conditions: Temperature 333K, Feed concentration 1 g/L, Vacuum Pressure 7.3 kPa

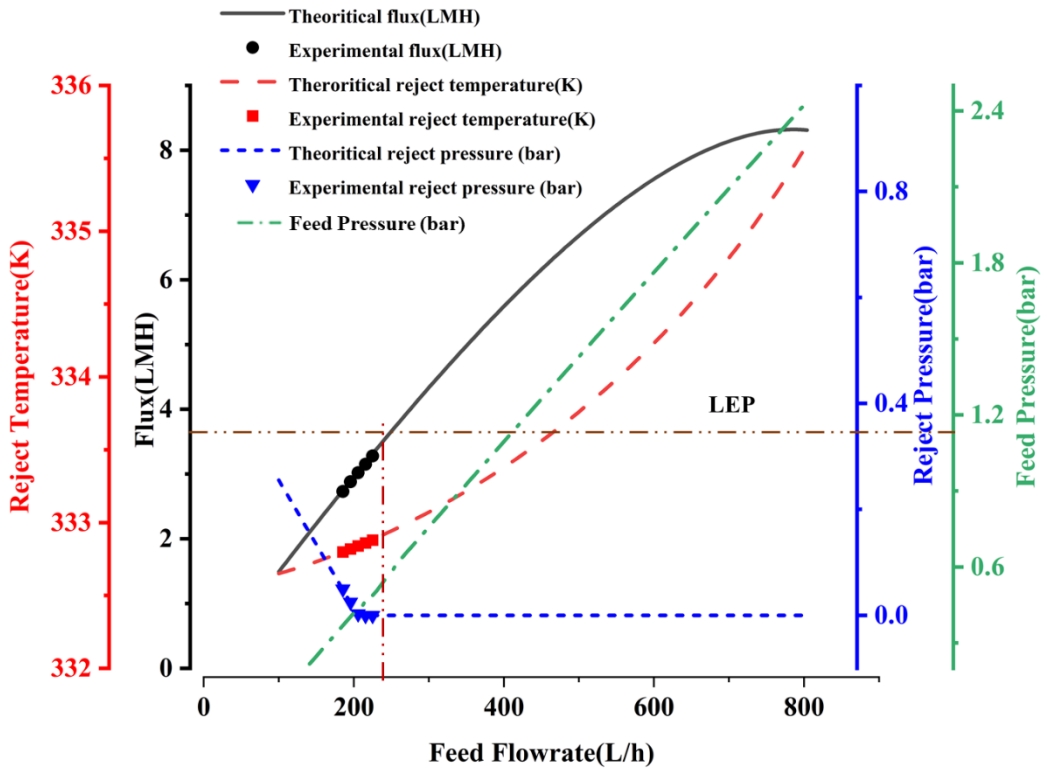

Figure 24: The effect of feed flowrate(L/h) on flux at the operating conditions: Temperature 343K, Concentration 1 g/L, Vacuum Pressure 20kPa

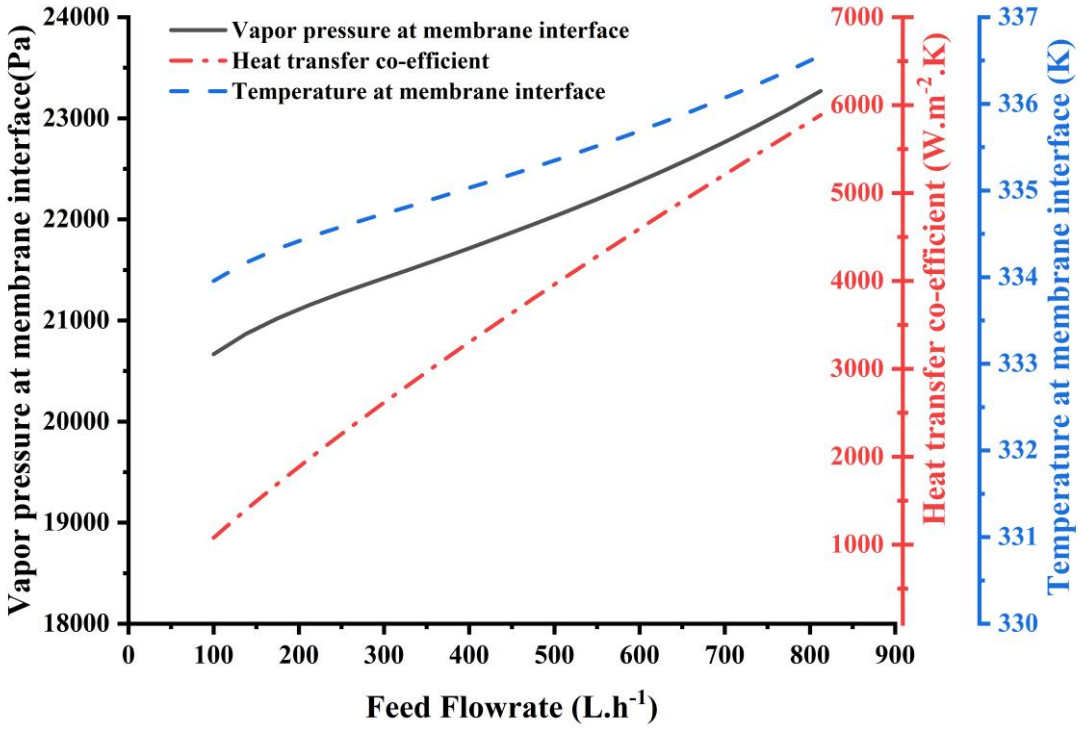

Figure 25: The effect of feed flowrate(L/h) on flux at the operating conditions: Temperature 333K, Feed concentration 1 g/L, Vacuum Pressure 20 kPa

5.2.3 Effect of feed temperature

The dependency of feed temperature on flux, reject temperature and reject pressure were studied by varying the temperature from 313K to 343K, for the fixed flowrate of 200L/h, feed concentration of 1g/L and absolute vacuum pressure of 7.3 kPa. The experimentally observed water flux is increasing linearly with increase in feed temperature as shown in Figure 26. The 2-fold flux increase obtained for 10K rise in feed temperature from 313K.

By increasing the feed temperature, net available sensible heat for water evaporation at membrane interface is also increased that leads to both increase in flux and the reject temperature, the non-linear behavior is observed for reject temperature. Since all the experiments with respect to temperature variation reported here are performed at feed flowrate 200 L/h, absolute vacuum pressure 7.3 kPa (0.073 bar) and absolute feed pressure 1.3 bar which is leading close to maximum Liquid Entry Pressure (LEP) 1.5 bar, therefore the observed reject pressure is zero.

Most of the literature reported experimental data for flux dependency with temperature for HF-VMD process concludes that the high non-linear relationship between flux and temperature. However, in this work linear behavior is observed, further, to explore the mass, heat and transport phenomena behind this behavior, the validated model is used to simulate the flux variation along the length. The cumulative flux till 0.1m length of the HF-VMD module is shown in Figure 27 and this concludes that when module length is reduced, the observed flux is highly non-linear with respect to increase in the feed temperature. This is mainly due to under-utilization of the HF module length, due to unavailability of sensible heat and low feed temperature when module length is greater than 0.5m as shown in Figure 28(a) and Figure 28(b) respectively. Therefore, while manufacturing the HF module estimating of module length for the given application is mandatory, i.e. the optimum length of the module will be function of maximum operating pressure, flow and temperature of the system, fiber diameter and LEP. To perform this design optimization the model proposed in this work can be used.

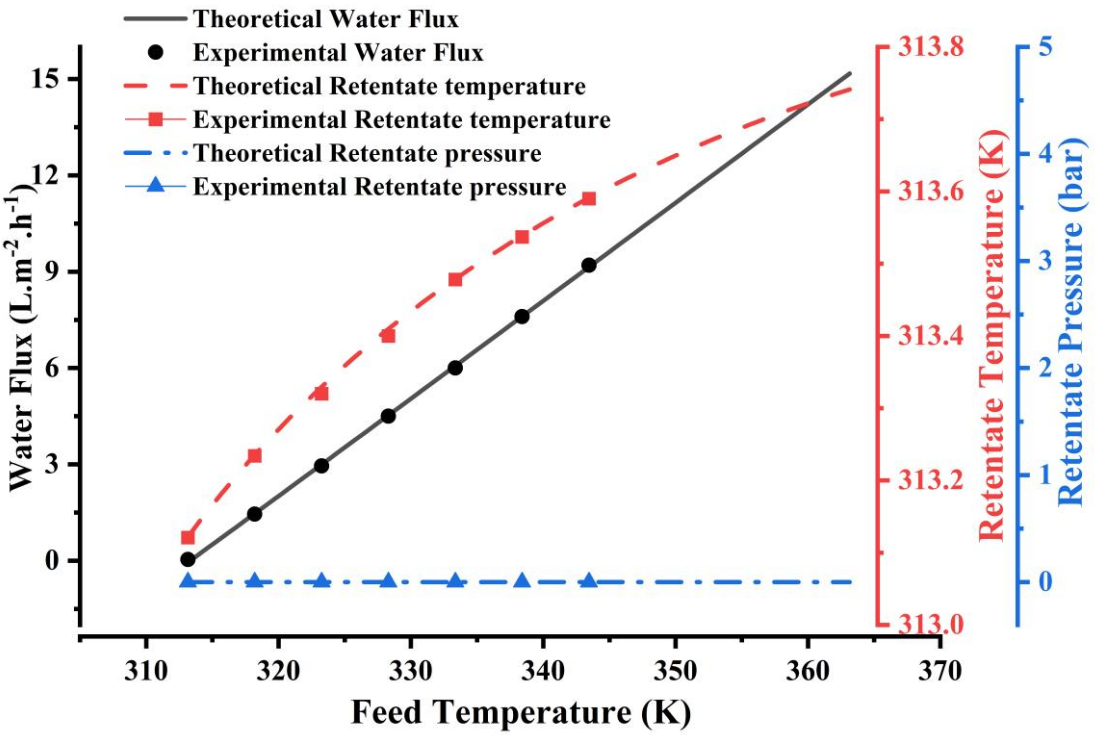

Figure 26: The effect of feed temperature on flux, reject temperature and reject pressure at the conditions: Feed flowrate 200 L/h, Salt concentration 1g/L and vacuum pressure 7.3 kPa

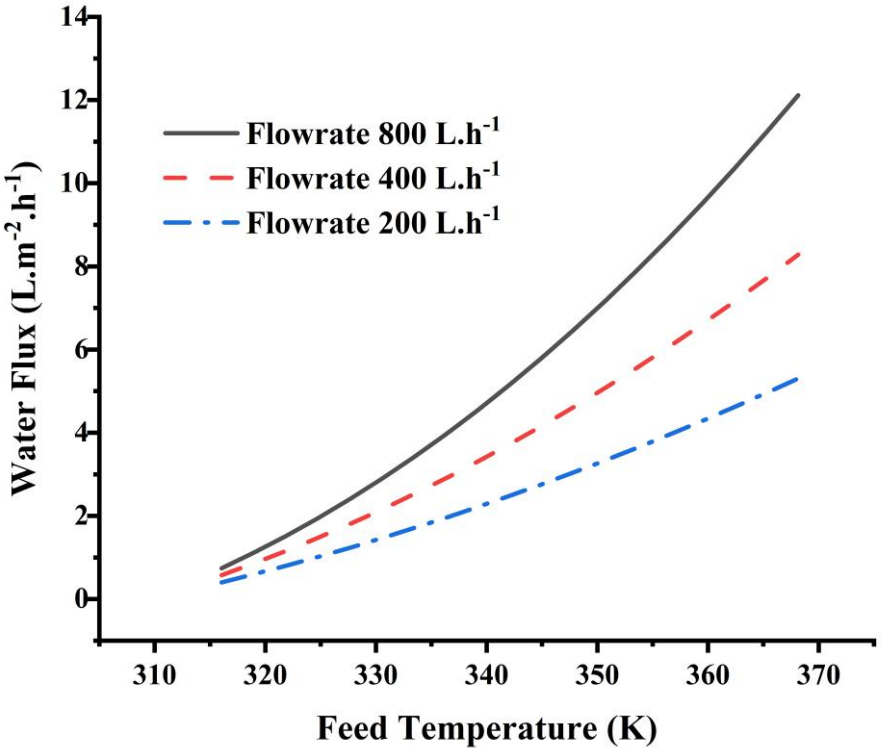

Figure 27: Flux behaviour upon decreasing the module length to 0.1m

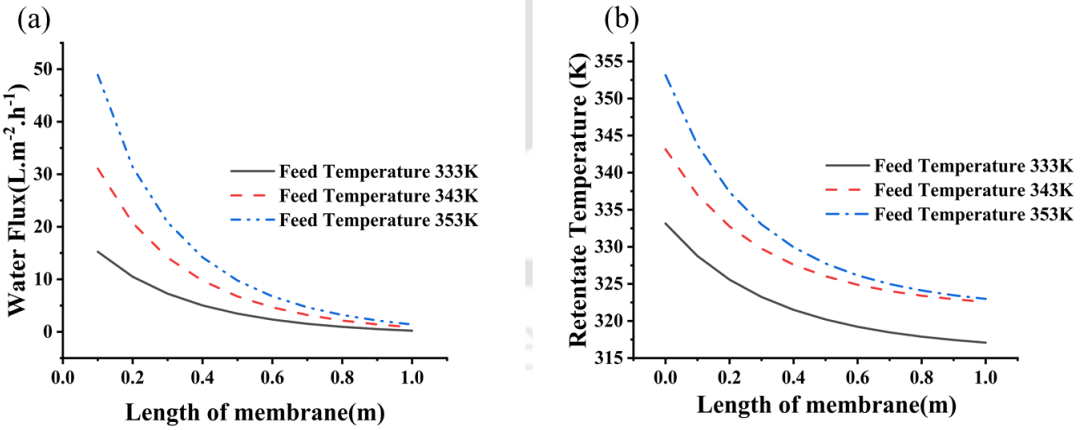

Figure 28: (a) Variation of flux and (b) reject temperature across the length of the membrane module

5.2.4 Effect of vacuum pressure

The dependency of vacuum pressure on flux, reject temperature and reject pressure were studied by varying the absolute vacuum pressure between 18.6 kPa to 7.3 kPa for the fixed temperature of 333K and flowrate of 200 L/h. The resulting trend as shown in Figure 29 that on decreasing absolute vacuum pressure the permeate flux increases non-linearly. Experiments had the limitations of LEP of 150 kPa (1.5 bar) at 30^{o}C, for operation around 333K it eventually decreases further. Hence the experiments were carefully conducted between 140 kPa (1.4 bar) pressure as feed and 7.3 kPa (0.073 bar) as vacuum for the safety operation of HF-VMD module. The change in the flux per unit vacuum pressure varies from 0.5 LMH/kPa to 1.5 LMH/kPa while varying absolute vacuum from 18.6 to 7.3kPa. Therefore, operating at lower vacuum pressure provides higher flux per unit vacuum pressure.

Further the energy consumption of vacuum pump is also expected to increase while operating at low vacuum pressure. The estimation of optimal vacuum pressure for a given application requires the formulation of objective function that combines flux and energy consumption with respect to vacuum pressure with the constraint from LEP, to avoid the intrusion of liquid in the pore (wetting of membrane pore) which is prevalent[139,140]. Since the studied downstream pressure is well below the liquid entry pressure (LEP) membrane performed at its full potential. As the downstream pressure decreases, the reject temperature is observed to be decreasing trend as more vapor is passing through the membrane, that leads to loss of sensible heat from vapor due to evaporation. The reject pressure observed to be close to zero at a higher flowrate of 200 L/h.

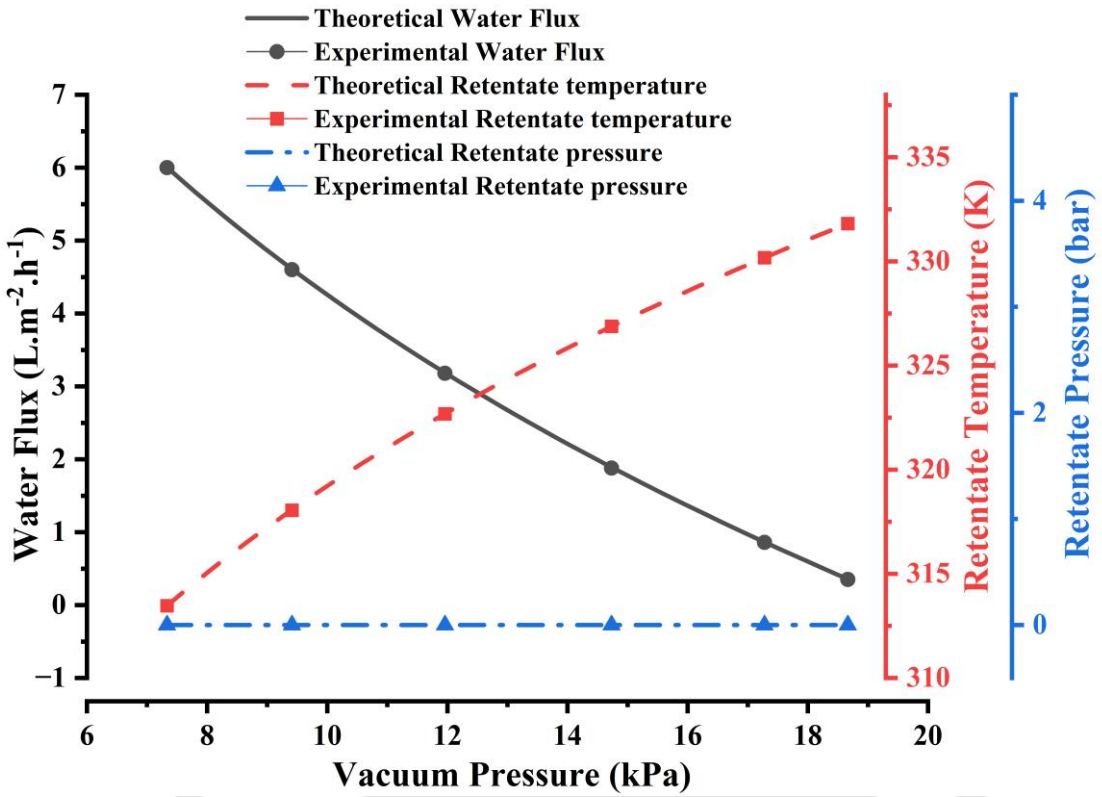

Figure 29: The effect of Vacuum pressure on flux, reject temperature and reject pressure at the conditions: Feed flowrate 200 L/h, Salt concentration 1g/L and feed temperature 333K

5.2.5 Effect of feed concentration

To study the effect of feed concentration on HF VMD module performance experimentally, the salt concentration varied from 5g/L to 35g/L of rock salt for the fixed feed temperature of 333K, feed flowrate 200 L/h and vacuum pressure of 7.3 kPa. The addition of solute is expected to increase the boiling point of the solution such that the evaporation rate decrease, and this phenomenon can be explained by Boiling point elevation (BPE) which decreases the vapor pressure of solution. In addition to the increase in boiling point, the CP phenomena will also increase the observed solute concentration on membrane surface. Both these effects will contribute to the decline in water flux while increasing salt concentration as shown in Figure *30*. Since the water flux is reduced the loss of sensible heat from the feed is also reduced such that increase in reject temperature is observed. Since these experiments are operated at maximum recommended feed flowrate the reject pressure is expected to be near to zero. Therefore, not much variation in reject pressure is observed.

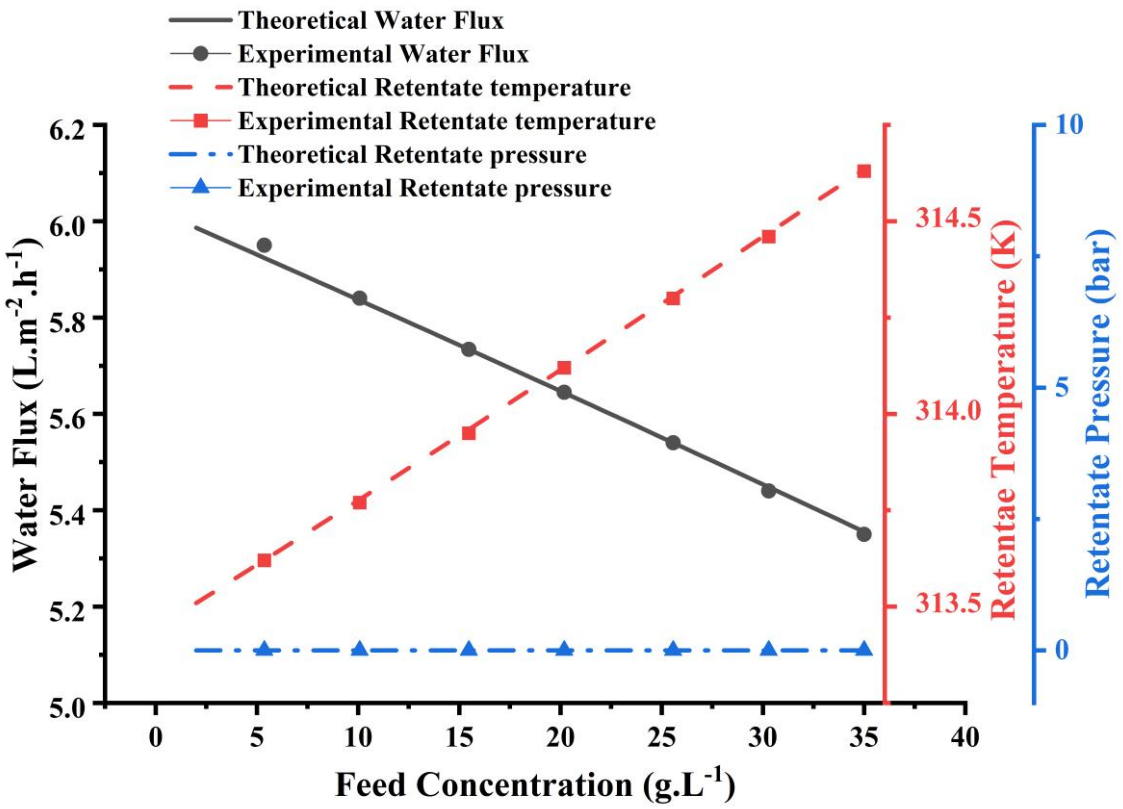

Figure 30: The effect of Feed concentration on flux, reject temperature and reject pressure at the conditions: Feed flowrate 200 L/h, Vacuum pressure 7.3 kPa and feed temperature 333K

Operation under near-saturation and supersaturation conditions inherently increases the risk of membrane wetting and fouling in membrane distillation, as elevated solute activity and concentration polarization can reduce the effective liquid entry pressure and promote pore intrusion. In the present study, a gradual decline in permeate flux was observed during extended operation at high concentration levels, indicating the onset of transport resistance associated with concentration polarization, fouling, or incipient crystallization at the membrane interface. Although no post-experimental membrane characterization was performed, the observed flux reduction is consistent with phenomena commonly reported during MD operation close to saturation limits. Detailed post-operation membrane analyses, such as SEM imaging and long-term fouling and cleaning studies, are recommended in future work to directly assess crystallization, fouling morphology, and wetting propensity under sustained supersaturation conditions.

Although the developed model captures the overall trends of the experimental data with good agreement, minor deviations between model predictions and experimental results were observed under certain operating conditions, particularly at higher feed concentrations and extended operating times. These discrepancies can be attributed to simplifying assumptions adopted in the model, including one-dimensional transport, constant membrane properties, and the use of average heat and mass transfer coefficients. In addition, localized concentration polarization, unsteady thermal effects, and the onset of fouling or incipient crystallization reflected experimentally by a gradual flux decline are not explicitly resolved in the current modelling framework. Measurement uncertainties associated with temperature, flow rate, and permeate flux determination may also contribute to the observed deviations. Despite these differences, the model successfully reproduces the dominant transport behaviour and provides reliable predictive capability for system performance within the investigated operating range.

5.2.6 Effect on concentration polarization

Further to understand, CP effect along the membrane module length, the parameters that correlates the concentration polarization is estimated through mathematical model that uses the film theory model. As shown in Figure 31(a), the feed flowrate is varied for feed concentration of 35g/L at the feed temperature of 343K and vacuum pressure of 20kPa and the corresponding CPC is presented. In Figure 31(b), feed flowrate is varied but for three different concentrations of 15,25 and 35g/L for the feed temperature of 343K and vacuum pressure of 20 kPa. CPC trend increases with increase in feed flowrate which is opposite to the pressure driven membrane separation process like Ultra Filtration (UF), Nano Filtration (NF) and RO. This can be explained by the following arguments

- According to the equation (2-15) the CPC is expected to increase with Jv and increase with increasing k. But in MD process increasing the feed flowrate contributes to higher flux as the heat transfer co-efficient increases inside the module and more sensible heat is available for vaporization of feed. This leads to higher vaporization compared to the increase in the overall mass transfer coefficient value for the fixed increase in feed flowrate.
- In VMD process, mass transport has less effect compared to heat transport which signifies that value of permeate flux is more as compared to the mass transfer co-efficient as shown in Figure 31(a). This resulted in CPC with increasing trend against

flowrate as shown in Figure 31(b). This study also indicates that VMD is dominated by heat transport.

- The solute concentration at the membrane's surface rises until it reaches a critical feed flow rate (625 L/h), after which it decreases as a result of saturation in the CPC above the Critical Flow rate for Nucleate Formation (CFNF), while the bulk feed concentration continues to grow along its length. Based on these findings, setting the feed flow rate to its critical value is advisable for achieving optimal nucleate formation close to the VMD membrane surface.

(a) (b)

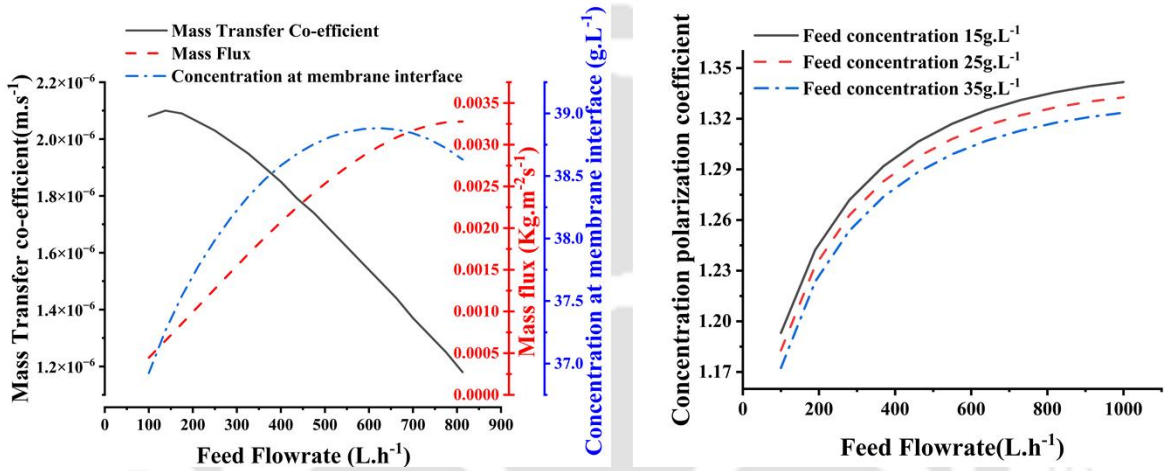

Figure 31: Concentration polarization effects of VMD

5.2.7 Effect on temperature polarization

The effect of temperature polarization is studied by varying the feed flowrate from 100-500L/h of the system for three different temperatures such as 338,343 and 348K of feed concentration 1g/L and vacuum pressure 20kPa shown in Figure 32 TPC is increasing, with increasing the feed flowrate and decreasing at higher temperature. This can be explained by the below explanations

- By increasing the feed temperature, higher flux is generated at the membrane interface that creates more difference between the temperature at the bulk and interface, favors TPC phenomenon.
- Operating at lower bulk temperature, membrane interface attains temperature closer to bulk temperature that leads TPC close to 1. Therefore, TPC can be minimized by operating the VMD system at higher flowrate and lower bulk temperature

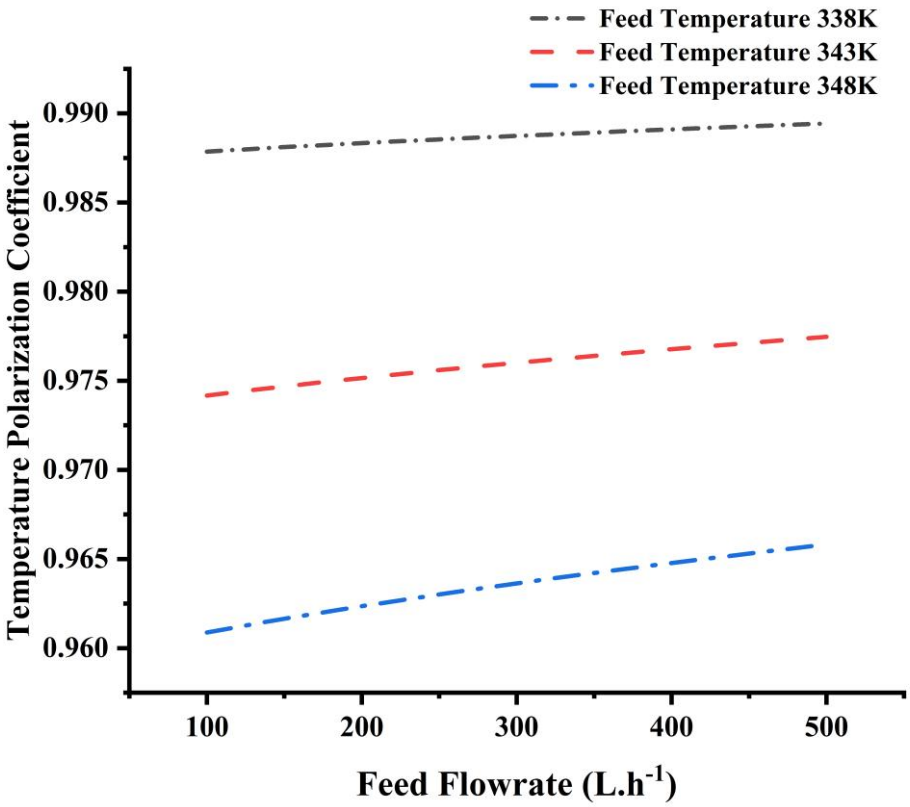

Figure 32: Effect of TPC upon varying feed flowrate

5.2.8 Validation of mathematical model with existing literature

To validate the mathematical model presented in this work, the model prediction is compared with experimental data reported in the literature for smaller HF VMD modules[51,57]. The validation was performed against two aspects: (1) the experimentally reported data and (2) the predictions of literature-reported mathematical models, specifically the lumped system models which do not incorporate distributed modeling approaches. Our model demonstrated excellent predictive capability for the literature experimental data, achieving an average error of 0.75%, compared to maximum errors of 3.5% in chang et. al model[57] and 1.67% in the Boan Li et al model[51]. Additionally, the maximum error in water flux predictions for our model was only 1.4%, further confirming its accuracy compared to the literature models. The performance of the model is also shown in Figure 33, to represent the predicted against experimental water flux value. The results show that the model presented in this work successfully predicts water flux data with an error margin below 1%, significantly outperforming the literature reported model. This highlights the importance of incorporating Knudsen and Poiseuille mechanisms in the membrane mass transport modeling for accurate predictions, even for shorter modules.

Moreover, as previously described, the literature-reported models such as Chang et al and Boan Li et al are expected to deviate significantly when the module length increases due to their limited capability in addressing distributed effects. The model that incorporates variation along the membrane length and mechanistic transport phenomena, effectively addresses this limitation, offering superior predictive accuracy for both smaller and longer module configurations.

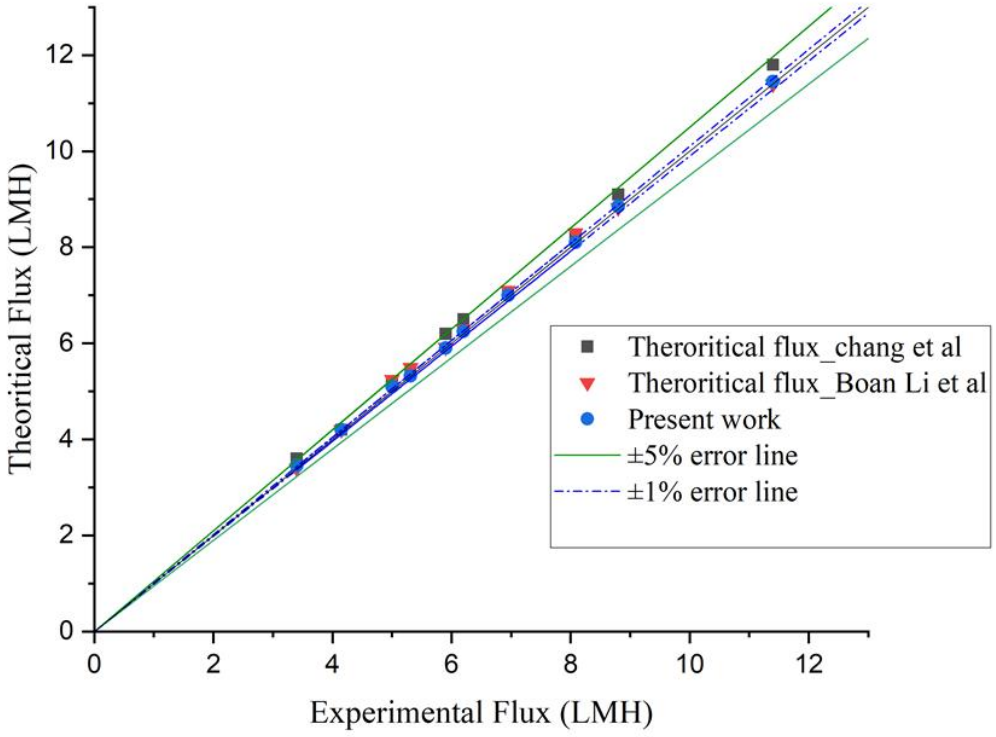

Figure 33: Comparison of existing literatures

5.3 Process Integration of VMD with TEHP device

As the TEHP model outlines, three parameters, namely electrical resistance (ohm), Seebeck coefficient (V/K), and thermal conductivity, must be estimated from experimental data by solving an error minimization optimization problem as shown in equation (3-24). Before estimating these parameters, the model is simulated by varying them to explore their range. This variation in different ranges involves calibrating and conducting three critical parameters. A sensitivity analysis is needed to assess how the model responds to parameter changes and is presented in Figure 34.

5.3.1 Electrical Resistance

The impact of electrical resistance on the performance parameters of a TEHP, such as hot and cold outlet temperatures, is shown in Figure 34(a). Typical thermal conductivity for TEHP material reported in the literature ranges from 0.1 to 5 W/m.K. As electrical resistance increases from 0.1 to 5 ohms for the inlet feed temperature of 303.15 K and flow rate of 5 L/h, the hot outlet temperature from TEHP decreases from 325 to 307.5 K, and cold outlet temperatures rise from 295 to 312.5 K. as electrical resistance in TEHP increases, the electrical current decreases, reducing the Peltier effect responsible for heat transfer. Consequently, less heat is transferred from the cold to the hot side, leading to a lower hot-side temperature. Simultaneously, the diminished cooling effect causes the cold side temperature to rise due to heat accumulation. Literature reported electrical resistance in the 0.152 to 3 ohms, respectively[141]

5.3.2 Seebeck Coefficient

The effect of the Seebeck coefficient on the performance parameters of a TEHP, such as hot and cold outlet temperatures, is shown in Figure 34(b). As the Seebeck coefficient increases from 0.0002 to 0.02 V/K for the inlet feed temperature of 303.15 K and flowrate of 5 L/h, the hot outlet temperature from TEHP increases from 312 K to 319 K and cold outlet temperatures rise from 308 K to 300 K. As the Seebeck coefficient increases, there is a significant upward trend in the hot outlet temperature. This rise is caused by the improved thermoelectric effect, where an increased Seebeck coefficient aids the conversion efficiency of electrical energy into thermal energy on the hot side of the TEHP module. Conversely, the cold outlet temperature shows a steady decline with rising α as more cooling heat effect produced by lifting more heat to the hot side of TEHP. Literature reported that the Seebeck coefficient ranged from 0.0002 to 0.02 V/K, respectively[142].

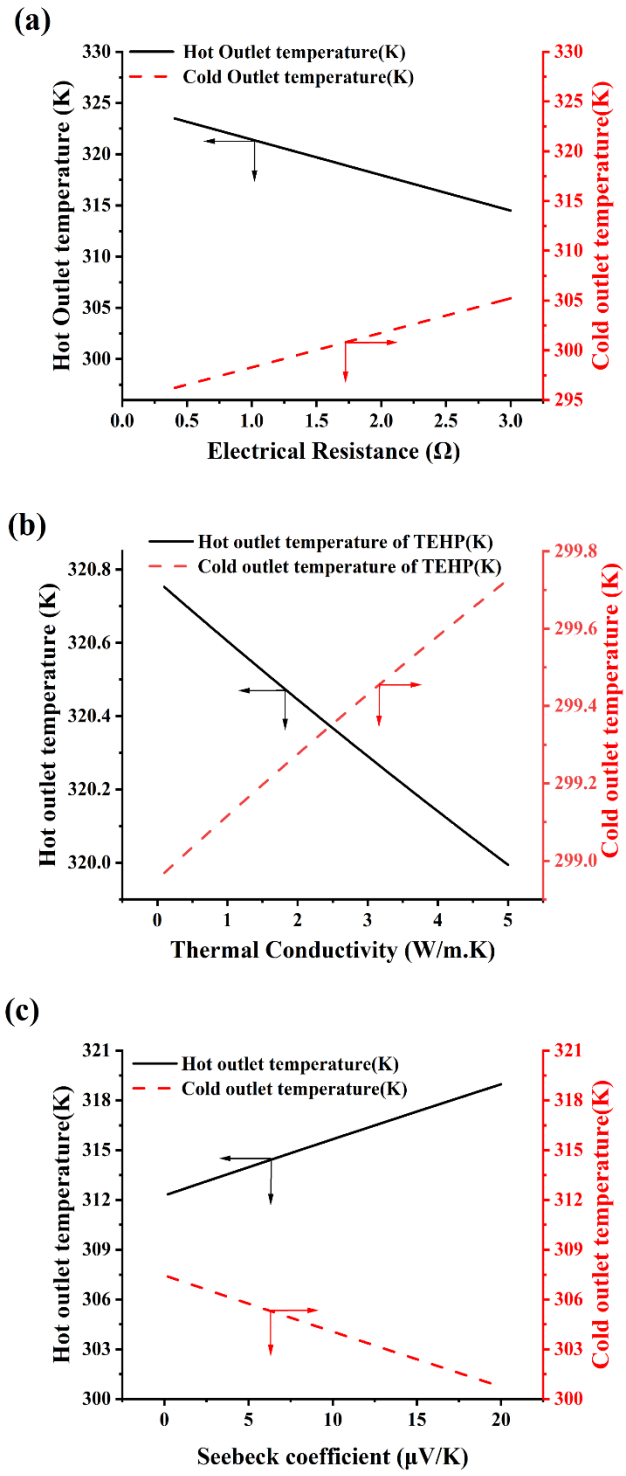

Figure 34: Effects of TEHP parameters on performance: (a) electrical resistance (Ω), (b) Seebeck coefficient (α, mV/K), and (c) thermal conductivity (k, W/m·K)

5.3.3 Thermal Conductivity

The effect of thermal conductivity on the performance parameters of a TEHP, such as hot and cold temperatures, is shown in Figure 34(c). As thermal conductivity increases from 0.1 to 5 W/mK for the inlet feed temperature of 303.15 K and flow rate of 5 L/h, the hot outlet temperature from TEHP decreases from 320.75 to 319.8 K, and cold outlet temperatures rise from 299 to 299.7 K. As thermal conductivity increases, there is a rise in cold temperature as more heat conduction loss to the cold side from the hot side is observed. This trend is attributed to enhanced heat conduction losses from the hot side to the cold side with increasing thermal conductivity. However, the decrease in the hot side temperature is less noticeable, indicating that the impact of thermal conductivity on the hot side is relatively minimal. Typical thermal conductivity for TEHP material ranged from 0.1 to 5 W/(m.K) .

The electrical resistance, Seebeck coefficient, and thermal conductivity bounds are selected based on the literature-reported values, as shown in Figure 34. Based on the bounds reported in the literature, this study was selected, and the model was calibrated to find the optimal parameters that minimize the relative error between the experiment and the simulation[141].

5.3.4 TEHP model validation and performance analysis

Model calibration and validation provide the accuracy of the TEHP model and establish an acceptable error tolerance. This validation process ensures the model's reliability and performance within the defined error margin.

The COP for the hot side of the TEHP module is evaluated by varying the flow rate at the cold side, and subsequently, the flow rate of the hot side is varied to assess the COP of the module's cold side, as shown in Figure 35. Experimental observation is well matched with the numerical simulation, with a relative error of less than 1%. At lower flow rates, i.e., 5 L/h, the system achieves a greater outlet temperature difference between the hot and the cold side of 47 K due to the longer interaction time between the fluid and the TEHP module. However, the heat transfer rate is limited because the mass flow rate is low, resulting in lower COP despite higher temperature differences. At higher flow rates, enhanced convective heat transfer improves temperature gradients, resulting in higher COP for both the hot and cold sides. Beyond this range, COP saturates because the TEHP module's thermal and electrical limitations dominate, and additional flow rate increases yield diminishing heat transfer gains.

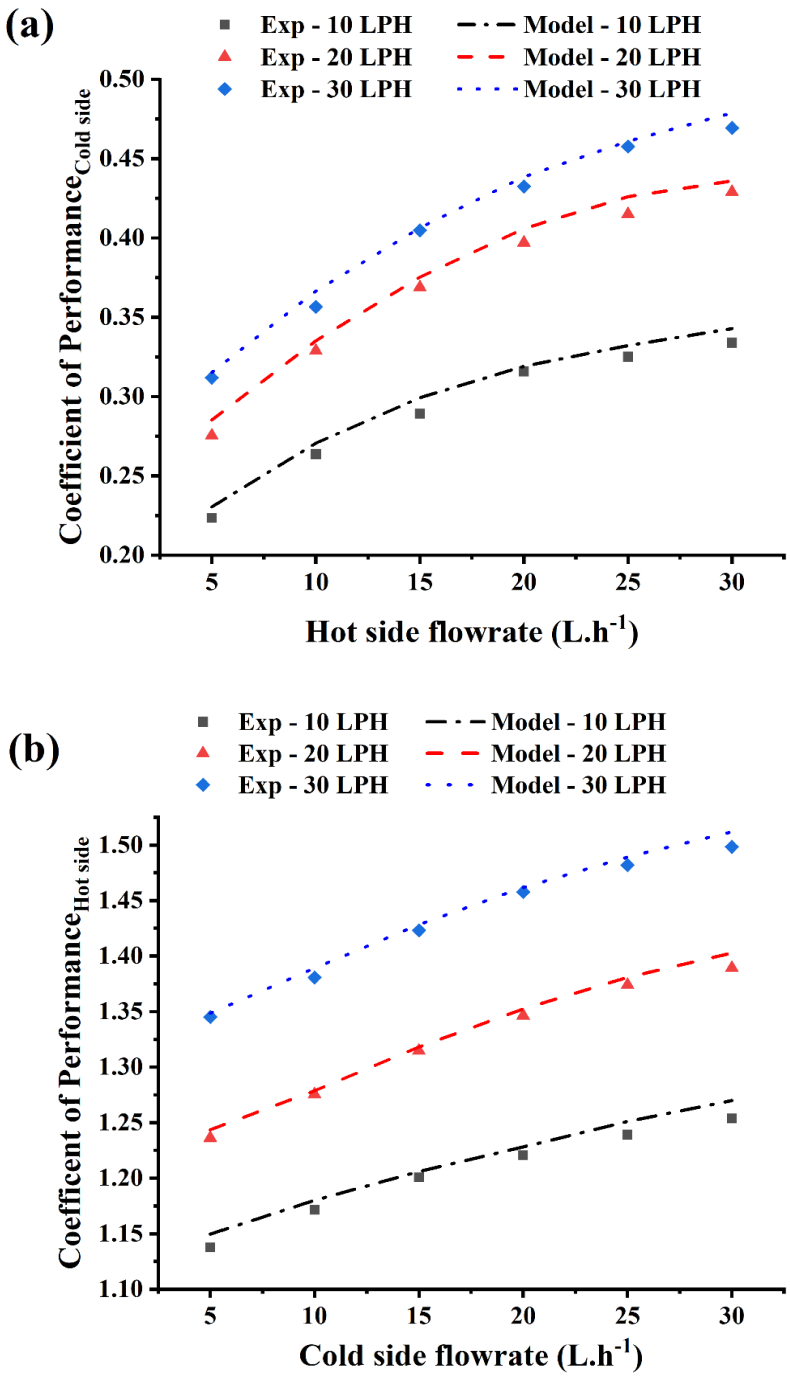

Figure 35: Model validation of the TEHP module performance on both the hot and cold sides

This study laid the foundation for scaling the number of modules for higher flowrate applications. It is also evident that the module's hot side performs two times better than the cold side, suitable for heating applications, and can be deployed for a capacity cooling system. In subsequent sections, a theoretical study on integrating the VMD system with TEHP will be attempted. The energy and cost analysis are further discussed to determine the potential scope of this integration.

The observed asymmetry between the hot-side and cold-side coefficients of performance COP_H and COP_C arises from irreversible losses within the thermoelectric heat pump, including Joule heating, thermal contact resistance, and heat leakage through the thermoelectric elements. While the hot side benefits from the combined contribution of Peltier heat and internally generated Joule heat, the cold side must overcome both parasitic heat conduction from the hot junction and electrical losses, resulting in a lower effective cooling capacity.

5.4 Flowsheet simulation of Integrated VMD with TEHP module

As shown in Figure 35 , COP for the hot side is more than 1, and cold side performance is less than 1. Therefore, the following two scenarios can occur while using TEHP with the HF-VMD module.

1. While maintaining sufficient heat requirements from the hot side, an additional cooling requirement has to be satisfied through an external condenser.
2. When a sufficient cooling load on vapor condensation is maintained, excess heat generated from the hot side of TEHP has to be dissipated. Further, to study both cases through simulation, two flow sheet models shown in Figure 36(a) and Figure 36(b) were simulated in this work.

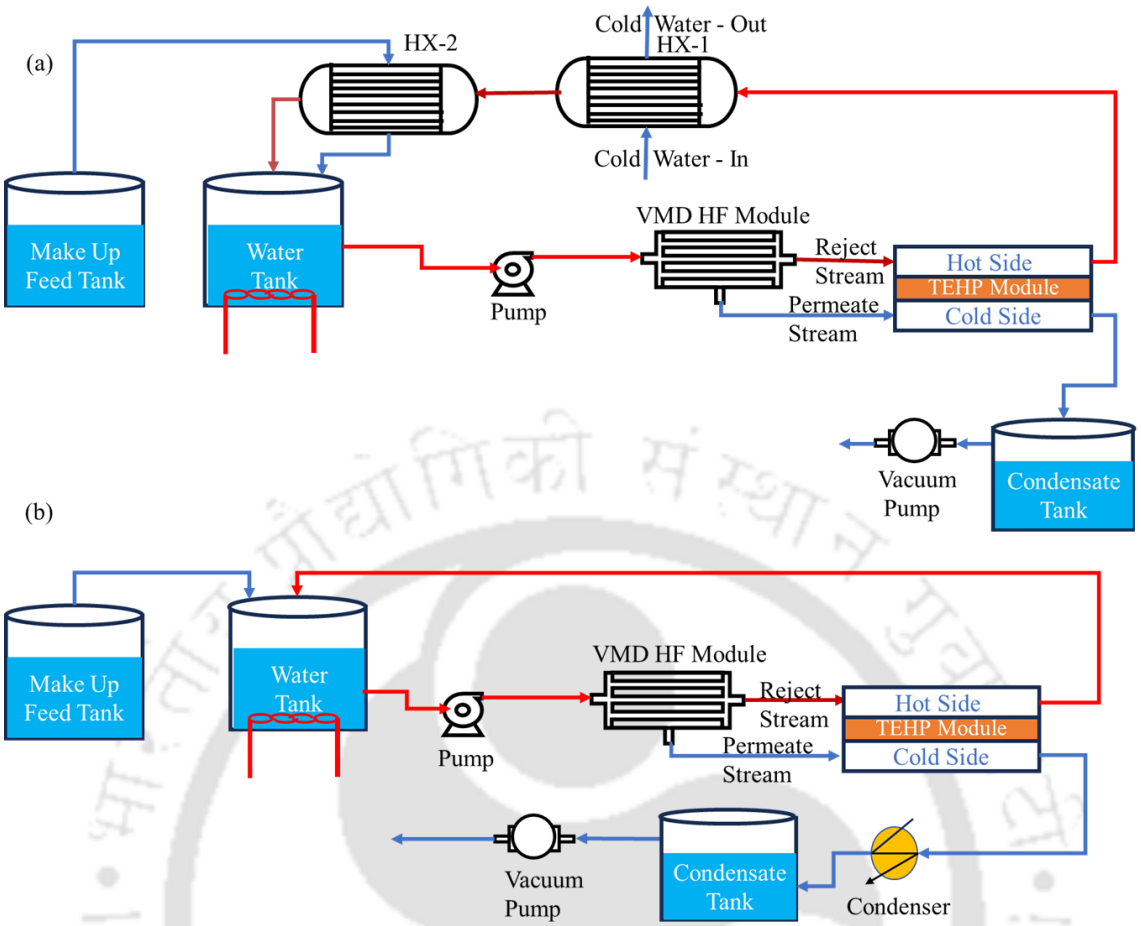

Figure 36: Two integration scenarios for TEHP with VMD: (a) TEHP provides a fixed heating load (with an external condenser handling excess cooling), and (b) TEHP provides a fixed cooling load (with excess hot-side heat dissipated)

Figure 36(a) shows the number of TEHP modules fixed for heating application, and Figure 36 (b) shows a similar number for fixed cooling. As the performance of the cooling side is comparatively lower in the module, an additional condenser is proposed for the fixed number of TEHP for the desired heating in flowsheet 1. Similarly, excess heat would be generated in the system for the fixed number of TEHP for the desired cooling, and an additional heat exchanger is proposed to remove the heat from the system.

5.4.1 Simulation of integrated TEHP with VMD for achieving the desired heating

In both cases of flow sheet simulation, the required number of TEHP modules will change depending on the TEHP load. The integrated model is simulated for varying vacuum pressure, feed flow rate, and feed temperature. The potential application of the TEHP system for lifting the reject temperature to the actual feed temperature and to condense the generated vapor from the VMD system, thereby evaluating the performance of the entire integrated module, was evaluated.

Table 17: Comparison of simulated performance of flowsheets

Parameter	Flowsheet 1	Flowsheet 2
Properties of the membrane	ID :1 mm OD :1.6 mm Porosity : 0.45 Length : 1000 mm Pore diameter : 2 μm	ID : 1 mm OD : 1.6 mm Porosity : 0.45 Length : 1000 mm Pore diameter : 2 μm
Properties of TEHP	Max operating temperature: 138 ˚C Max operating voltage: 12 V Max operating current: 6.4 A	Max operating temperature: 138 ˚C Max operating voltage: 12 V Max operating current: 6.4 A
Feed flowrate	650 L/h	650 L/h
Reject flowrate	632.7 L/h	632.7 L/h
Purge flowrate	63.27 L/h	63.27 L/h
Vacuum pressure	6 kPa	6 kPa
Product flowrate	17.3 L/h	17.3 L/h
Heat exchanger	1	2
COP	1.12 (Hot)	0.43 (Cold)
SEC	35 kW	11.2 kW

5.5 Performance analysis of the integrated system for varying operating conditions

5.5.1 Varying vacuum pressure

The dependency of vacuum pressure on reject stream temperature and permeate flowrate was simulated by varying the vacuum pressure from 6 to 28 kPa for the fixed flowrate of 650 L/h and feed temperature of 343.15 K, using the validated mathematical model of integrated VMD and TEHP as shown in Figure 37(a). A non-linear variation in reject temperature and permeate flow rate was observed while varying vacuum pressure, mainly due to the exponential relationship between vapor pressure and temperature.

The number of TEHP modules for the entire operational vacuum pressure increases as the permeate flow rate and reject stream temperature increase. In the event of high vacuum

operating conditions, such as 6 kPa, from this study, a total of 187 TEHP modules can preheat and restore the actual feed temperature of 343 K from the reject stream temperature of 321.24 K, consisting of a heating load of 16.1 kW. Similarly, for condensing, the vapor of flowrate 17.3 kg/h generated from the VMD system was 356 TEHP modules with a cooling load of 11.2 kW. From Figure 37(b), the COP of the hot side for the calculated number of TEHP modules was found to be 1.12, and for the cold side, it was found to be 0.43, respectively. The lower performance on the cooling side demands the use of a more significant number of TEHP modules; in that case, the excess heat generated on the hot side needs to be removed, and, in another aspect, excess cooling load need to be maintained for fixing the hot side demand of TEHP as shown in Figure 37(b).

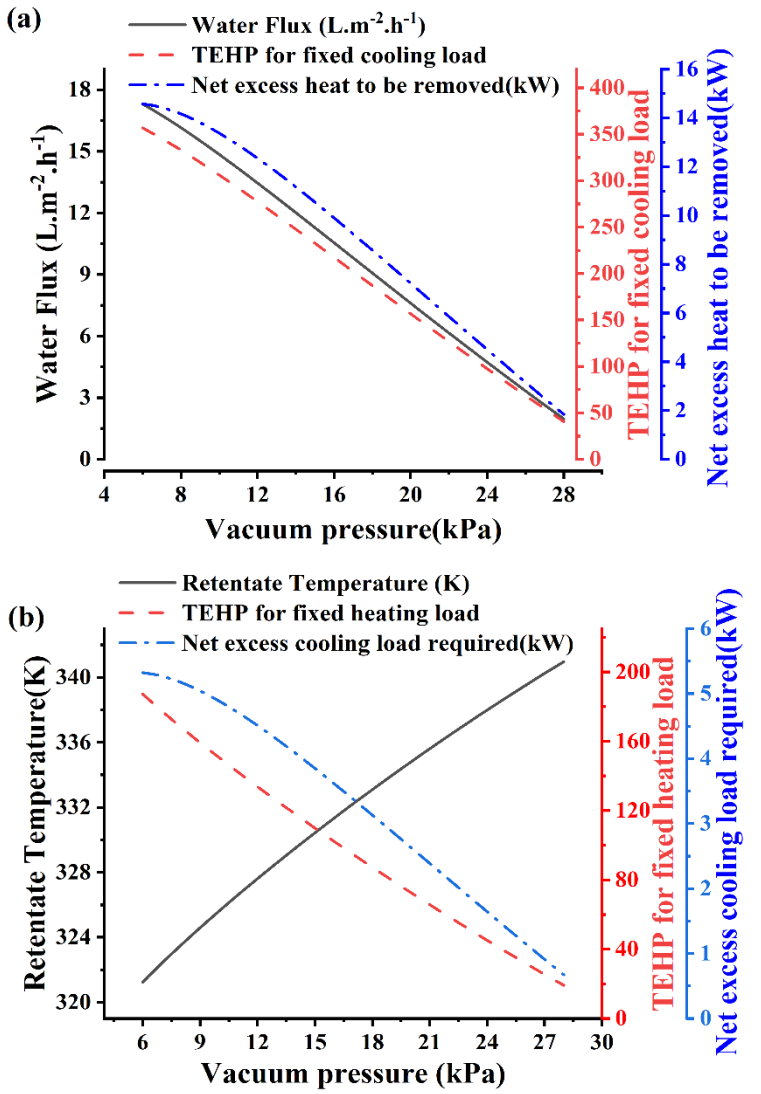

Figure 37: Performance analysis of integrated VMD and TEHP for varying vacuum pressure at fixed feed flow rate 650 LPH and feed temperature 343.15 K

5.5.2 Varying feed temperature

The dependency of feed temperature on reject stream temperature and permeate stream flowrate was studied by varying the feed temperature from 313.13 K to 368.13 K for the feed flowrate of 650 L/h and vacuum pressure of 6 kPa using the mathematical model as shown in Figure 38. Increasing feed temperature increases vapor pressure, which drives more vapor generation from the membrane interface and non-linearly increases the reject stream temperature. Vapor pressure increases exponentially with temperature following the Antoine equation; an increase in feed temperature of 5 K leads to a significant two-fold increase in the permeate stream. Also, higher feed temperature reduces the thermal boundary layer resistance near the membrane surface, which improves convective heat transfer. This phenomenon allows

more energy to be utilized for vaporization, which drives more vapor from the membrane interface to the permeate side. Upon increasing the feed temperature, the available heat energy after vaporization increases, significantly contributing to a non-linear increase in the reject stream temperature.

The number of TEHP modules along the operational range was also determined in this study. For the simulated feed temperature range of 313 to 368 K at the operating condition defined above, the maximum number of TEHP modules required for heating the maximum reject stream of 324.5 K for the feed temperature of 368 K found to be 359 K. This consists of heating load 31 kW to preheat the reject stream and recycle back to the feed tank as shown in Figure 38 (a). Similarly, for condensing the permeate vapor stream of flowrate 37.5 kg/h, the number of TEHP was 773, as shown in Figure 38(b). After fixing the number of TEHP modules, the coefficient of performance on both sides is evaluated. COP of the hot side for the calculated number of TEHP modules was found to be 1.12, and the cold side for TEHP modules was found to be 0.53, respectively. As the COP is almost twice as high on the hot side compared to the cold side of TEHP, a study on excess cooling required and the excess heat needed to be removed is also reported in Figure 38(b).

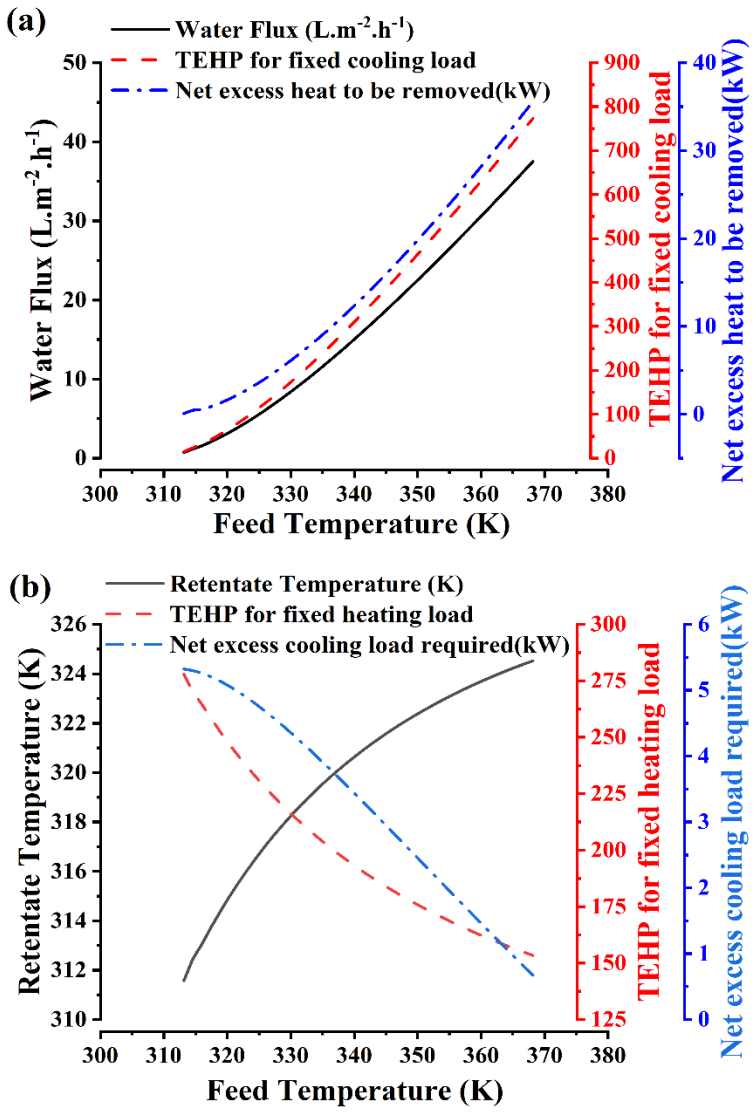

Figure 38: Performance analysis of integrated VMD and TEHP for varying feed temperature at fixed vacuum pressure 6kPa and feed flow rate 650 LPH

5.5.3 Varying feed flowrate

The dependency of feed flowrate on reject stream temperature and permeate flowrate was simulated by varying the feed flowrate from 100 to 1000 L/h for the fixed vacuum pressure of 6 kPa and feed temperature of 343.15 K, using the validated mathematical model, as shown in Figure 39(a). Increasing the feed flow rate non-linearly increases the reject temperature profile and the permeate flow rate linearly. As the feed flow rate considerably increases, the turbulence and mixing inside the VMD module contribute a linear increase in the permeate flow rate following the Darcy law equation, wherein more sensible heat is transferred from the feed side to the reject side, contributing a non-linear observation. The flux declines after the flow rate of 650 L/h due to the maximum velocity attained in the membrane module. At high flow rates,

the energy delivered by the feed may not be sufficient to maintain the required feed-side temperature. The cooling effect due to increased convective heat transfer could lower the membrane surface's average temperature, reducing the vapour transport's driving force.

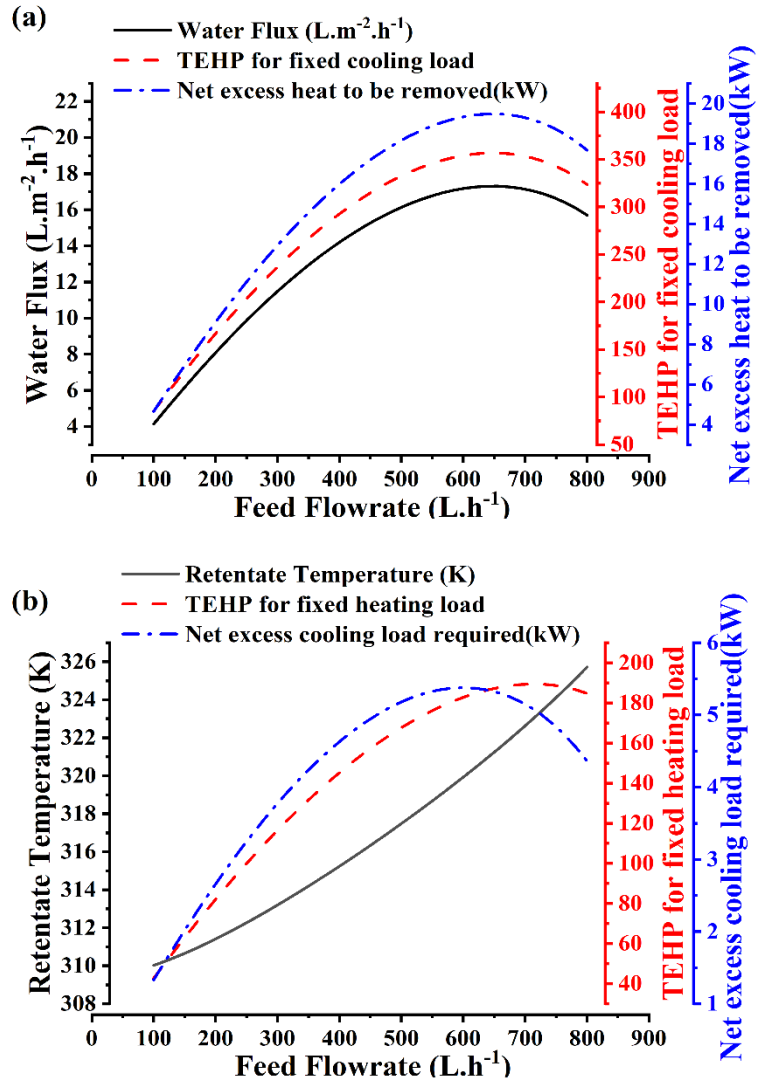

Figure 39: Performance analysis of integrated VMD and TEHP for varying feed flow rate at fixed vacuum pressure 6 kPa and feed temperature 343.15 K

The number of TEHP modules for the entire operational range of feed flow rate is determined. For optimal flowrate operations around 650 L/h, from this study, to restore the actual feed temperature of 343.15 K from the reject stream temperature of 321.1 K, a total heat load demand of 16 kW has been calculated. This heating energy can be achieved by integrating around 187 TEHP modules with the VMD system. On the other hand, condensing the permeate vapor of 17.3 kg/h generated from the VMD system requires the cooling load demand of 11.2 kW of energy; this can be achieved by integrating around 356 TEHP modules. The COP of the

hot and cold sides of the TEHP module was calculated to be 1.1 and 0.43, respectively. Further, an energy analysis of excess heat to be removed and the excess cooling required upon integrating either fixed TEHP for hot and cold side demand is shown in Figure 39(b). As the available heat energy on the hot side is almost twice that on the cold side, TEHP integration needs to be optimally evaluated based on this study.

5.5.4 Optimization of process variables

Based on the simulation results of the integrated VMD-TEHP system, as presented in Figure 37, Figure 38 and Figure 39, it is evident that the effects of key operational parameters, namely feed flow rate, feed temperature, and vacuum pressure, on the permeate flow rate are highly non-linear and strongly interdependent. These interactions highlight the complexity of identifying optimal operating conditions purely through parametric variation.

To facilitate an intuitive understanding of these complex relationships, the 3D surface plot for permeate flow rate against combinations of two variables at a time while fixing the third at its respective optimal condition derived from earlier parametric studies. Specifically, the following two-dimensional plots were analyzed: (i) permeate flow rate versus feed temperature and vacuum pressure (Figure 40a), (ii) permeate flow rate versus feed flow rate and feed temperature (Figure 40b), and (iii) permeate flow rate versus feed flow rate and vacuum pressure (Figure 40c).

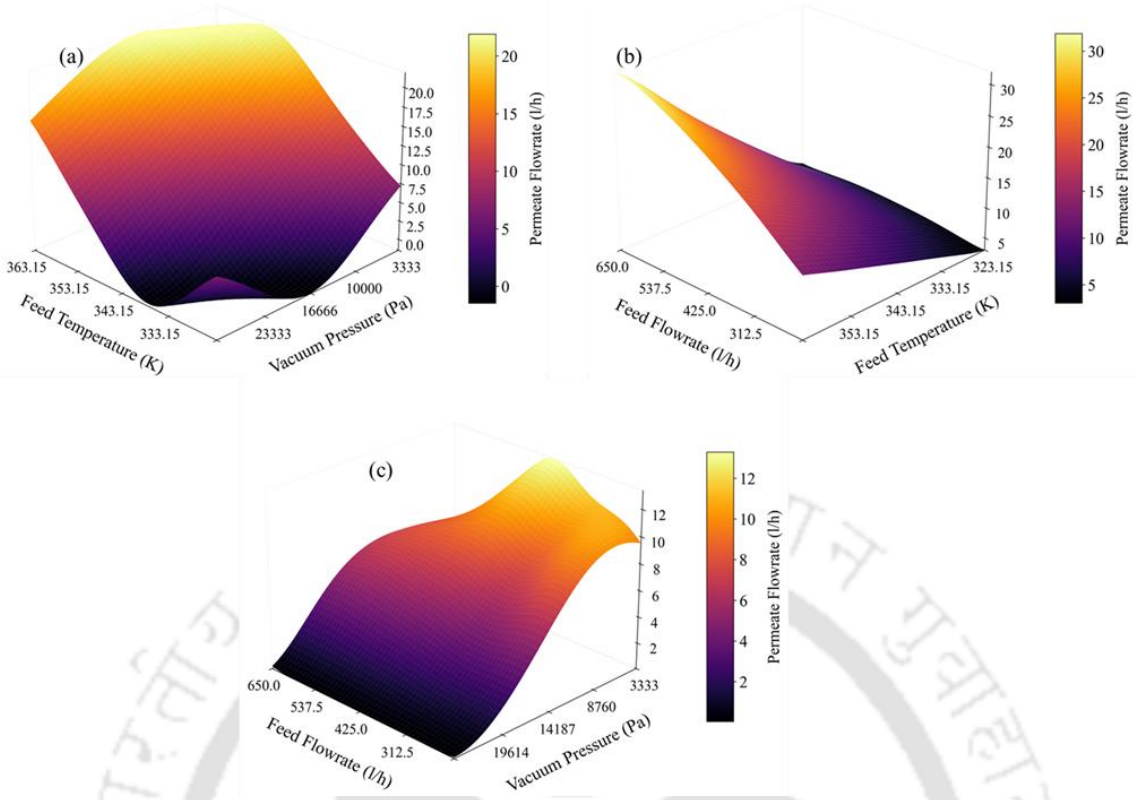

Figure 40: Simulation-Based Optimization of VMD Operating Parameters: 3D Surface Analysis of Feed Temperature, Flowrate, and Vacuum Pressure Effects on Permeate Flux

In all the 3D surface plots in Figure 40, one parameter was held constant at its inferred optimum, which was identified through individual variation studies. For instance, while varying feed temperature and vacuum pressure, the feed flow rate was fixed at 650 L/h (the condition determined to maximize permeate output in Figure 39). Similarly, the remaining plots follow this structure to isolate the pairwise interactions.

The resulting surfaces in Figure 40 (subfigures a–c) demonstrate that permeate flow rate increases non-linearly with rising feed temperature and feed flow rate. Specifically, combinations of high feed temperature, high feed flow rate, and low vacuum pressure with high feed temperature exhibit significant increases in permeate flow. However, beyond a certain threshold, further reduction leads to an asymptotic decay in permeate flow enhancement with respect to vacuum pressure. This behavior indicates diminishing returns, likely due to the exponential relationship between vacuum level and vapor pressure as described by the equation (2-11).

Of particular importance is the observation that feed temperature has a more pronounced effect on permeate production at lower vacuum levels. In comparison, at higher vacuum levels, the

increase in permeate flow becomes less significant. Similarly, the interaction between feed flow rate and vacuum pressure reveals a peak beyond which higher flow rates do not contribute meaningfully. It may even reduce membrane surface temperature due to convective cooling, reducing the driving force.

These non-linear behaviors underscore the necessity of adopting a formal optimization approach in future studies. A multi-variable constrained optimization framework is required to simultaneously determine the optimal feed flow rate, feed temperature, and vacuum pressure to maximize permeate productivity while minimizing SEC. Such a formulation would also allow trade-off analysis between energy cost and water yield, facilitating techno-economic decisions.

At present, this study focuses only on graphical optimization through simulation, serving as a precursor to more rigorous optimization work. Based on the trends observed in Figure 40, it can be concluded that (i) reducing vacuum pressure up to an optimal limit and increasing feed flow rate enhances permeate flux, (ii) increasing both feed flow rate and feed temperature further promotes permeate flow, and (iii) excessive vacuum reduction leads to an asymptotic decline in performance gains.

Given the system's complexity, identifying a global optimum through analytical methods remains a subject for future research. Nevertheless, for the techno-economic analysis presented in the subsequent section, the following operational conditions are fixed based on the above findings: feed flow rate at 650 L/h, feed temperature at 343.15 K, and vacuum pressure at 6 kPa.

5.5.5 Limitation of TEHP-MD and scale-up feasibility

TEHP-MD systems face clear practical limits that likely preclude their use in large-scale desalination. The main limitation is the low COP of TE modules, which leads to disproportionately high energy usage per volume of water. Even at lab scale, achieving just 5-30 L/h of distillate can demand kilowatts of power input. Scaling to, say, 1 m^3/h (~1000 L/h) would require hundreds of TE modules and an impractically large power supply. Unlike mechanical compressors, TE devices do not benefit from economies of scale in the thermodynamic sense, as adding more modules in parallel increases output linearly. Still, the overall efficiency remains low, so energy consumption and OPEX skyrocket. Moreover, large arrays of TE modules introduce heat transfer challenges like removing waste heat from many

small hot/cold junctions evenly, and reliability concerns like each module adding a potential failure point.

For these reasons, researchers consider TEHP-MD suitable mainly for small, portable, or emergency desalination units where simplicity (solid-state operation) is valued over efficiency. The practical implication is that TEHP-MD is unsuited for industrial-scale deployment beyond ~30 L/h, its role will remain in small-scale applications unless significant advances in thermoelectric materials dramatically raise COP. Meanwhile, MD-HP hybrids might serve medium scales, and MD-MVC hybrids target large installations or ZLD systems.

5.5.6 Potential Application

The integration of TEHP into the VMD system not only reduces operational costs but also increases the potential applications of this technology. When VMD systems are paired with TEHP, they can negate the necessity to separately reheat the reject stream and cool the permeate, resulting in substantial cost savings and enhanced energy efficiency. This new configuration is particularly advantageous in applications requiring ultra-pure water at low flow rates, typically less than 10 L/h, where traditional methods may be less efficient or too costly.

Potential applications of this optimized VMD system include dialysis, where ultra-pure water is crucial for patient safety and effective treatment. Additionally, in space applications, the compact and efficient design of TEHP-VMD systems makes them ideal for water purification in spacecraft. Another relevant application is water purification on ships or cruises, where consistent production of high-quality water is essential for both operational needs and the well-being of passengers and crew. The adaptability and cost-effectiveness of TEHP-integrated VMD systems position them as a promising solution in various fields requiring pure water and low-volume outputs, addressing the demand for efficient, compact, and reliable water purification technologies

5.6 Process integration of VMD with Heat exchanger

A standalone heat exchanger was initially integrated into the VMD system as shown in Figure 41 to facilitate the latent heat recovery. However, the maximum recoverbale heat energy from this integration was limited to 0.1 kW based on the overall mass balance of the sytem, as a consequence steam exiting at the HX predominantly as uncondensed vapor. An additional heat input of 16.5 kW was required for the system for continuous heating of the feed, while an

excess cooling load of 11.1 kW had to be managed using an auxiliary chiller unit. The performance analysis of the sytem for various feed flowrate, feed temperature and vacuum pressure with the corresponding excess heat need to be removed from the system is shown in the Figure 42.

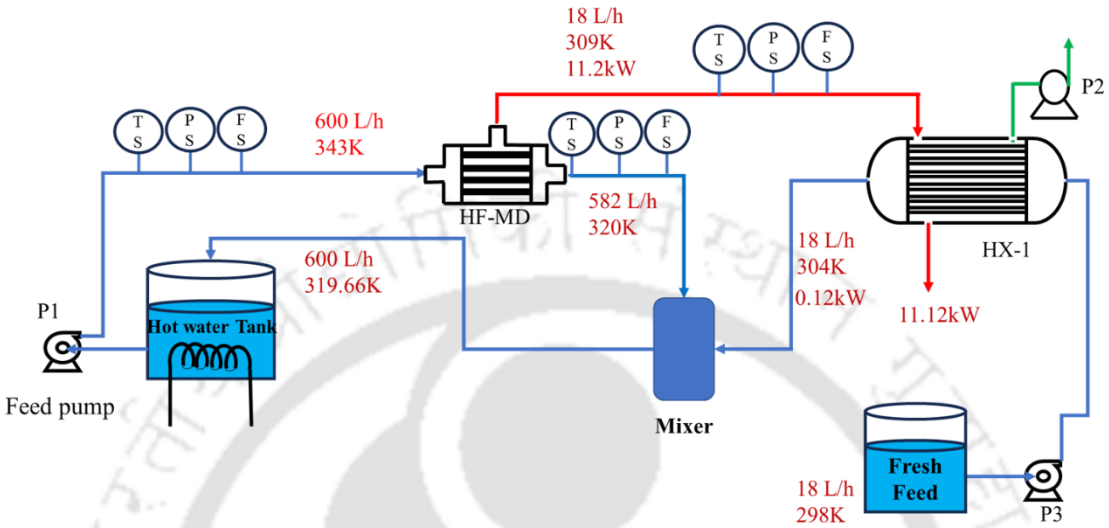

Figure 41: Process flowsheet of VMD system integrated with HX

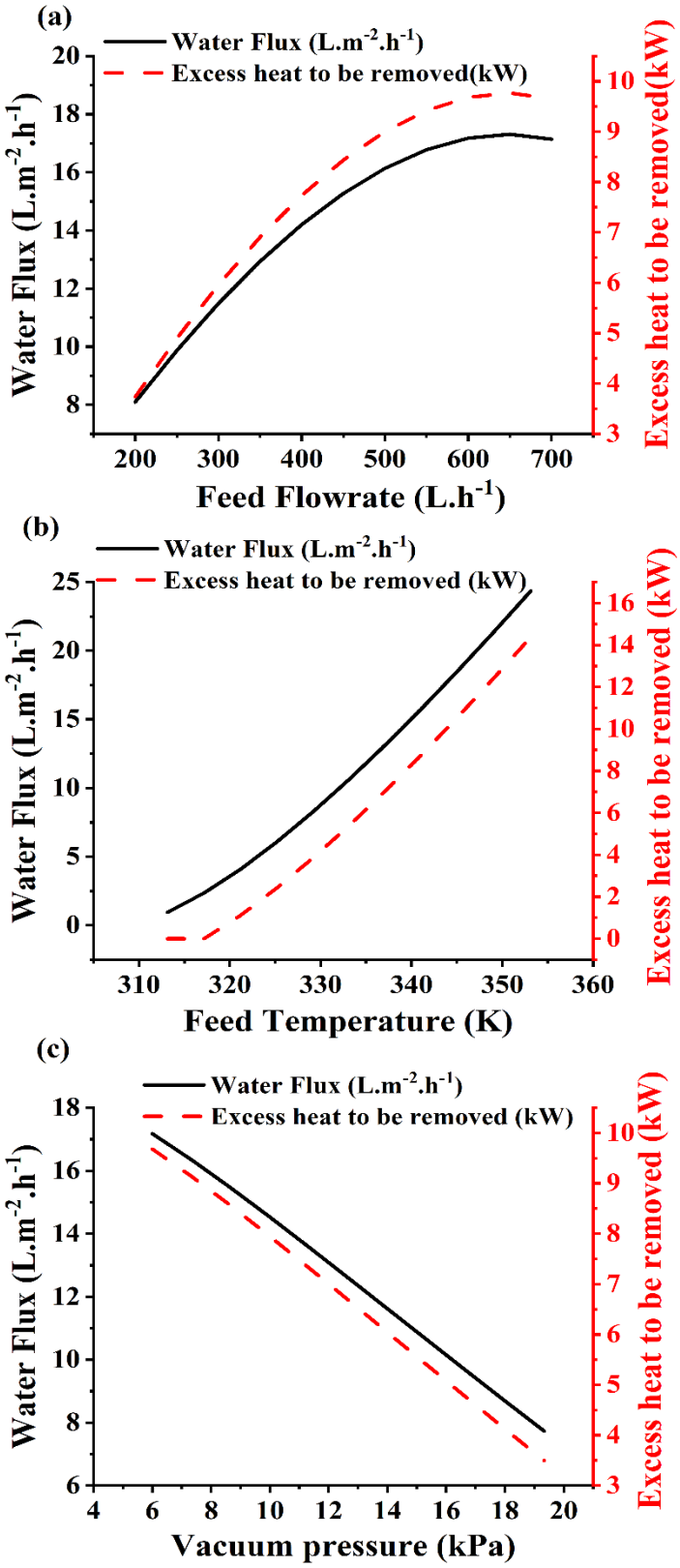

Figure 42: Performance and energy analysis of VMD by integrating with HX (a) Varying the feed flowrate (b) Varying the feed temperature (c) Varying the vacuum pressure

5.7 Process integration of VMD with Vapor compressor

To enhance system performance and improve energy recovery, VMD is integrated with VC and HX. This integration allowed for an increase in permeate vapor temperature and pressure from VMD, the compression ratio fixed as 2 and the hot stream temperature of 373K is achieved through this integrated as shown in Figure 43 thereby the latent heat of the vapor increases. To maintain the mass balance of the system, the maximum recoverable heat found to be 1.52 kW, therefore the excess heat of 9.68kW need to be removed as excess heat, although the vapor continued to leave as uncondensed. An additional heat input of 15 kW was required for the system for continuous heating of the feed, while an excess cooling load of 9.68 kW had to be managed using an auxiliary chiller unit. The detailed excess energy need to be removed for varying the feed flowrate, feed temperature and vacuum pressure from the VMD is shown in the Figure 44.

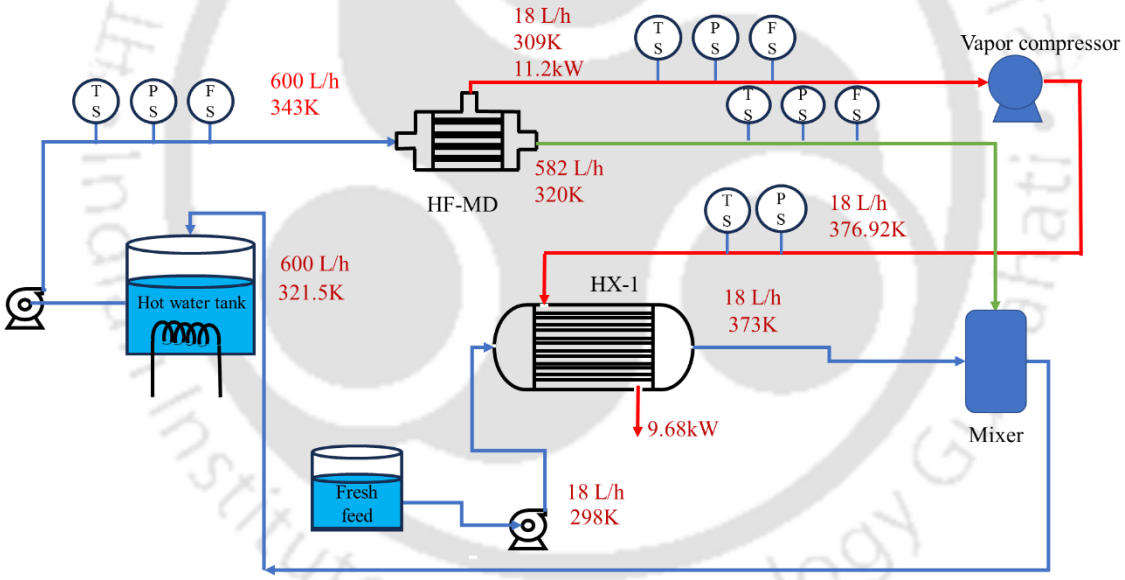

Figure 43: Process integration of VMD with VC and HX

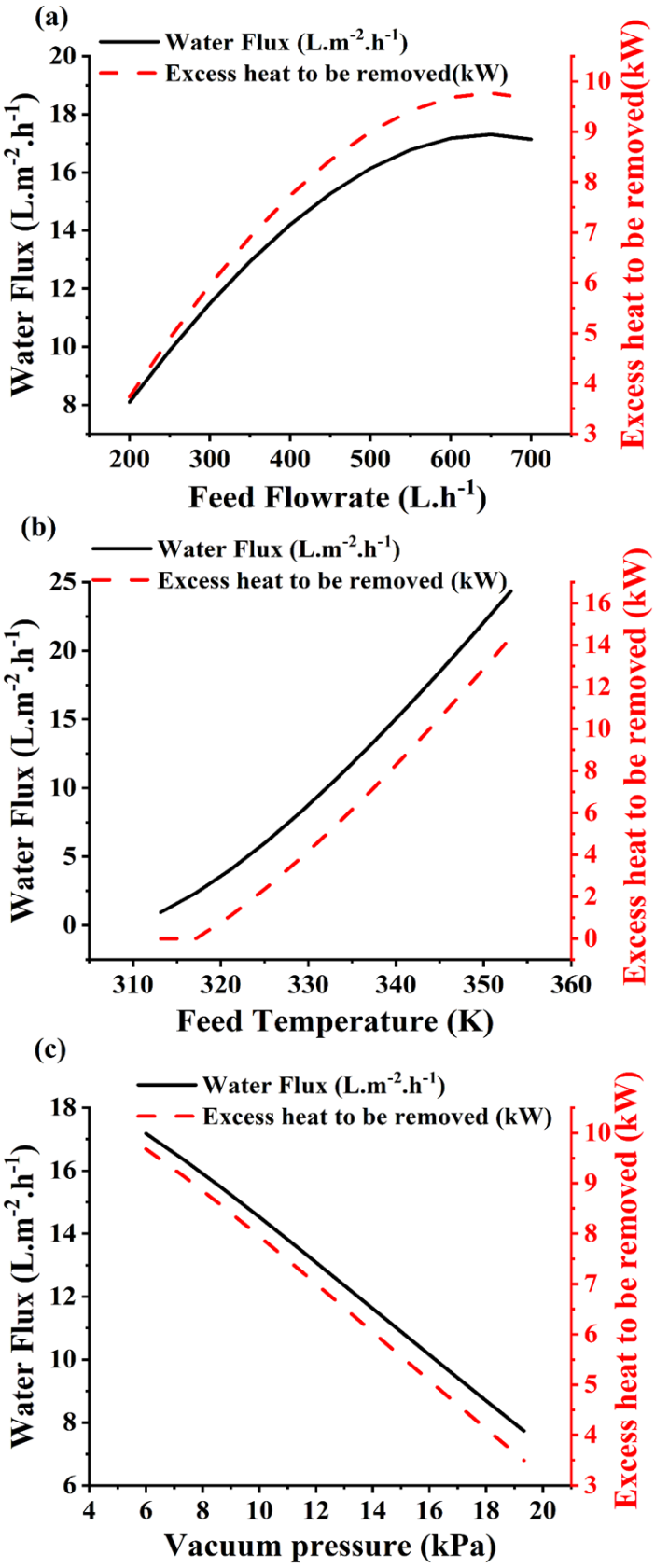

Figure 44: Performance and energy analysis of VMD by integrating with VC and HX (a) Varying the feed flowrate (b) Varying the feed temperature (c) Varying the vacuum pressure

5.8 Process integration of VMD with Heat pump

To establish both the thermal and cooling energy requirements efficiently, a HP system was proposed to integrate with VMD and the overall system was simulated. Refrigerant R314a was selected due to its favourable thermophysical properties for the desired application. Vapor condensation modelled on the evaporator side, while the reject stream was simultaneously heated on the condenser side. Performance evaluation indicated that the COP of the hot side is higher that of the cold side, resulting in an excess heat output of 4.5 kW, which was subsequently dissipated through an external heat exchanger to maintain system steady operation. The state of refrigerant at the each unit operation is shown in the Figure 45.

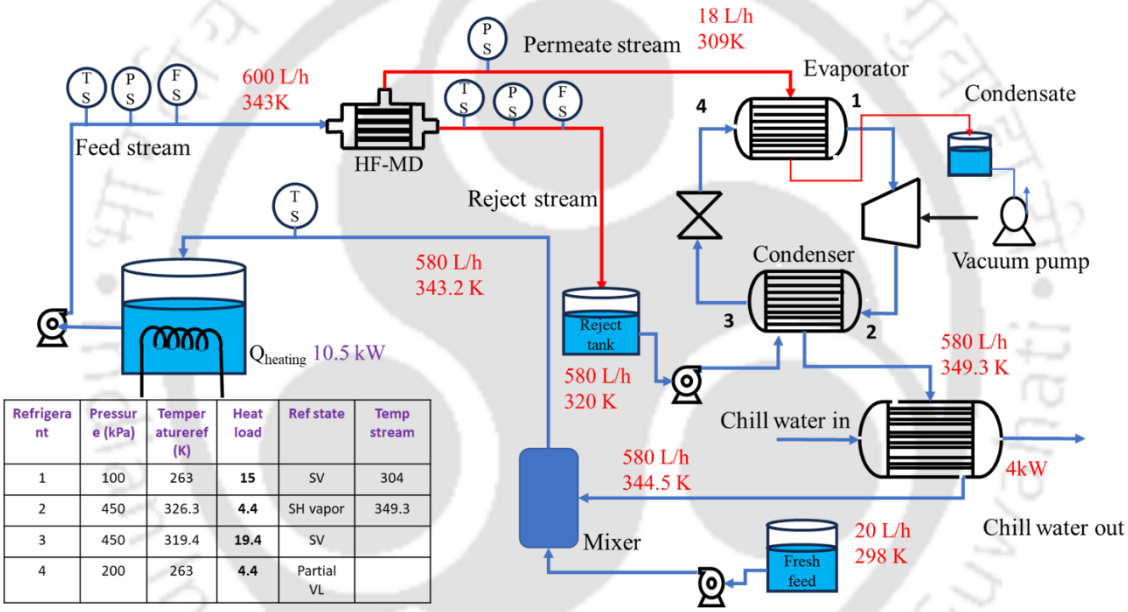

Refrigerant	Pressure (kPa)	Temperatureref (K)	Heat load	Ref state	Temp stream
1	100	263	**15**	SV	304
2	450	326.3	**4.4**	SH vapor	349.3
3	450	319.4	**19.4**	SV	
4	200	263	**4.4**	Partial VL	

Figure 45: Process integration of VMD system with HP

The system was initially operated at a feed flowrate of 600 L/h, generating 18 kg/h of vapor and 582 kg/h of reject solution, with a heating requirement to raise feedwater from 298 K to 343 K. During startup, the system exhibited a low GOR of 0.36 and a high STEC of 1,490 kWh/m³, due to high thermal input and limited vapor production. Once equilibrium was reached at 320 K, GOR improved to 0.73 and STEC decreased accordingly. The detailed performance analysis is explained in the below section

5.8.1 Energy performance analysis of HF-VMD integrated with HP for varying feed flowrate

Feed flowrate of the system increased from 100-650L/h to study the energy metrics such as GOR and STEC respectively. Upon increasing the feed flowrate, the reject temperature increases non-linearly as shown in Figure 23 . Therefore the amount of energy required for bringing back to the steady state varies non-linearly, this had an impact on the GOR and STEC as shown in Figure 46(a).

This study reveals a unique behaviour in the system that upto 245L/h, GOR increases from 0.816 to 0.8337 and STEC decreases from 873 kWh/m³ to 8546 kWh/m³**.** This indicates an improvement in thermal efficiency with increasing feed flowrate. The enhancement is attributed to more effective utilization of thermal energy due to improved turbulence and convective heat transfer on the feed side, which promotes vapor transport across the membrane. However, after this critical flowrate, the trend is reversed STEC begins to rise gradually from 0.8546 to 0.9126 kWh/m³, and GOR decreases slightly from 0.8337 to 0.7808. This decrease in performance indicates the thermal efficiency has declined after this critical flowrate, i.e. the heat load required to bring back the system to steady state to 343.K with th corresponding flowrate is controlling over the mass of vapor generated in the system. In other words, the mass flowrate of reject stream and reject temperature increases non-linearly upon increasing the feed flowrate.

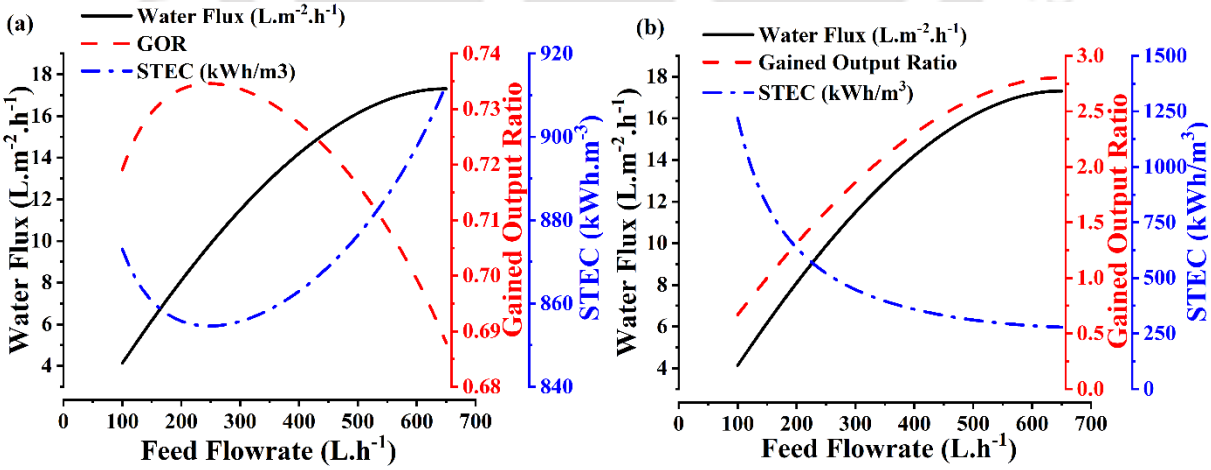

Figure 46: The effect of feed flowrate(L/h) on permeate flowrate, STEC and GOR at the operating conditions: Temperature 343K, Concentration 1 g/L, Vacuum Pressure 6 kPa

To improve the energy efficiency of the system, HP is integrated with the HF-VMD, and the compressor load is fixed as 4.4kW as discussed in the section 5.8. Upon integrating, the energy effieciency of the system is significantly improved from the maximum GOR of 0.83 without

HP to 2.81 and the STEC decreased from 912.57 kWh/m³ to 278.55 kWh/m³ respectively. HP integration has substantially decreased around 70% of the energy requirement highlighting its strong potential in improving overall process efficiency and sustainability.

5.8.2 Energy performance analysis of HF-VMD integrated with HP for varying vacuum pressure

Vacuum pressure of the system varied from 6kPa to 20kPa to analyse the energy metrics such as GOR and STEC respectively. Upon decreasing the vacuum pressure, the reject temperature increases non-linearly in accordance with antoine equation as shown in equation (2-11). Therefore the amount of energy required for bringing back to the steady state varies non-linearly, and the impact on GOR and STEC metrics as shown in Figure 47(a).

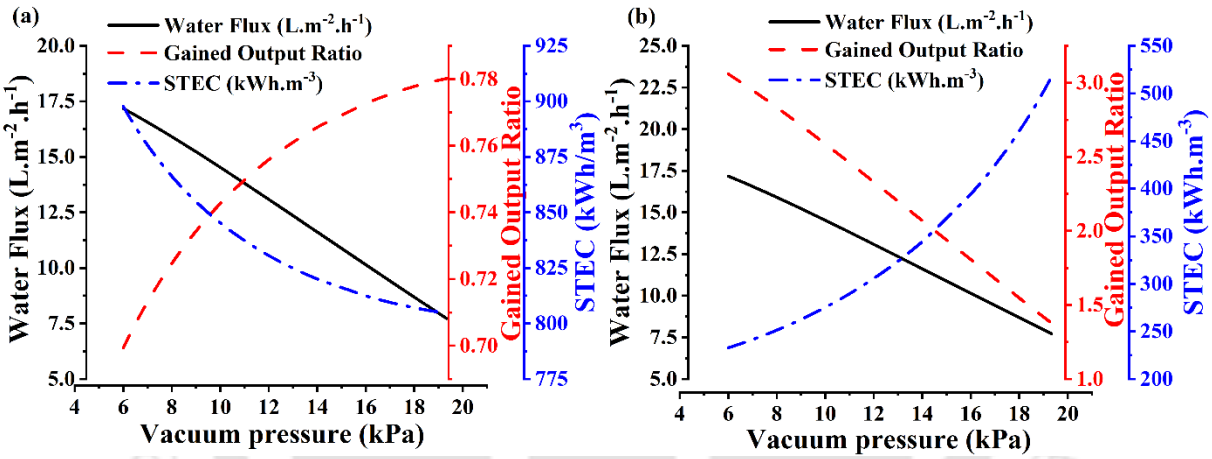

Figure 47: The effect of Vacuum pressure(kPa) on permeate flowrate, GOR and STEC at the operating conditions: Temperature 343K, Concentration 1 g/L, Feed flowrate 600L/h

The stand alone HF-VMD system operating at lower vacuum pressure, contributes greater driving force resulted in enhanced permeate flow. However, the temperature drop between feed and reject would be higher, thus resulted in increased heat load to bring back the system to steady state temperature of 343K. This impacted less GOR of 0.7 upto 0.78 at higher vacuum pressure and significantly higher STEC from 804 kWh/m^3 to 897 kWh/m^3 making the system inefficient in energy.

The proposed system of HP integrated with HF-VMD with the compressor load of 4.4kW can handle the system with better energy efficiency. As the condenser can contribute heating load upto 19.4 kW, the energy efficiency of the overall system is considerably increased. GOR of the integrated system can be lifted up to 3.05 in comparison with the stand alone system GOR 0.78. Subsequently, the STEC has considerably decreased from 897 kWh/m^3 to minimum of

232.86 kWh/m^3 respectively as shown in Figure 47(b). This shows the strong potential of the HP integration to enhance the energy efficiency of HF-VMD system.

5.8.3 Energy performance analysis of HF-VMD integrated with HP for varying feed temperature

Feed temperature of the system varied from 313K to 353K to analyse the system performance and energy metrics such as GOR and STEC respectively. Upon increasing the feed temperature, vapor pressure increases non-linearly with temperature that contributes both higher permeate flowrate and higher reject temperature which has agreement with antoine equation as shown in equation (2-12).

The feed temperature is critical operating variable in MD, as the variation revealed key insights in energy consumption and the system performance. The stand alone HF-VMD has the minimum GOR of 0.57 and STEC of 1349 kWh/m3 when operated at the lower temperatures as shown in Figure 48(a). However at higher feed temperature the maximum GOR could achieve upto 0.83 with STEC of 853.3409 though the permeate flowrate rises, yet the HF-VMD system is considerably ineffiecient energy metrics.

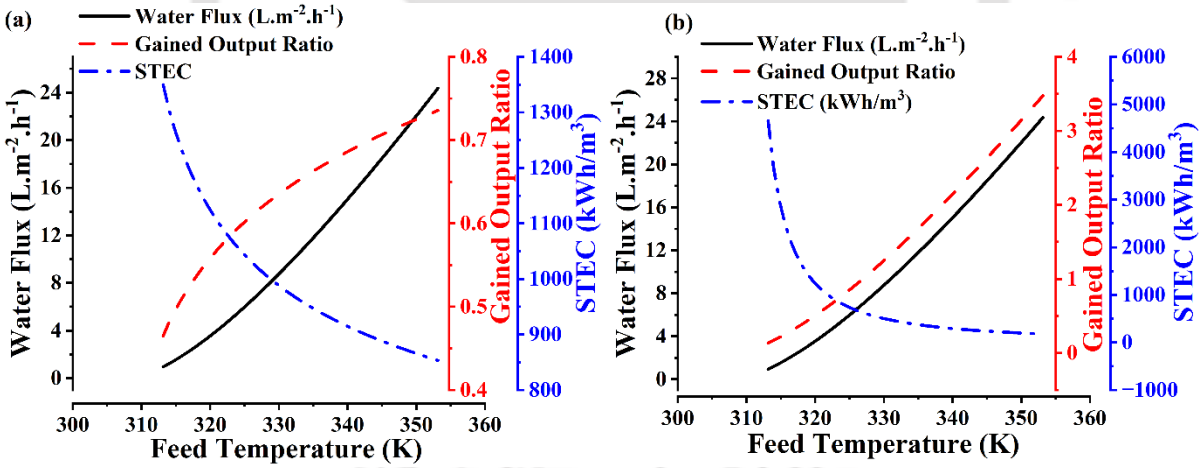

Figure 48: The effect of Feed temperature(K) on permeate flowrate, GOR and STEC at the operating conditions: Feed flowrate 600 L/h, Concentration 1 g/L, Vacuum pressure 6kPa

Upon integrating with HP with the fixed compressor load of 4.4kW, the HF-VMD significantly performs in the energy metrics. Though initially STEC is higher and lower GOR at lower feed temperature, the system revamps to higher efficiency when the feed temperature rises. The maximum GOR of 3.94 with minimum STEC of 180.68 kWh/m^3 from 1349.8 kWh/m^3 i.e. 86.6% of minimization of energy were achieved as shown in Figure 48(b). Since the HF-VMD system usually operated for higher permeate flowrate, these results demonstrate the substantial

efficiency gains possible through combined thermal recovery and membrane optimization in VMD systems.

Table 18: Performance comparison of different VMD energy-integration configurations

Integration	Flux ($L.m^{-2}.h^{-1}$)	GOR	COP		STEC ($kWh.m^{-3}$)	Energy savings (%)
			Hot	Cold		
Standalone VMD	18	0.35	-	-	1800	0
VMD-HX	18	0.6	-	-	1100	40
VMD-VC+HX	18	1	-	-	600	70
HP-VMD	18	2	3.5	2.5	340	86
TEHP-VMD	18	0.8	1	0.3	1300	30

5.9 Investigation of pitch characterization

5.9.1 Solubility Test

The solubility test was conducted to evaluate the dissolution behavior of pitch in various solvents. The results indicate that dichloromethane, toluene, and dichloroethane completely solubilized the pitch, suggesting that the material exhibits a high affinity toward non-polar organic solvents. Partial solubility was observed in sulfuric acid, which indicates possible chemical interactions between sulfur-containing compounds in the pitch and the acid. Other solvents, including acetone, n-hexane, ethanol, ammonia, N-methyl-2-pyrrolidone, nitric acid and hydrochloric acid, showed poor dissolution capability as shown in Figure 49, confirming the chemically stable and non-polar nature of the pitch. These results highlight that pitch is largely hydrophobic and selectively soluble in specific solvents, which has implications for its processing and purification.

Figure 49: Solubility of pitch in various solvent

5.9.2 Energy-Dispersive X-ray Spectroscopy (EDX) Analysis

EDX analysis was performed to determine the elemental composition of the pitch sample. The results confirm the presence of molybdenum and sulfur as significant components as shown in Figure 50. The excitation of both elements at similar wavelengths indicates that the sulfur layer is covering the molybdenum surface, leading to a higher sigma value for molybdenum composition. This suggests that the molybdenum in the pitch is primarily present in a sulfur-stabilized state, which could affect its thermal and catalytic properties.

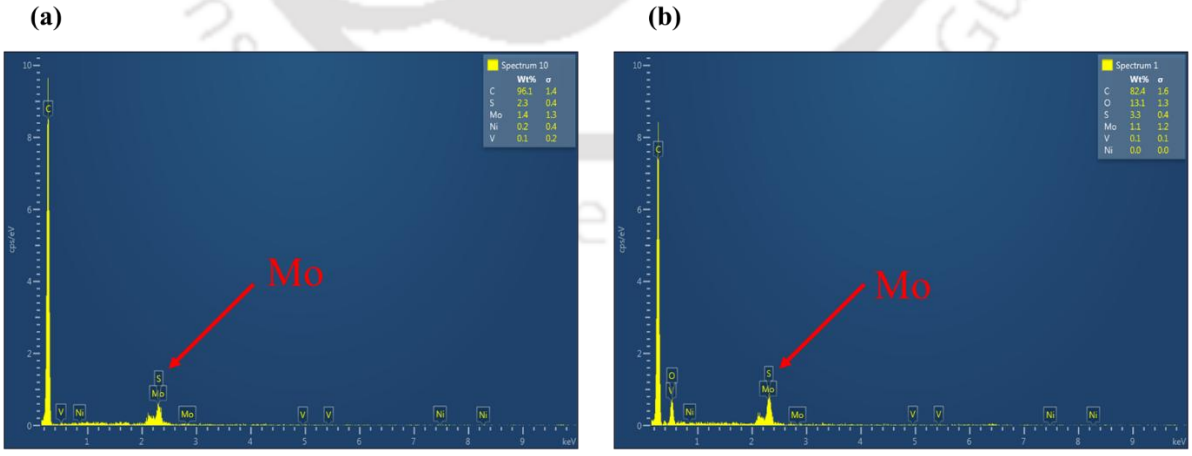

Figure 50: EDX analysis of pitch

5.9.3 Thermogravimetric Analysis

TGA was performed to study the thermal decomposition behavior of the pitch. The thermogravimetric curve shows multiple exothermic and endothermic peaks corresponding to different thermal conditions; Exothermic peaks at 240°C and 440°C indicate the loss of hydrocarbons and transformation of sulfides into metal oxides. This suggests that molybdenum sulfide phases undergo oxidation at elevated temperatures. Endothermic peaks at 185°C, 340°C, and 510°C correspond to the α → β transition of sulfur, the melting of β-sulfur, and the complete sublimation of sulfur, respectively as shown in Figure 51. These transitions confirm the presence of sulfur-rich phases in the pitch, which can significantly affect its processing and high-temperature applications

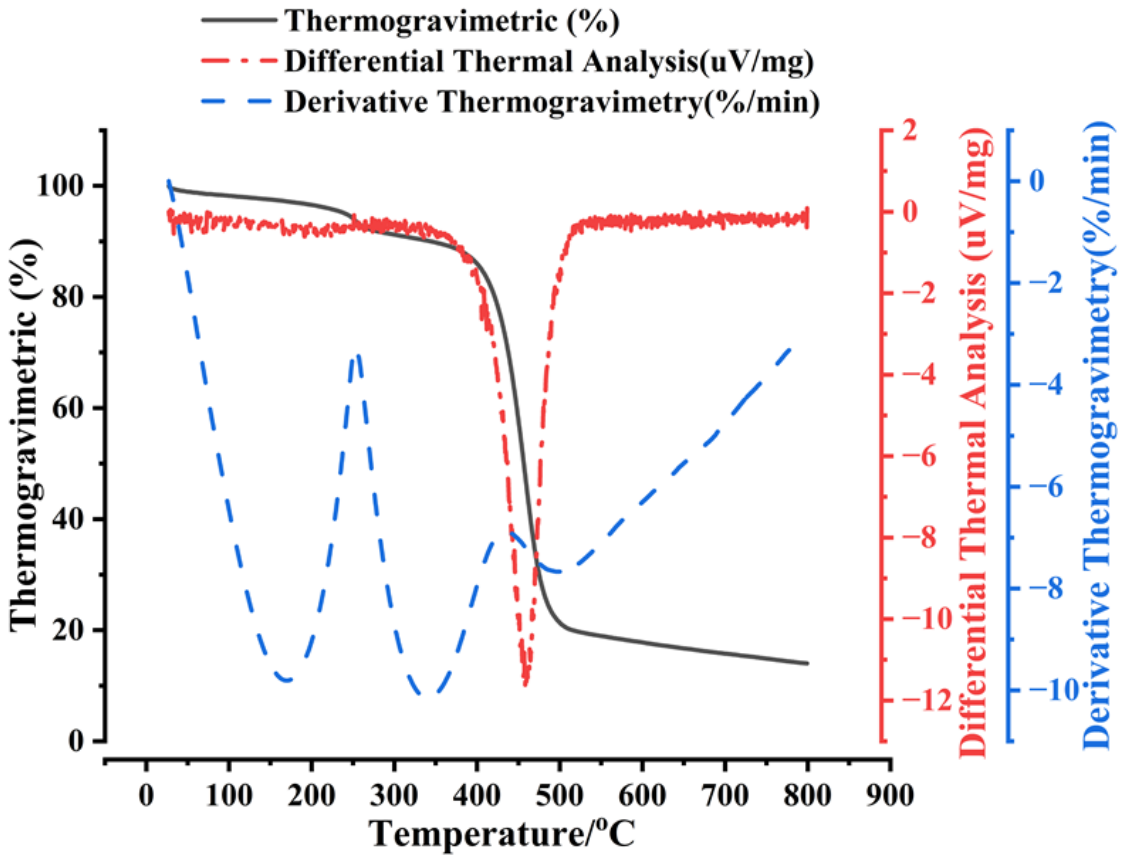

Figure 51: TGA analysis of pitch

5.9.4 X-ray Photoelectron Spectroscopy

XPS analysis was conducted to examine the chemical states of carbon, molybdenum, and sulfur in the pitch sample as shown in Figure 52. The binding energy (BE) of 532.7 eV corresponds to the presence of C=O functional groups, indicating oxidation or oxygen-containing species. The BE of 284.7 eV confirms the presence of C=C bonds, suggesting a highly aromatic or

graphitic nature of the pitch. The BE of 228 eV suggests that molybdenum metal is overlapped with sulfur (S_2), indicating the formation of Mo-S bonds. These findings suggest that the pitch contains a complex mixture of carbon-based structures along with molybdenum sulfide phases, which could be crucial for applications in catalysis or energy storage.

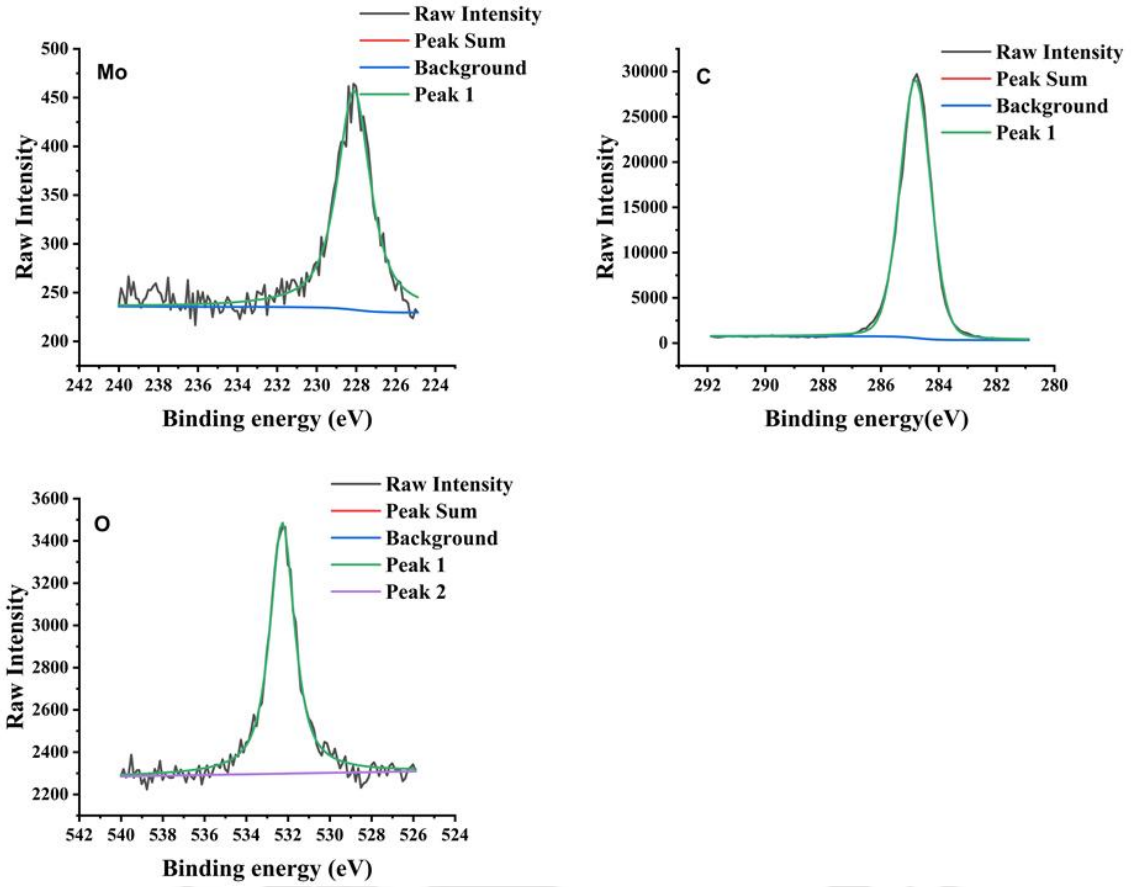

Figure 52: XPS analysis of pitch

5.9.5 Inductively Coupled Plasma Mass Spectroscopy (ICP-MS)

The concentration of metal ion in the heavy fraction pitch is analysed using ICP-MS instrument. The molybdenum concentration found to be in the range of 1.2-1.4 mg/g of pitch. The targeted pitch was attempted to recover from organic phase(toluene) to aqueous phase using acids like HNO_3, HCL and aqua regia. The percentage recovery in each stage is tabulated in Table 19 and the concentration measurement along with permeate and reject is listed in the Table 20. ICP-MS analysis of molybdenum accumulated in the pitch was performed in triplicate for each condition (n = 3). The measured Mo content ranged from 1.2 to 1.4 $mg \cdot g^{-1}$, with a mean value of 1.30 $mg \cdot g^{-1}$ and a standard deviation of ±0.08 $mg \cdot g^{-1}$, corresponding to

a relative standard deviation (RSD) below 7%. This low variability indicates good repeatability of the measurements and consistent molybdenum uptake by the pitch.

Table 19: Stage wise contact of solvent with pitch dissolved in organic solvent

Solvent	Stage 1 (%)	Stage 2 (%)	Stage 3 (%)
HNO_3	10	0.65	0.415
Aqua regia	7.2	0.5	0.3
HCL	5	0.35	0.1

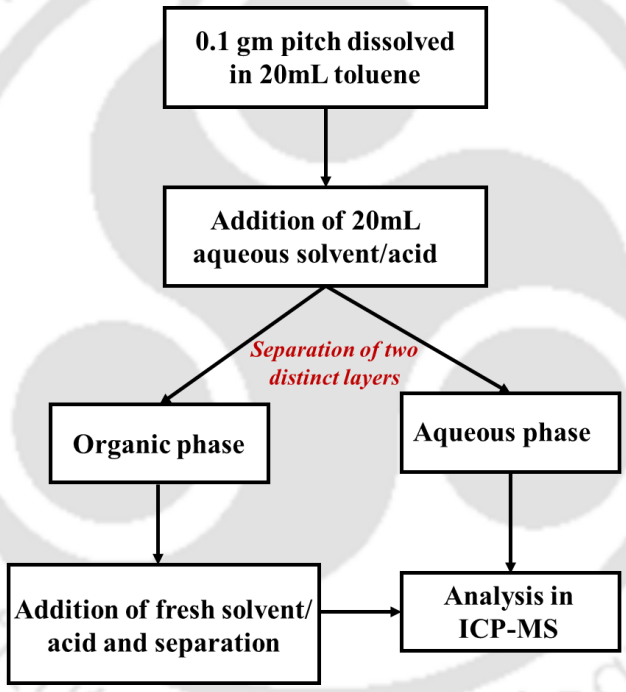

Figure 53: Separation of metal ion from organic to aqueous phase

Table 20: ICP-MS permeate Mo concentrations and calculated rejection values (LOD = 1 µg·L⁻¹ for molybdenum)

Feed concentration (µg/L) *10^6	**Permeate concentration (µg/L)**	**LOD (µg/L)**	**Rejection (%)**
5	<1	1	99.99
10	<1	1	99.98
15	<1	1	99.98
20	<1	1	99.98
30	<1	1	99.99
35	<1	1	99.98

5.10 Extraction of Molybdenum from pitch using different solvents

The recovery of molybdenum from the heavy fraction pitch using acids are very traceable; in order to enhance the recovery, hydrometallurgy technique is combined with pyrometallurgy technique such as pyrolysis for the extraction. Among the different solvents, ammonia favours the highest extraction of 48.5% in the third stage, during the contact in the first stage ammonia recovers close to 35% of molybdenum as shown in Figure 54. The molybdenum could be precipitated as ammonium molybdate in the reaction.

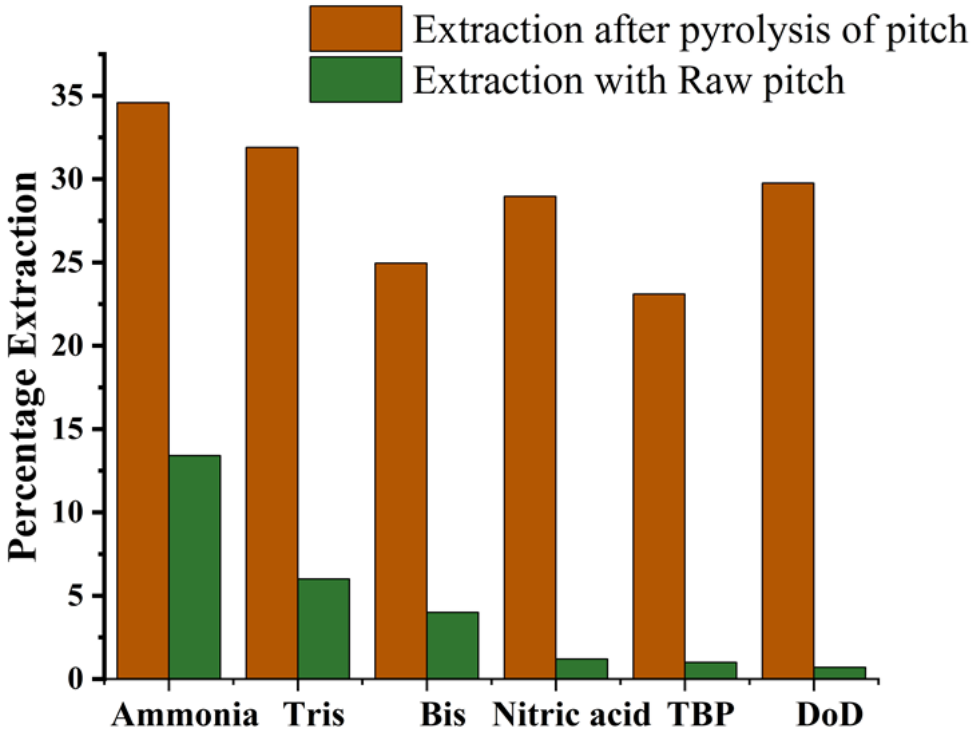

Figure 54: Comparison of the effect of pyrolysis followed by solvent extraction

Chapter 06

Conclusion and future work

6 Conclusion

The primary objective of the present study was to address the limitations associated with the scaling up of VMD process in process industries for recovering the secondary source of valuables and desalination applications. VMD process is sustainable, as the energy requirement can be fulfilled by the auxiliary energy source such as waste heat, excess energy available in the process industries typically required around 40-80^{o}C. In the event of non-available energy, the system itself generates valuable latent heat, upon appropriate energy analysis, this can be recovered and reused in the system for heating requirements.

To begin with, the study attempted to develop a 1-Dimensional mathematical model of VMD system to capture the underlying physical phenomena such as mass transport diffusion, concentration and temperature polarization, heat transport mechanism within the module, the effect of membrane material property and geometry etc. This helped to understand the underlying principles that governs the performance of the module.

6.1 Performance analysis of HF-VMD module

The developed 1-Dimensional mathematical model is validated with the actual experimental conditions through which unknown membrane parameters such as tortuosity, heat transfer and mass transfer co-efficient were estimated respectively. The objective function for the optimization sets to be minimization of the MAE between the actual experiment and simulation. The developed 1-D HF-VMD model demonstrates exceptional accuracy, can predict module performance with a maximum relative error of 1.5% for permeate flux, reject temperature, and reject pressure. This high precision was achieved through an innovative model tuning approach proposed in the study. The model indicates that neglecting conduction loss in the equations can lead to errors in estimated parameters, as it affects the relative absolute error value of reject temperature and pressure in the parameter estimation function. the proposed model, which accounts for these phenomena is robust and applicable across a wide range of operating conditions.

- The study also found that increasing the module length beyond 0.5 meters results in a reduction of flux per unit length, eventually reaching an asymptotic value. Module length was found to influence permeate flux distribution.

- Upon decreasing the membrane module length, the non-linearity is more witnessed and the flux is high as 30 times at the entry is recorded. This shows the criticality of membrane length and diameter in the fabrication of the HF-VMD module

- The variation of operating conditions upon the targeted output variables such as flux, reject temperature and reject pressure were systematically evaluated. This resulted in a non-linear increase in permeate flux and reject temperature.

- Increase in feed flowrate increases the flux as the turbulence inside the membrane module increases, the flux increases upto the feed flowrate of 650L/h beyond that it decreases primarily due to thermal and hydrodynamic limitations inherent to the system. While increasing flowrate generally enhances flux by reducing boundary layer effects, excessively high flowrates reduce the residence time of the feed within the membrane module, limiting heat transfer to the membrane surface. This results in a lower membrane interface temperature and reduced vapor pressure gradient, ultimately suppressing flux.

- The concentration polarization coefficient in HF-VMD exhibits a unique behavior, as it increases upon increasing higher feed flow rates, which contrasts with pressure-driven membrane processes such as RO, NF, and UF. The concentration polarization behaviour differed from pressure-driven membrane processes.

- The solute concentration at the membrane surface rises until reaching a CFNF (650 L/h). Beyond this point, the CPC saturates, causing the solute concentration at the membrane surface to decrease, even as the bulk feed concentration continues to increase along the module length.

- This finding concludes that for crystallization application VMD has to be operated at its critical flowrate for desalination applications below or above the critical flowrate based on sensible heat requirement for evaporation for whole module length. This study provides valuable insights for optimizing HF-VMD module design and operation, particularly for applications in desalination and crystallization.

- While the present work has primarily focused on process performance, energy integration, and model validation, membrane fouling behaviour and post-cleaning flux recovery were not examined in detail. Future investigations should therefore

systematically evaluate fouling mechanisms under prolonged operation, particularly when processing high-salinity feeds and operating near saturation or supersaturation conditions. In addition, quantitative assessment of membrane cleaning protocols and flux recovery rates following physical and chemical cleaning would be essential to establish the long-term operational stability.

6.2 Energy requirement in VMD system

Upon studying the performance of the VMD system, to generate the continuous flux two primary energy source is targeted to minimize.

(i) Heating source for continuously heating the feed to compensate the heat loss occurred across the membrane module and also for the initial preheating the feed solution
(ii) Cooling source for condensing the vapor continuously generated in the VMD system.

The major limitations hindering for scaling up this energy demand, a sustainable integration could lift the process efficiency of the system. This study further focused on innovative integration of ERD such as TEHP, HX, VC and HP respectively

6.2.1 Integration of TEHP with VMD system

The novel integration of the VMD and TEHP system has been proposed to effectively condense the pure vapor and preheat the reject stream to meet the feed temperature demand from the VMD system by using the hot and cold energy available in the TEHP system. The performance of the TEHP was studied by varying the operating condition in the VMD system; upon manipulating the operating variables such as feed temperature, feed flowrate and vacuum pressure, the output variables such as permeate and reject stream heat load vary; therefore, based on this requirement a specific number of TEHP devices have been proposed. The COP of the hot side of the TEHP module is close to 1 wherein cold side is 0.3; therefore, two flowsheets were simulated in this study. Upon fixing the number of TEHP modules based on heat load demand, an excess cooling load needs to be supplied using an external condenser, or upon fixing the number of TEHP modules based on cooling load demand, an excess heat needs to be removed from the system for the desired heating of the reject stream.

TEHP found to be modular and scalable for VMD applications, This new configuration is particularly advantageous in applications requiring ultra-pure water at low flow rates, typically less than 10 L/h, where traditional methods may be less efficient or too costly. Potential

applications of this optimized VMD system include dialysis, where ultra-pure water is crucial for patient safety and effective treatment. Additionally, in space applications, the compact and efficient design of TEHP-VMD systems makes them ideal for water purification in spacecraft. Another relevant application is water purification on ships or cruises, where consistent production of high-quality water is essential for both operational needs and the well-being of passengers and crew. The adaptability and cost-effectiveness of TEHP-integrated VMD systems position them as a promising solution in various fields requiring pure water and low-volume outputs, addressing the demand for efficient, compact, and reliable water purification technologies.

6.2.2 Integration of VMD with HX

An initial attempt to recover latent heat in the VMD system using a standalone HX revealed limitation of energy reocvery. Based on mass and energy balance, the maximum recoverable heat from this integration was restricted to just 0.1 kW, as most of the vapor exited the exchanger uncondensed. Consequently, the system still required an additional 16.5 kW of thermal energy input to maintain the feed temperature, while a substantial excess cooling load of 11.1 kW had to be managed using an auxiliary chiller. This outcome highlights a fundamental constraint in standalone HX-based recovery for VMD. The vapor volume limits effective condensation and energy reuse, underscoring the need for more advanced integration strategies.

6.2.3 Integration of VMD with VC

The integration of a VC and HX moderately enhanced thermal energy recovery in the VMD system by increasing the vapor's latent heat through compression, achieving a higher condensate-side temperature. However, the recoverable heat remained limited to 1.52 kW due to vapor mass flow constraints, and a substantial portion of vapor still exited uncondensed. As a result, the system required a significant auxiliary heat input of 15 kW for feed heating and a cooling load of 9.68 kW to manage the excess unutilized heat. These findings indicate that while VC-HX integration offers incremental improvement over a standalone HX, it is not sufficient to close the system's thermal loop.

6.2.4 Integration of VMD with HP

The integration of a HP system with the VMD process proved to be the most effective strategy for simultaneously addressing the system's thermal input and cooling demands. Utilizing

refrigerant R314a, the HP configuration successfully recovered 15 kW of latent heat from vapor condensation on the evaporator side and transferred 19.4 kW to the feed via the condenser, all with a modest compressor input of 4.4 kW. This resulted in a substantial performance improvement, increasing the GOR from 0.73 to 2.57 and reducing the STEC from 1,490 kWh/m³ to 244 kWh/m³, reflecting over 80% energy savings on an electrical basis. While the system produced an excess heat output of 4.5 kW dissipated through an external heat exchanger to maintain thermal balance. The overall integration effectively closed the energy loop, demonstrating the heat pump's strong potential to transform VMD into a scalable and energy-efficient solution for ZLD and resource recovery applications.

6.3 Recovery of Molybdenum from heavy pitch

Pitch is initially characterized for understanding its interactions among the other elements such as sulphur, carbon etc. The results are crucial for the extraction of Mo ion from organic solvent to aqueous solvent to further concentrate and crystallize in VMD system. The characterization results were summarized below

- The solubility analysis confirmed that the pitch exhibits strong affinity toward non-polar organic solvents such as dichloromethane, toluene, and dichloroethane, which completely dissolved the material.
- EDX analysis confirmed Mo and sulfur as major components in the pitch, with sulfur likely forming a surface layer over molybdenum.
- TGA analysis revealed distinct thermal events indicating the presence of sulfur-rich phases in the pitch. Exothermic peaks at 240°C and 440°C suggest hydrocarbon loss and sulfide-to-oxide conversion, while endothermic peaks at 185°C, 340°C, and 510°C correspond to sulfur phase transitions and sublimation.
- XPS analysis revealed that the pitch contains oxygenated carbon (C=O at 532.7 eV) and aromatic or graphitic structures (C=C at 284.7 eV), along with Mo–S bonding (Mo at 228 eV overlapping with S_2).
- Concentration of Mo detected using ICP-MS, further Mo ion attempted to move from organic phase to aqueous phase. In order to increase the extraction, aqueous solvents were contacted in multistage.
- A combined hydrometallurgical and pyrometallurgical approach involving pyrolysis was employed. Among various solvents, ammonia showed the highest extraction

efficiency, recovery of 35% in the first stage and up to 48.5% by the third stage, likely due to the formation of ammonium molybdate.

- Based on the characterization of pitch, sodium molybdate was selected for experimental evaluation for the actual sample. VMD demonstrated excellent rejection performance, with up to 99.99% of Mo ions retained in the reject solution, as confirmed by ICP-MS analysis.

6.3.1 Key outcome of this study

- Maximum permeate flux**:** The HF-VMD system achieved a maximum permeate flux of 9.6 LMH under optimized operating conditions.
- Energy performance**:** Integration of VMD with a heat pump reduced the specific thermal energy consumption from 1,490 $kWh \cdot m^{-3}$ to 244 $kWh \cdot m^{-3}$**,** corresponding to an energy saving of over 80%**.**
- Molybdenum rejection**:** VMD demonstrated excellent separation performance, achieving >99.99% rejection of molybdenum ions, as confirmed by ICP-MS analysis.

References

[1] A.J. Toth, Modelling and optimisation of multi-stage flash distillation and reverse osmosis for desalination of saline process wastewater sources, Membranes (Basel) 10 (2020) 1–18. https://doi.org/10.3390/membranes10100265.

[2] M. Imandoust, S. Taher Kermani Alghorayshi, M. Javidfar, B. Asadi, M. Jafarinasab, S. Qezelbigloo, R. Zahedi, Technical-economic analysis and optimization of multiple effect distillation system by solar energy conversion as the heat source, Solar Energy 280 (2024). https://doi.org/10.1016/j.solener.2024.112859.

[3] N.E. Batista, P.C.M. Carvalho, L.M. Fernández-Ramírez, A.P.S. Braga, Optimizing methodologies of hybrid renewable energy systems powered reverse osmosis plants, Renewable and Sustainable Energy Reviews 182 (2023). https://doi.org/10.1016/j.rser.2023.113377.

[4] A.C. Sun, W. Kosar, Y. Zhang, X. Feng, Vacuum membrane distillation for desalination of water using hollow fiber membranes, J Memb Sci 455 (2014) 131–142. https://doi.org/10.1016/j.memsci.2013.12.055.

[5] A. Yadav, P.K. Labhasetwar, V.K. Shahi, Membrane distillation crystallization technology for zero liquid discharge and resource recovery: Opportunities, challenges and futuristic perspectives, Science of the Total Environment 806 (2022). https://doi.org/10.1016/j.scitotenv.2021.150692.

[6] A.G. Fane, R.W. Schofield, C.J.D. Fell, THE EFFICIENT USE OF ENERGY IN MEMBRANE DISTILLATION, 1987. https://doi.org/https://doi.org/10.1016/0011-9164(87)90099-3.

[7] H. Attia, M.S. Osman, D.J. Johnson, C. Wright, N. Hilal, Modelling of air gap membrane distillation and its application in heavy metals removal, Desalination 424 (2017) 27–36. https://doi.org/10.1016/j.desal.2017.09.027.

[8] U.F. Alqsair, A.M. Alshwairekh, A.M. Alwatban, A. Oztekin, Computational study of sweeping gas membrane distillation process – Flux performance and polarization characteristics, Desalination 485 (2020). https://doi.org/10.1016/j.desal.2020.114444.

[9] J. Swaminathan, H.W. Chung, D.M. Warsinger, F.A. AlMarzooqi, H.A. Arafat, J.H. Lienhard, Energy efficiency of permeate gap and novel conductive gap membrane distillation, J Memb Sci 502 (2016) 171–178. https://doi.org/10.1016/j.memsci.2015.12.017.

[10] J. Zhang, J. De Li, M. Duke, M. Hoang, Z. Xie, A. Groth, C. Tun, S. Gray, Modelling of vacuum membrane distillation, J Memb Sci 434 (2013) 1–9. https://doi.org/10.1016/j.memsci.2013.01.048.

[11] M.A. Izquierdo-Gil, G. Jonsson, Factors affecting flux and ethanol separation performance in vacuum membrane distillation (VMD), 2003. https://doi.org/https://doi.org/10.1016/S0376-7388(02)00540-9.

[12] L. Peha, J.M. Ortiz De Zarate, J. 1 Mengual', Steady States in Membrane Distillation e Influence of Membrane Wetting7, 1993. https://doi.org/10.1039/FT9938904333.

[13] E.W. Tow, D.M. Warsinger, A.M. Trueworthy, J. Swaminathan, G.P. Thiel, S.M. Zubair, A.S. Myerson, J.H. Lienhard V, Comparison of fouling propensity between reverse osmosis, forward osmosis, and membrane distillation, J Memb Sci 556 (2018) 352–364. https://doi.org/10.1016/j.memsci.2018.03.065.

[14] C. Skuse, A. Gallego-Schmid, A. Azapagic, P. Gorgojo, Can emerging membrane-based desalination technologies replace reverse osmosis?, Desalination 500 (2021). https://doi.org/10.1016/j.desal.2020.114844.

[15] P.K. Weyl, WEYL 3,340,186 RECOVERY OF DEMINERALIZED WATER FROM SALINE WATERS Filed May l4, 1967.

[16] S.M. Alawad, D. Lawal, A.E. Khalifa, Optimization of the design and operating parameters of a large-scale vacuum membrane distillation system to improve process performance, Journal of Water Process Engineering 56 (2023). https://doi.org/10.1016/j.jwpe.2023.104369.

[17] B. Li, K.K. Sirkar, Novel membrane and device for vacuum membrane distillation-based desalination process, J Memb Sci 257 (2005) 60–75. https://doi.org/10.1016/j.memsci.2004.08.040.

[18] J.I. Mengual, M. Khayet, M.P. Godino, Heat and mass transfer in vacuum membrane distillation, Int J Heat Mass Transf 47 (2004) 865–875. https://doi.org/10.1016/j.ijheatmasstransfer.2002.09.001.

[19] J. Kim, M. Park, H.K. Shon, J.H. Kim, Performance analysis of reverse osmosis, membrane distillation, and pressure-retarded osmosis hybrid processes, Desalination 380 (2016) 85–92. https://doi.org/10.1016/j.desal.2015.11.019.

[20] N.E. Batista, P.C.M. Carvalho, L.M. Fernández-Ramírez, A.P.S. Braga, Optimizing methodologies of hybrid renewable energy systems powered reverse osmosis plants, Renewable and Sustainable Energy Reviews 182 (2023). https://doi.org/10.1016/j.rser.2023.113377.

[21] S.C. Tsai, W.Z. Huang, G.S. Lin, Z. Wang, K.L. Tung, C.J. Chuang, Evaluation of the Specific Energy Consumption of Sea Water Reverse Osmosis Integrated with Membrane Distillation and Pressure–Retarded Osmosis Processes with Theoretical Models, Membranes (Basel) 12 (2022). https://doi.org/10.3390/membranes12040432.

[22] N.M. Mazlan, D. Peshev, A.G. Livingston, Energy consumption for desalination - A comparison of forward osmosis with reverse osmosis, and the potential for perfect membranes, Desalination 377 (2016) 138–151. https://doi.org/10.1016/j.desal.2015.08.011.

[23] I. Khoshrou, M.R. Jafari Nasr, K. Bakhtari, New opportunities in mass and energy consumption of the Multi-Stage Flash Distillation type of brackish water desalination process, Solar Energy 153 (2017) 115–125. https://doi.org/10.1016/j.solener.2017.05.021.

[24] E.S. Mohamed, P. Boutikos, E. Mathioulakis, V. Belessiotis, Experimental evaluation of the performance and energy efficiency of a Vacuum Multi-Effect Membrane Distillation system, Desalination 408 (2017) 70–80. https://doi.org/10.1016/j.desal.2016.12.020.

[25] K.S.S. Christie, T. Horseman, S. Lin, Energy efficiency of membrane distillation: Simplified analysis, heat recovery, and the use of waste-heat, Environ Int 138 (2020). https://doi.org/10.1016/j.envint.2020.105588.

[26] Y. Zhang, Y. Peng, S. Ji, J. Qi, S. Wang, Numerical modeling and economic evaluation of two multi-effect vacuum membrane distillation (ME-VMD) processes, Desalination 419 (2017) 39–48. https://doi.org/10.1016/j.desal.2017.05.032.

[27] G. Guan, X. Yang, R. Wang, A.G. Fane, Evaluation of heat utilization in membrane distillation desalination system integrated with heat recovery, Desalination 366 (2015) 80–93. https://doi.org/10.1016/j.desal.2015.01.013.

[28] Y. Zhang, Y. Peng, S. Ji, Z. Li, P. Chen, Review of thermal efficiency and heat recycling in membrane distillation processes, Desalination 367 (2015) 223–239. https://doi.org/10.1016/j.desal.2015.04.013.

[29] C.K. Lee, C. Park, Y.C. Woo, J.S. Choi, J.O. Kim, A pilot study of spiral-wound air gap membrane distillation process and its energy efficiency analysis, Chemosphere 239 (2020). https://doi.org/10.1016/j.chemosphere.2019.124696.

[30] Q. Chen, B. Muhammad, F.H. Akhtar, D. Ybyraiymkul, W.S. Muhammad, Y. Li, K.C. Ng, Thermo-economic analysis and optimization of a vacuum multi-effect membrane

distillation system, Desalination 483 (2020). https://doi.org/10.1016/j.desal.2020.114413.

[31] O. Makanjuola, B.S. Lalia, R. Hashaikeh, Thermoelectric heating and cooling for efficient membrane distillation, Case Studies in Thermal Engineering 28 (2021). https://doi.org/10.1016/j.csite.2021.101540.

[32] S.H. Kim, H.K. Lim, Energy efficiency evaluation of a compact direct contact membrane distillation system using thermoelectric modules, Desalination Water Treat 201 (2020) 55–62. https://doi.org/10.5004/dwt.2020.26021.

[33] D.U. Lawal, S.M. Alawad, A.H. Jagaba, S.I. Abba, J. Usman, Q.F. Alsalhy, S.M.H. Shah, I.H. Aljundi, Air gap membrane distillation unit operated by thermoelectric module, Desalination 593 (2025). https://doi.org/10.1016/j.desal.2024.118133.

[34] E. Shaulsky, Z. Wang, A. Deshmukh, V. Karanikola, M. Elimelech, Membrane distillation assisted by heat pump for improved desalination energy efficiency, Desalination 496 (2020). https://doi.org/10.1016/j.desal.2020.114694.

[35] A. Khalifa, A. Mezghani, H. Alawami, Analysis of integrated membrane distillation-heat pump system for water desalination, Desalination 510 (2021). https://doi.org/10.1016/j.desal.2021.115087.

[36] Z. Si, D. Han, Y. Liu, Y. Li, K. Chen, Performance analysis of treating sulfuric acid solution by the combined system of vacuum membrane distillation and mechanical vapor recompression, Chemical Engineering and Processing - Process Intensification 150 (2020). https://doi.org/10.1016/j.cep.2020.107890.

[37] Z. Si, J. Xiang, D. Han, Performance analysis of a vacuum membrane distillation system coupled with heat pump for sulfuric acid solution treatment, Chemical Engineering and Processing - Process Intensification 171 (2022). https://doi.org/10.1016/j.cep.2021.108734.

[38] K.W. Lawson, D.R. Lloyd, Membrane distillation. II. Direct contact MD, 1996. https://doi.org/https://doi.org/10.1016/0376-7388(96)00141-X.

[39] K. Smolders, A.C.M. Franken, Terminology for Membrane Distillation, 1989.

[40] P. Wang, T.S. Chung, Recent advances in membrane distillation processes: Membrane development, configuration design and application exploring, J Memb Sci 474 (2015) 39–56. https://doi.org/10.1016/j.memsci.2014.09.016.

[41] E. Drioli, A. Ali, F. Macedonio, Membrane distillation: Recent developments and perspectives, Desalination 356 (2015) 56–84. https://doi.org/10.1016/j.desal.2014.10.028.

[42] J. Ravi, M.H.D. Othman, T. Matsuura, M. Ro'il Bilad, T.H. El-badawy, F. Aziz, A.F. Ismail, M.A. Rahman, J. Jaafar, Polymeric membranes for desalination using membrane distillation: A review, Desalination 490 (2020). https://doi.org/10.1016/j.desal.2020.114530.

[43] C.R.S. Mesquita, A.O.C. Gómez, C.P.N. Cotta, R.M. Cotta, Comparison of Different Polymeric Membranes in Direct Contact Membrane Distillation and Air Gap Membrane Distillation Configurations, Membranes (Basel) 15 (2025). https://doi.org/10.3390/membranes15030091.

[44] H. Zhang, D. Gong, Y. Zhou, Z. Qin, B. Wen, Influence of Membrane Characteristics on Efficiency of Vacuum Membrane Distillation: a Lattice Boltzmann Study, (2025). https://doi.org/10.1016/j.desal.2025.118943.

[45] E. Curcio, E. Drioli, Membrane distillation and related operations - A review, Separation and Purification Reviews 34 (2005) 35–86. https://doi.org/10.1081/SPM-200054951.

[46] Y. Zhou, L. Chen, M. Huang, W. Hu, G. Chen, B. Wu, Experimental Investigation of the Desalination Process for Direct Contact Membrane Distillation Using Plate and Frame Membrane Module, Applied Sciences (Switzerland) 13 (2023). https://doi.org/10.3390/app13169439.

[47] A. Alkhudhiri, N. Darwish, N. Hilal, Membrane distillation: A comprehensive review, Desalination 287 (2012) 2–18. https://doi.org/10.1016/j.desal.2011.08.027.

[48] J.H. Tsai, C. Quist-Jensen, A. Ali, Multipass hollow fiber membrane modules for membrane distillation, Desalination 548 (2023). https://doi.org/10.1016/j.desal.2022.116239.

[49] A.J. Karabelas, M. Kostoglou, C.P. Koutsou, Modeling of spiral wound membrane desalination modules and plants - review and research priorities, Desalination 356 (2015) 165–186. https://doi.org/10.1016/j.desal.2014.10.002.

[50] A. Ali, M.M. Agha Shirazi, L. Nthunya, R. Castro-Muñoz, N. Ismail, N. Tavajohi, G. Zaragoza, C.A. Quist-Jensen, Progress in module design for membrane distillation, Desalination 581 (2024). https://doi.org/10.1016/j.desal.2024.117584.

[51] B. Li, K.K. Sirkar, Novel membrane and device for vacuum membrane distillation-based desalination process, J Memb Sci 257 (2005) 60–75. https://doi.org/10.1016/j.memsci.2004.08.040.

[52] F. Shao, C. Hao, L. Ni, Y. Zhang, R. Du, J. Meng, Z. Liu, C. Xiao, Experimental and theoretical research on N-methyl-2-pyrrolidone concentration by vacuum membrane distillation using polypropylene hollow fiber membrane, J Memb Sci 452 (2014) 157–164. https://doi.org/10.1016/j.memsci.2013.09.041.

[53] A.S. Alsaadi, L. Francis, G.L. Amy, N. Ghaffour, Experimental and theoretical analyses of temperature polarization effect in vacuum membrane distillation, J Memb Sci 471 (2014) 138–148. https://doi.org/10.1016/j.memsci.2014.08.005.

[54] G. Zuo, G. Guan, R. Wang, Numerical modeling and optimization of vacuum membrane distillation module for low-cost water production, Desalination 339 (2014) 1–9. https://doi.org/10.1016/j.desal.2014.02.005.

[55] G. Guan, X. Yang, R. Wang, R. Field, A.G. Fane, Evaluation of hollow fiber-based direct contact and vacuum membrane distillation systems using aspen process

simulation, J Memb Sci 464 (2014) 127–139. https://doi.org/10.1016/j.memsci.2014.03.054.

[56] J.G. Lee, W.S. Kim, Numerical modeling of the vacuum membrane distillation process, Desalination 331 (2013) 46–55. https://doi.org/10.1016/j.desal.2013.10.022.

[57] Y.S. Chang, B.S. Ooi, A.L. Ahmad, C.P. Leo, W.J. Lau, Numerical study on performance and efficiency of batch submerged vacuum membrane distillation for desalination, Chemical Engineering Research and Design 163 (2020) 217–229. https://doi.org/10.1016/j.cherd.2020.08.031.

[58] M. Suleman, M. Asif, S.A. Jamal, P. Dong, X. Xi, A numerical study on the effects of operational parameters and membrane characteristics on the performance of vacuum membrane distillation (Vmd), Desalination Water Treat 183 (2020) 182–193. https://doi.org/10.5004/dwt.2020.25320.

[59] Z. Triki, Z. Fergani, H. Tahraoui, Modeling of heat and mass transfer in vacuum membrane distillation for seawater desalination, Desalination Water Treat 313 (2023) 12–25. https://doi.org/10.5004/dwt.2023.30083.

[60] Y.D. Kim, Y. Bin Kim, S.Y. Woo, Detailed modeling and simulation of an out-in configuration vacuum membrane distillation process, Water Res 132 (2018) 23–33. https://doi.org/10.1016/j.watres.2017.12.066.

[61] J. Zhang, J. De Li, M. Duke, M. Hoang, Z. Xie, A. Groth, C. Tun, S. Gray, Modelling of vacuum membrane distillation, J Memb Sci 434 (2013) 1–9. https://doi.org/10.1016/j.memsci.2013.01.048.

[62] D.M. Scheepers, A.J. Tahir, C. Brunner, E. Guillen-Burrieza, Vacuum membrane distillation multi-component numerical model for ammonia recovery from liquid streams, J Memb Sci 614 (2020). https://doi.org/10.1016/j.memsci.2020.118399.

[63] Y.T. Chua, G. Ji, G. Birkett, C.X.C. Lin, F. Kleitz, S. Smart, Nanoporous organosilica membrane for water desalination: Theoretical study on the water transport, J Memb Sci 482 (2015) 56–66. https://doi.org/10.1016/j.memsci.2015.01.060.

[64] B. Lian, Y. Wang, P. Le-Clech, V. Chen, G. Leslie, A numerical approach to module design for crossflow vacuum membrane distillation systems, J Memb Sci 510 (2016) 489–496. https://doi.org/10.1016/j.memsci.2016.03.041.

[65] S.M. Shim, J.G. Lee, W.S. Kim, Performance simulation of a multi-VMD desalination process including the recycle flow, Desalination 338 (2014) 39–48. https://doi.org/10.1016/j.desal.2013.12.009.

[66] A.C. Sun, W. Kosar, Y. Zhang, X. Feng, Vacuum membrane distillation for desalination of water using hollow fiber membranes, J Memb Sci 455 (2014) 131–142. https://doi.org/10.1016/j.memsci.2013.12.055.

[67] X. Yang, M. Duke, J. Zhang, J. De Li, Modeling of heat and mass transfer in vacuum membrane distillation for ammonia separation, Sep Purif Technol 224 (2019) 121–131. https://doi.org/10.1016/j.seppur.2019.05.004.

[68] G. Alfonso, S. Laborie, C. Cabassud, Modeling-based investigation on the contribution of radial heating into integrated VMD hollow-fiber modules at different scales for autonomous desalination, Desalination 569 (2024). https://doi.org/10.1016/j.desal.2023.117032.

[69] Y. Zhang, Y. Peng, S. Ji, S. Wang, Numerical simulation of 3D hollow-fiber vacuum membrane distillation by computational fluid dynamics, Chem Eng Sci 152 (2016) 172–185. https://doi.org/10.1016/j.ces.2016.05.040.

[70] S.G. Lovineh, M. Asghari, B. Rajaei, Numerical simulation and theoretical study on simultaneous effects of operating parameters in vacuum membrane distillation, Desalination 314 (2013) 59–66. https://doi.org/10.1016/j.desal.2013.01.005.

[71] H. Hayer, O. Bakhtiari, T. Mohammadi, Analysis of heat and mass transfer in vacuum membrane distillation for water desalination using computational fluid dynamics (CFD), Desalination Water Treat 55 (2015) 39–52. https://doi.org/10.1080/19443994.2014.912158.

[72] Q. Ma, X. Liu, L. Tong, J. Li, Z. Wu, H. Lu, H. Luo, C. Wang, S. Wang, Theoretical, numerical and experimental research on an innovative ocean thermal energy conversion coupled VMD desalination system, Desalination 571 (2024). https://doi.org/10.1016/j.desal.2023.117097.

[73] Z. Zhang, N. Zhang, B. Xiang, Y. Yuan, P.E. Phelan, Numerical investigation on mass and heat transfer performance for novel vacuum membrane distillation modules enhanced by semicircular spacers, International Journal of Thermal Sciences 187 (2023). https://doi.org/10.1016/j.ijthermalsci.2023.108165.

[74] A.E. Anqi, M. Usta, R. Krysko, J.G. Lee, N. Ghaffour, A. Oztekin, Numerical study of desalination by vacuum membrane distillation – Transient three-dimensional analysis, J Memb Sci 596 (2020). https://doi.org/10.1016/j.memsci.2019.117609.

[75] L. Zhang, J. Xiang, P.G. Cheng, N. Tang, H. Han, L. Yuan, H. Zhang, S. Wang, X. Wang, Three-dimensional numerical simulation of aqueous NaCl solution in vacuum membrane distillation process, Chemical Engineering and Processing: Process Intensification 87 (2015) 9–15. https://doi.org/10.1016/j.cep.2014.11.002.

[76] J. Zhou, Y. Hu, J. Zhao, X. Niu, F. Wang, Z. Dai, X. Zhang, Conjugate heat and mass transfer in vacuum membrane distillation for solution regeneration using hollow fiber membranes, Appl Therm Eng 241 (2024). https://doi.org/10.1016/j.applthermaleng.2024.122346.

[77] G. Naidu, Y. Choi, S. Jeong, T.M. Hwang, S. Vigneswaran, Experiments and modeling of a vacuum membrane distillation for high saline water, Journal of Industrial and Engineering Chemistry 20 (2014) 2174–2183. https://doi.org/10.1016/j.jiec.2013.09.048.

[78] H. Kim, T. Yun, S. Hong, S. Lee, Experimental and theoretical investigation of a high performance PTFE membrane for vacuum-membrane distillation, J Memb Sci 617 (2021). https://doi.org/10.1016/j.memsci.2020.118524.

[79] A. Criscuoli, M.C. Carnevale, E. Drioli, Modeling the performance of flat and capillary membrane modules in vacuum membrane distillation, J Memb Sci 447 (2013) 369–375. https://doi.org/10.1016/j.memsci.2013.07.044.

[80] A. Omar, Q. Li, A. Nashed, J. Guan, P. Dai, R.A. Taylor, Experimental and numerical investigation of a new hollow fiber-based multi-effect vacuum membrane distillation design, Desalination 501 (2021). https://doi.org/10.1016/j.desal.2020.114908.

[81] Y.D. Kim, K. Thu, S.H. Choi, Solar-assisted multi-stage vacuum membrane distillation system with heat recovery unit, Desalination 367 (2015) 161–171. https://doi.org/10.1016/j.desal.2015.04.003.

[82] W. Su, J. Li, Z. Lu, X. Jin, J. Zhang, Z. Liu, Z. Xiaosong, Performance analysis and optimization of a solar assisted heat pump-driven vacuum membrane distillation system for liquid desiccant regeneration, Energy Convers Manag 301 (2024). https://doi.org/10.1016/j.enconman.2023.118047.

[83] Q. Ma, A. Ahmadi, C. Cabassud, Optimization and design of a novel small-scale integrated vacuum membrane distillation - solar flat-plate collector module with heat recovery strategy through heat pumps, Desalination 478 (2020). https://doi.org/10.1016/j.desal.2019.114285.

[84] Z. Si, D. Han, Y. Xing, J. Xiang, Experimental and numerical study on thermodynamic characteristics of a vacuum membrane distillation system based on mechanical vapor recompression for sulfuric acid waste, Chemical Engineering and Processing - Process Intensification 174 (2022). https://doi.org/10.1016/j.cep.2022.108862.

[85] Y.Z. Tan, L. Han, N.G.P. Chew, W.H. Chow, R. Wang, J.W. Chew, Membrane distillation hybridized with a thermoelectric heat pump for energy-efficient water treatment and space cooling, Appl Energy 231 (2018) 1079–1088. https://doi.org/10.1016/j.apenergy.2018.09.196.

[86] O. Makanjuola, R. Hashaikeh, Assessing thermoelectric membrane distillation performance: An experimental design approach, MethodsX 12 (2024). https://doi.org/10.1016/j.mex.2024.102604.

[87] D. Afaneh, H. Bahaidarah, D.U. Lawal, M.A. Antar, Novel integration of thermoelectric distiller with direct contact membrane distillation, Energy Conversion and Management: X 22 (2024). https://doi.org/10.1016/j.ecmx.2024.100575.

[88] Ahmadou Tidiane Diaby, Paul Byrne, Patrick Loulergue, Ousmane Sow, Thierry Maré, Experimental study of a heat pump for simultaneous cooling and desalination by membrane distilation, Membranes (Basel) (2021). https://doi.org/https://doi.org/10.3390/ membranes11100725.

[89] N. Dutta, B. Singh, S. Subbiah, P. Muthukumar, Performance analysis of a single and multi-staged direct contact membrane distillation module integrated with heat recovery units, Chemical Engineering Journal Advances 4 (2020) 100055. https://doi.org/10.1016/j.ceja.2020.100055.

[90] S.B. Sasongko, G.J. Sanyoto, L. Buchori, Study of Performance: An Improved Distillation using Thermoelectric Modules, Chem Eng Trans 89 (2021) 649–654. https://doi.org/10.3303/CET2189109.

[91] O. Makanjuola, B.S. Lalia, R. Hashaikeh, Thermoelectric heating and cooling for efficient membrane distillation, Case Studies in Thermal Engineering 28 (2021). https://doi.org/10.1016/j.csite.2021.101540.

[92] S.O. Olatunji, L.M. Camacho, Heat and mass transport in modeling membrane distillation configurations: A review, Front Energy Res 6 (2018). https://doi.org/10.3389/fenrg.2018.00130.

[93] Ó. Andrjesdóttir, C.L. Ong, M. Nabavi, S. Paredes, A.S.G. Khalil, B. Michel, D. Poulikakos, An experimentally optimized model for heat and mass transfer in direct contact membrane distillation, Int J Heat Mass Transf 66 (2013) 855–867. https://doi.org/10.1016/j.ijheatmasstransfer.2013.07.051.

[94] L. Gao, J. Zhang, S. Gray, J. De Li, Modelling mass and heat transfers of Permeate Gap Membrane Distillation using hollow fibre membrane, Desalination 467 (2019) 196–209. https://doi.org/10.1016/j.desal.2019.06.014.

[95] I. Hitsov, T. Maere, K. De Sitter, C. Dotremont, I. Nopens, Modelling approaches in membrane distillation: A critical review, Sep Purif Technol 142 (2015) 48–64. https://doi.org/10.1016/j.seppur.2014.12.026.

[96] K.S. Chauhan, H. Tyagi, Thermal modeling of fluid flow and heat transfer in direct contact membrane distillation, Energy Convers Manag 291 (2023). https://doi.org/10.1016/j.enconman.2023.117249.

[97] J. Liu, B. Xie, N. Mushtaq, G. Xu, E. Bar-Zeev, Y. Hu, New insights into the role of carbon nanotubes spray-coated on both sides of the PTFE membrane in suppressing temperature polarization and enhancing water flux in direct contact membrane distillation, J Memb Sci 689 (2024). https://doi.org/10.1016/j.memsci.2023.122184.

[98] J. Bose, S. Chowdhury, U. Adhikari, J. Sikder, Optimisation of direct contact membrane distillation to enhance brackish water desalination and study polyvinylidene fluoride (PVDF) membrane performance, Comput Chem Eng 181 (2024). https://doi.org/10.1016/j.compchemeng.2023.108529.

[99] K.T. Rashid, S.B.A. Rahman, Q.F. Alsalhy, Optimum Operating Parameters for Hollow Fiber Membranes in Direct Contact Membrane Distillation, Arab J Sci Eng 41 (2016) 2647–2658. https://doi.org/10.1007/s13369-016-2178-3.

[100] E. Jang, S.H. Nam, T.M. Hwang, S. Lee, Y. Choi, Effect of operating parameters on temperature and concentration polarization in vacuum membrane distillation process, Desalination Water Treat 54 (2015) 871–880. https://doi.org/10.1080/19443994.2014.952673.

[101] A.L. McGaughey, R.D. Gustafson, A.E. Childress, Effect of long-term operation on membrane surface characteristics and performance in membrane distillation, J Memb Sci 543 (2017) 143–150. https://doi.org/10.1016/j.memsci.2017.08.040.

[102] A. Ali, J.H. Tsai, K.L. Tung, E. Drioli, F. Macedonio, Designing and optimization of continuous direct contact membrane distillation process, Desalination 426 (2018) 97–107. https://doi.org/10.1016/j.desal.2017.10.041.

[103] J. Xu, Y.B. Singh, G.L. Amy, N. Ghaffour, Effect of operating parameters and membrane characteristics on air gap membrane distillation performance for the treatment of highly saline water, J Memb Sci 512 (2016) 73–82. https://doi.org/10.1016/j.memsci.2016.04.010.

[104] A. Ruiz-Aguirre, J.A. Andrés-Mañas, J.M. Fernández-Sevilla, G. Zaragoza, Experimental characterization and optimization of multi-channel spiral wound air gap membrane distillation modules for seawater desalination, Sep Purif Technol 205 (2018) 212–222. https://doi.org/10.1016/j.seppur.2018.05.044.

[105] H.C. Duong, P. Cooper, B. Nelemans, T.Y. Cath, L.D. Nghiem, Optimising thermal efficiency of direct contact membrane distillation by brine recycling for small-scale seawater desalination, Desalination 374 (2015) 1–9. https://doi.org/10.1016/j.desal.2015.07.009.

[106] R. Ullah, M. Khraisheh, R.J. Esteves, J.T. McLeskey, M. AlGhouti, M. Gad-el-Hak, H. Vahedi Tafreshi, Energy efficiency of direct contact membrane distillation, Desalination 433 (2018) 56–67. https://doi.org/10.1016/j.desal.2018.01.025.

[107] E. Ali, J. Orfi, S. Mokraoui, Hybrid Mechanical Vapor Compression and Membrane Distillation System: Concept and Analysis, Membranes (Basel) 15 (2025). https://doi.org/10.3390/membranes15030069.

[108] Seung Jin Oh, Yeongmin Kim, Youngsun Hong, Jong Woo Kim, Numerical Study on the performance of a heat pump-driven-DCMD for sustainable desalination, (n.d.). https://doi.org/https://doi.org/10.3389/fenrg.2022.1053219.

[109] Z. Si, D. Han, J. Gu, Y. Song, Y. Liu, Exergy analysis of a vacuum membrane distillation system integrated with mechanical vapor recompression for sulfuric acid waste treatment, Appl Therm Eng 178 (2020). https://doi.org/10.1016/j.applthermaleng.2020.115516.

[110] U. Loganathan, S.B. Reddy, Development of Hybrid Source Thermal Desalination System using Thermoelectric Module as a Powerful Heat Pump, Energy Proceedings 22 (2021) 2021.

[111] D. Milani, A. Abbas, A. Vassallo, M. Chiesa, D. Al Bakri, Evaluation of using thermoelectric coolers in a dehumidification system to generate freshwater from ambient air, Chem Eng Sci 66 (2011) 2491–2501. https://doi.org/10.1016/j.ces.2011.02.018.

[112] D. González, J. Amigo, F. Suárez, Membrane distillation: Perspectives for sustainable and improved desalination, Renewable and Sustainable Energy Reviews 80 (2017) 238–259. https://doi.org/10.1016/j.rser.2017.05.078.

[113] Improvement of Air Gap Membrane Distillation (AGMD) by Peltier's Effect and Condensation Plate Modifications, 2019.

[114] H. Al-Madhhachi, Effective Thermal Analysis of Using Peltier Module for Desalination Process, n.d. www.astesj.com.

[115] R. González-Bravo, N.A. Elsayed, J.M. Ponce-Ortega, F. Nápoles-Rivera, M.M. El-Halwagi, Optimal design of thermal membrane distillation systems with heat integration with process plants, Appl Therm Eng 75 (2015) 154–166. https://doi.org/10.1016/j.applthermaleng.2014.09.009.

[116] Q. Li, L.J. Beier, J. Tan, C. Brown, B. Lian, W. Zhong, Y. Wang, C. Ji, P. Dai, T. Li, P. Le Clech, H. Tyagi, X. Liu, G. Leslie, R.A. Taylor, An integrated, solar-driven membrane distillation system for water purification and energy generation, Appl Energy 237 (2019) 534–548. https://doi.org/10.1016/j.apenergy.2018.12.069.

[117] H. Bamufleh, F. Abdelhady, H.M. Baaqeel, M.M. El-Halwagi, Optimization of multi-effect distillation with brine treatment via membrane distillation and process heat integration, Desalination 408 (2017) 110–118. https://doi.org/10.1016/j.desal.2017.01.016.

[118] A. Najib, E. Ali, H. Al-Ansary, F.A. Almehmadi, Experimental Evaluation of a Direct Contact Membrane Distillation System Efficiency Under Single- and Double-Stage Cooling Modes, Arab J Sci Eng (2025). https://doi.org/10.1007/s13369-024-09886-7.

[119] Z. Liu, X. Lu, C. Wu, J. Gu, Q. Wu, Exploiting the potential of a novel “in-situ latent heat recovery” in hollow-fiber vacuum membrane distillation process for simultaneously improved water production and energy efficiency, Water Res 256 (2024). https://doi.org/10.1016/j.watres.2024.121586.

[120] J. Swaminathan, H.W. Chung, D.M. Warsinger, J.H. Lienhard V, Membrane distillation model based on heat exchanger theory and configuration comparison, Appl Energy 184 (2016) 491–505. https://doi.org/10.1016/j.apenergy.2016.09.090.

[121] Z. Si, D. Han, J.M. Gu, Y. Song, P.P. Zhang, Characteristics analysis of a combined system of vacuum membrane distillation and mechanical vapor recompression, Desalination Water Treat 171 (2019) 29–43. https://doi.org/10.5004/dwt.2019.24781.

[122] J. Swaminathan, K.G. Nayar, J.H. Lienhard V, Mechanical vapor compression—Membrane distillation hybrids for reduced specific energy consumption, Desalination Water Treat 57 (2016) 26507–26517. https://doi.org/10.1080/19443994.2016.1168579.

[123] J. Li, Z. Si, Y. Yang, Parametric investigation of a vacuum membrane distillation system driven by mechanical vapor recompression, Desalination Water Treat 273 (2022) 43–54. https://doi.org/10.5004/dwt.2022.28860.

[124] Z. Si, D. Han, J. Xiang, Experimental investigation on the mechanical vapor recompression evaporation system coupled with multiple vacuum membrane distillation modules to treat industrial wastewater, Sep Purif Technol 275 (2021). https://doi.org/10.1016/j.seppur.2021.119178.

[125] Z. Si, Z. Li, X. Zhuang, D. Zhou, Experimental investigation on the hybrid system of mechanical vapor recompression and hollow fiber vacuum membrane distillation applied for wastewater treatment, J Environ Manage 350 (2024). https://doi.org/10.1016/j.jenvman.2023.119633.

[126] Z. Si, D. Han, J. Gu, J. Chen, M. Zheng, Y. Song, N. Mao, Study on vacuum membrane distillation coupled with mechanical vapor recompression system for the concentration of sulfuric acid solution, Journal of the Brazilian Society of Mechanical Sciences and Engineering 41 (2019). https://doi.org/10.1007/s40430-019-1967-5.

[127] A. Khalifa, A. Mezghani, H. Alawami, Analysis of integrated membrane distillation-heat pump system for water desalination, Desalination 510 (2021). https://doi.org/10.1016/j.desal.2021.115087.

[128] M. Bindels, B. Nelemans, Cost reduction of heat pump assisted membrane distillation by using variable electricity prices, Desalination 530 (2022). https://doi.org/10.1016/j.desal.2022.115669.

[129] L. Wang, H. Cui, C. Fu, Performance investigation of a novel heating tower heat pump system with integrated air gap membrane distillation regenerator, Energy Convers Manag 232 (2021). https://doi.org/10.1016/j.enconman.2021.113891.

[130] Z. Si, J. Xiang, D. Han, Performance analysis of a vacuum membrane distillation system coupled with heat pump for sulfuric acid solution treatment, Chemical Engineering and Processing - Process Intensification 171 (2022). https://doi.org/10.1016/j.cep.2021.108734.

[131] M. Zhang, H. Song, C. Zheng, Z. Lin, Y. Liu, W. Wu, X. Gao, Highly efficient recovery of molybdenum from spent catalyst by optimized process, J Air Waste Manage Assoc (2020) 971–979. https://doi.org/10.1080/10962247.2020.1792377.

[132] S.H.R. Rouhani, R. Davarkhah, P. Zaheri, S.M.A. Mousavian, Separation of molybdenum from spent HDS catalysts using emulsion liquid membrane system, Chemical Engineering and Processing - Process Intensification 153 (2020). https://doi.org/10.1016/j.cep.2020.107958.

[133] K.K. Sahu, A. Agrawal, D. Mishra, Hazardous waste to materials: Recovery of molybdenum and vanadium from acidic leach liquor of spent hydroprocessing catalyst using alamine 308, J Environ Manage 125 (2013) 68–73. https://doi.org/10.1016/j.jenvman.2013.03.032.

[134] H. Wu, S. Duan, D. Liu, X. Guo, A. Yi, H. Li, Recovery of nickel and molybdate from ammoniacal leach liquor of spent hydrodesulfurization catalyst using LIX84 extraction, Sep Purif Technol 269 (2021). https://doi.org/10.1016/j.seppur.2021.118750.

[135] J. Wang, S. Wang, A. Olayiwola, N. Yang, B. Liu, J.J. Weigand, M. Wenzel, H. Du, Recovering valuable metals from spent hydrodesulfurization catalyst via blank roasting and alkaline leaching, J Hazard Mater 416 (2021). https://doi.org/10.1016/j.jhazmat.2021.125849.

[136] N. Nagar, H. Garg, C.S. Gahan, Integrated bio-pyro-hydro-metallurgical approach to recover metal values from petroleum refinery spent catalyst, Biocatal Agric Biotechnol 20 (2019). https://doi.org/10.1016/j.bcab.2019.101252.

[137] A. Alhathal Alanezi, M. Bassyouni, S.M.S. Abdel-Hamid, H.S. Ahmed, M.H. Abdel-Aziz, M.S. Zoromba, Y. Elhenawy, Theoretical investigation of vapor transport

mechanism using tubular membrane distillation module, Membranes (Basel) 11 (2021). https://doi.org/10.3390/membranes11080560.

[138] M.M. Damtie, Y.C. Woo, B. Kim, K.D. Park, R.H. Hailemariam, H.K. Shon, J.S. Choi, Analysis of mass transfer behavior in membrane distillation: Mathematical modeling under various conditions, Chemosphere 236 (2019). https://doi.org/10.1016/j.chemosphere.2019.07.020.

[139] H. Chamani, T. Matsuura, D. Rana, C.Q. Lan, Modeling of pore wetting in vacuum membrane distillation, J Memb Sci 572 (2019) 332–342. https://doi.org/10.1016/j.memsci.2018.11.018.

[140] A.M. Urtiaga, G. Ruiz, I. Ortiz, Kinetic analysis of the vacuum membrane distillation of chloroform from aqueous solutions, 2000. https://doi.org/https://doi.org/10.1016/S0376-7388(99)00220-3.

[141] D.D.L. Wijngaards, E. Cretu, S.H. Kong, R.F. Wolffenbuttel, Modelling of integrated Peltier elements, Mekelweg, 2000.

[142] P.I. Mani, Design, Modeling and Simulation of a Thermoelectric Cooling Design, Modeling and Simulation of a Thermoelectric Cooling System (TEC) System (TEC), 2016. https://scholarworks.wmich.edu/masters_theses.

7 Appendix

7.1 Experimental data points

Table A1: Design of Experiment for varying feed flowrate

Feed Flow rate(L/h)	**Feed Temperature(K)**	**Vacuum Pressure (kPa)**	**Salt concentration (g/L)**	**Flux (LMH)**	**Reject temperature (K)**	**Reject pressure (bar-g)**
150	333.15	7.3	1	4.5	313.348	0.0221
160	333.15	7.3	1	4.82	313.37	0
170	333.15	7.3	1	5.12	313.39	0
180	333.15	7.3	1	5.44	313.42	0
190	333.15	7.3	1	5.72	313.448	0
200	333.15	7.3	1	6	313.46	0

Table A2: Design of Experiment for varying feed temperature

Feed Flowrate(L/h)	Feed Temperature(K)	Vacuum Pressure (kPa)	Salt Concentration (g/L)	Flux (LMH)	Reject Temperature (K)	Reject Pressure (barg)
200	313.15	7.3	1	0.04	313.121	0
200	318.15	7.3	1	1.45	313.234	0
200	323.15	7.3	1	2.95	313.32	0
200	328.15	7.3	1	4.5	313.42	0
200	333.15	7.3	1	6	313.478	0
200	338.15	7.3	1	7.6	313.537	0
200	343.15	7.3	1	9.2	313.59	0

Table A3: Design of Experiment for varying salt concentration

Feed Flowrate(L/h)	Feed Temperature(K)	Vacuum Pressure (kPa)	Salt Concentration (g/L)	Flux (LMH)	Reject Temperature (K)	Reject Pressure (barg)
200	333.15	7.3	5	5.95	313.62	0
200	333.15	7.3	10	5.84	313.77	0
200	333.15	7.3	15	5.734	313.95	0
200	333.15	7.3	20	5.645	314.12	0
200	333.15	7.3	25	5.54	314.3	0
200	333.15	7.3	30	5.44	314.46	0
200	333.15	7.3	35	5.35	314.63	0

Table A4: Design of Experiment for varying vacuum pressure

Feed Flowrate(L/h)	Feed Temperature(K)	Vacuum Pressure (kPa)	Salt Concentration (g/L)	Flux (LMH)	Reject Temperature (K)	Reject Pressure (barg)
200	333.15	7.33	1	6	313.47	0
200	333.15	9.41	1	4.6	318.05	0
200	333.15	11.95	1	3.18	322.68	0
200	333.15	14.73	1	1.88	326.88	0
200	333.15	17.27	1	0.86	330.18	0
200	333.15	18.6	1	0.35	331.81	0

7.2 Mathematical model link

VMD_LAB_Working (7).mo

7.3 Appendix Plots

7.3.1 Studies on Modified Hagen Poiseuille Equation

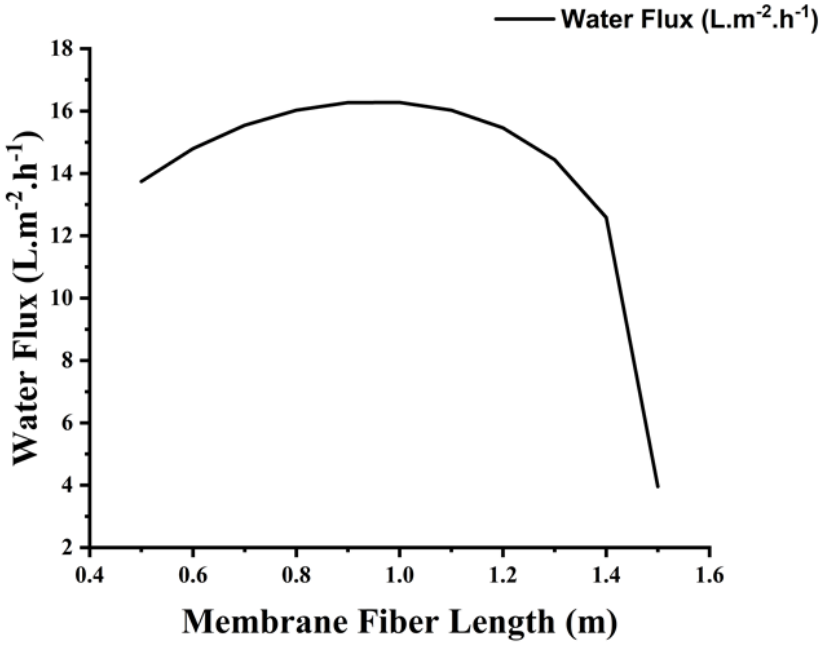

Figure 55: Water flux upon variation of membrane fiber length

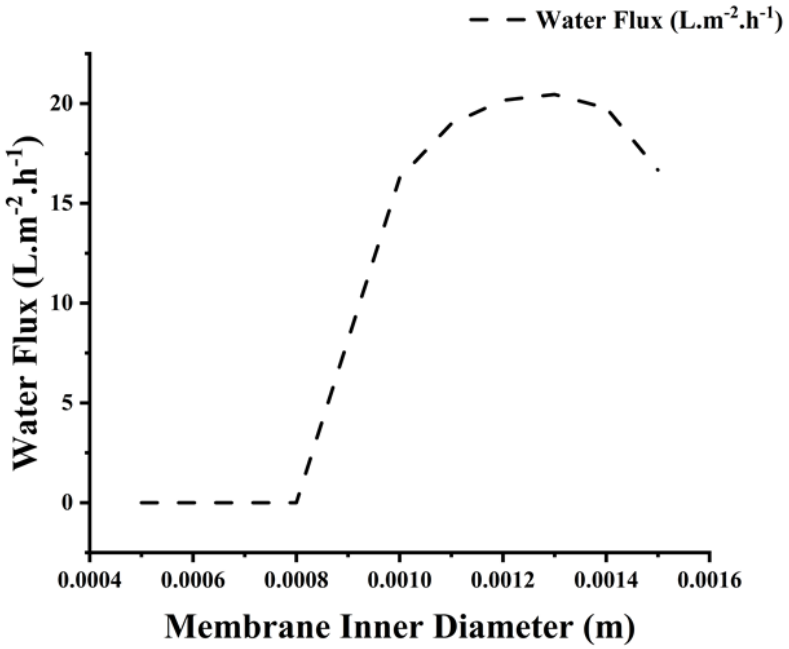

Figure 56:Water flux upon variation of membrane inner diameter

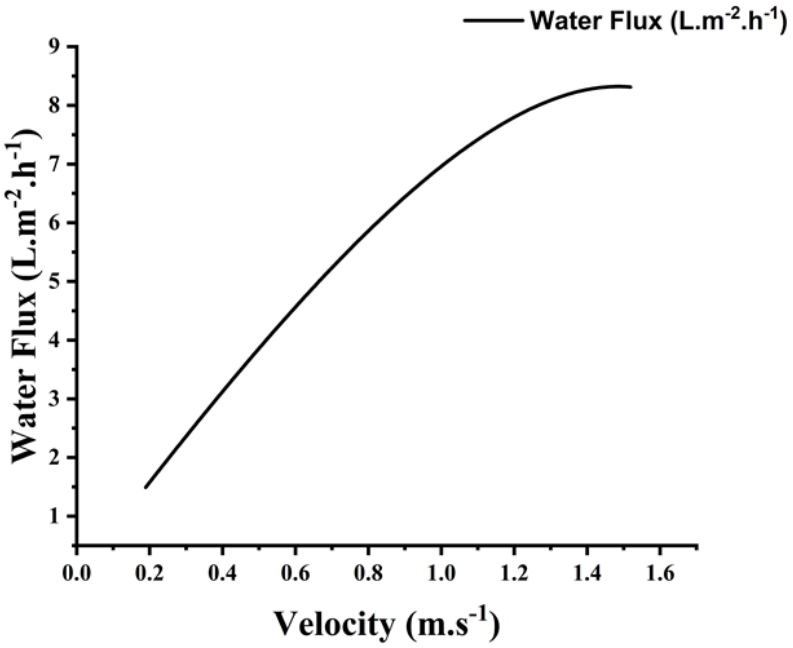

Figure 57:Water flux upon variation of velocity

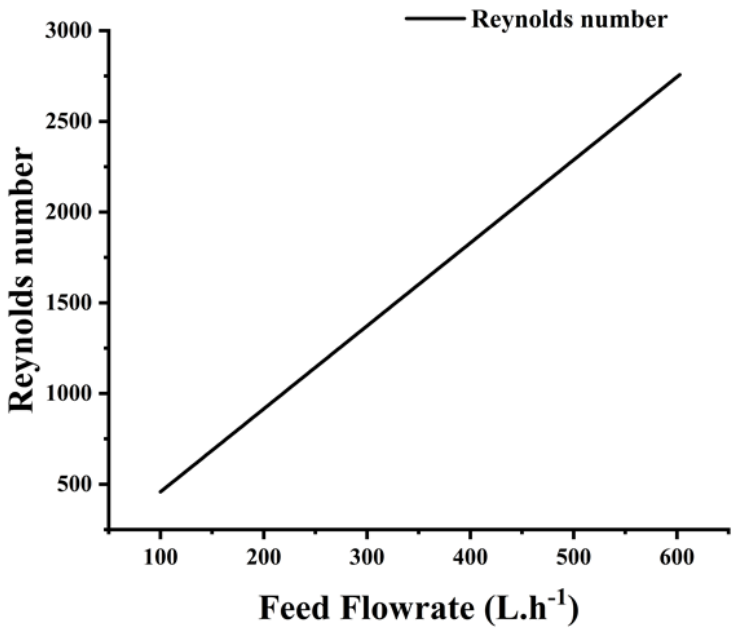

Figure 58: Reynolds number upon variation of feed flowrate

7.4 Study on supersaturation of sodium chloride

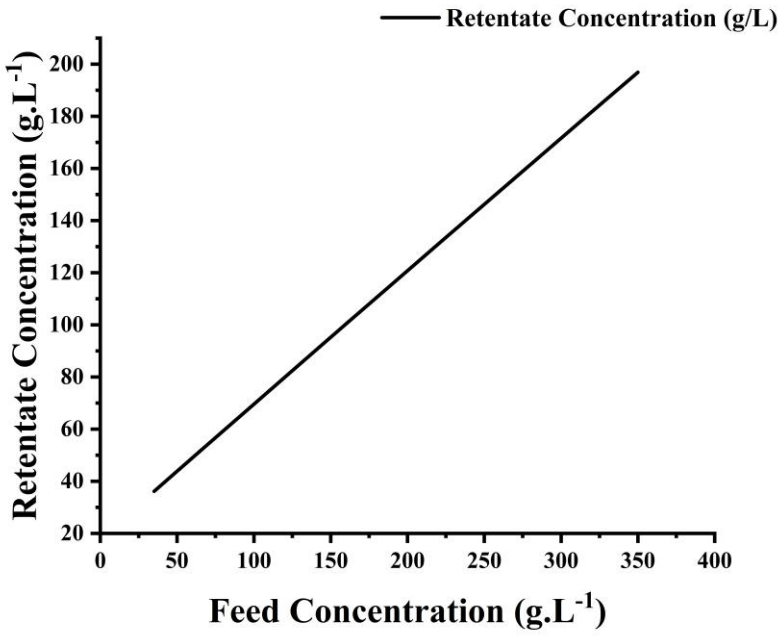

Figure 59: Variation of retentate concentration upon feed concentration

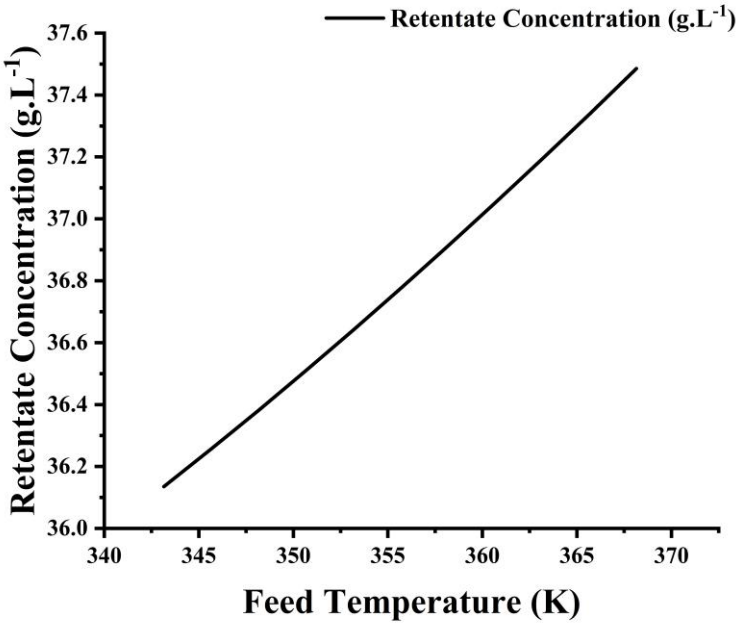

Figure 60: Variation of retentate concentration upon feed temperature